

UiO : **University of Oslo**

Sneha Pandit

A new look at Solar-Stellar Activity with the Atacama Large Millimeter/submillimeter Array

Thesis submitted for the degree of Philosophiae Doctor

Institute of Theoretical Astrophysics
Faculty of Mathematics and Natural Sciences

Rosseland Centre for Solar Physics



2023

© **Sneha Pandit, 2023**

*Series of dissertations submitted to the
Faculty of Mathematics and Natural Sciences, University of Oslo
No. 2691*

ISSN 1501-7710

All rights reserved. No part of this publication may be reproduced or transmitted, in any form or by any means, without permission.

Cover: UiO.
Print production: Graphic center, University of Oslo.

To my aai-baba

Two possibilities exist: either we are alone in the Universe or we are not. Both are equally terrifying.

- Arthur C. Clarke

Abstracts

English Abstract

The Sun, our nearest star, serves as an invaluable reference for the study of solar-like stars, due to the availability of many spatiotemporally resolved solar spectra. Amongst several spectral lines, some of the strongest chromospheric diagnostics are the Ca II H & K lines which can be used to gauge the temperature stratification of the atmosphere as the line core and wings are formed at different heights of the solar atmosphere. Furthermore, the H α line is a tracer for the magnetic structures and its line core provides an estimation of the mass density.

Complementing these diagnostics are brightness temperatures derived from observations made by the Atacama Large Millimeter (mm)/ submillimeter (sub-mm) Array (ALMA). These data open up fresh perspectives on stellar atmospheric activity and thermal structures. First, we compare synthetic Ca II and H α spectra with their corresponding millimetre continuum maps to gain deeper insights into the stellar structure.

To obtain synthetic spectra for the Ca II lines, H α line, and mm-sub mm continuum, this work employs radiative transfer codes such as RH1.5D, ART, and Multi3D. These simulations are based on an enhanced network atmosphere model created using the state-of-the-art Bifrost code. The resulting activity indices are then used to compare solar-like stars with the solar spectrum. These indices reveal crucial details about temperature stratification, magnetic structures, and mass density distribution in stellar atmospheres. Notably, we find strong correlations between the H α linewidth and ALMA Band 7 data, the Ca II s index and the lower chromosphere, and the Ca II Infrared triplet (IRT) index and an even lower atmospheric layer near the upper photosphere.

Furthermore, we undertake long-term full-disk (FD) total power (TP) observations from ALMA and compare them with other diagnostic data sources, including UV-EUV data from Solar Dynamics Observatory Atmospheric Imaging Assembly (SDO/AIA) and microwave data from the Radio Polarimeter from the Nobeyama observatory, as well as s index data. The first long-term solar activity variation using ALMA TP data is observed in this work. There exists notable short-term variations as well. As a result, a systematic utilisation of a combination of the SDO/AIA 304, 1600, and 1700, channels, which originate from comparable altitudes and display strong correlations with ALMA data, might be worth considering for enhancing the TP calibration process.

In summary, this PhD project revolves around a comparative exploration of solar and stellar activity among Sun-like stars. The investigations are based on observations from ALMA, in conjunction with other solar and stellar observational and synthetic data.

Norsk Sammendrag

Solen, vår nærmeste stjerne, fungerer som en uvurderlig referanse for studiet av sollignende stjerner, på grunn av tilgjengeligheten av mange romlig og tidsmessig oppløste solspektre. Blant flere spektrallinjer er Ca II H & K-linjene noen av de sterkeste linjene for kromosfæriske diagnoser da de kan brukes til å måle temperaturfordelingen i solens atmosfære, ettersom linjekjernen og -vingene dannes i forskjellige høyder av solens atmosfære. Videre er H α -linjen en sporer for de magnetiske strukturene, og linjekjernen gir en estimering av massetettheten.

I tillegg til denne diagnostikken er lysstyrketemperaturer hentet fra observasjoner gjort av Atacama Large Millimeter (mm)/ submillimeter (sub-mm) Array (ALMA). Disse dataene åpner for nye perspektiver på stjerners atmosfæriske aktivitet og termiske strukturer. Først sammenligner vi syntetiske Ca II- og H α -spektre med deres tilsvarende millimeterkontinuumskart for å få dypere innsikt i stjernestrukturen.

For å oppnå syntetiske spektre for Ca II-linjene, H α -linjen og mm-sub mm kontinuum, bruker dette arbeidet strålingstransportkoder som RH1.5D, ART og Multi3D. Disse simuleringene er basert på en forbedret nettverksatmosfæremodell laget ved hjelp av den toppmoderne Bifrost-koden. De resulterende aktivitetsindeksene brukes deretter til å sammenligne sollignende stjerner med solspekteret. Disse indeksene avslører viktige detaljer om temperaturfordeling, magnetiske strukturer og massetetthetsfordeling i stjerneatmosfærer. Spesielt finner vi sterke korrelasjoner mellom H α linjebredde og ALMA Band 7 data, Ca II s indeksen og den nedre kromosfæren, og Ca II infrarød triplett (IRT) indeks og et enda lavere atmosfærisk lag nær den øvre fotosfæren.

Videre foretar vi langsiktige full-disk (FD) total power (TP) observasjoner fra ALMA og sammenligner dem med andre diagnostiske datakilder, inkludert UV-EUV data fra Solar Dynamics Observatory Atmospheric Imaging Assembly (SDO/AIA) og mikrobølgedata fra Radio Polarimeter fra Nobeyama-observatoriet, samt s-indeksdata. Den første langsiktige solaktivitetsvariasjonen ved bruk av ALMA TP-data er observert i dette arbeidet. Det finnes også bemerkelsesverdige kortsiktige variasjoner. Som et resultat kan en systematisk bruk av en kombinasjon av SDO/AIA 304, 1600 og 1700, som stammer fra sammenlignbare høyder og viser sterke korrelasjoner med ALMA-data, være verdt å vurdere for å forbedre TP-kalibreringsprosessen.

Oppsummert dreier dette doktorgradsprosjektet seg om en komparativ utforskning av sol- og stjerneaktivitet blant sollignende stjerner. Undersøkelsene er basert på observasjoner fra ALMA, sammen med andre sol- og stjerneobservasjonsdata og syntetiske data.

Preface

This thesis is submitted in partial fulfilment of the requirements for the degree of *Philosophiae Doctor* at the University of Oslo. The research presented here was conducted at the Rosseland Centre for Solar Physics (RoCS), within the Institute of Theoretical Astrophysics (ITA) at the University of Oslo (UiO), and under the supervision of Professor Sven Wedemeyer. The research of this thesis was supported by the EMISSA project, which received funding from the FRINATEK grant by the Research Council of Norway (grant agreement No. 286853). Also through its Centres of Excellence scheme, project number 262622 and through grants of computing time from the Programme for Supercomputing. Computational resources have been provided by Sigma2 – the National Infrastructure for High-Performance Computing and Data Storage in Norway.

Acknowledgements

When I came to Norway 4 years ago, I was young and naïve, excited about the world and the idea of becoming a scientist! I came here with enthusiasm and determination to learn more about the sun and stars and expand the horizon of existing knowledge in some ways. I did not know I would get to explore so much of not only science and the scientific field but also different cultures, customs, languages and whatnot! I am immensely grateful to Rosseland Centre for Solar Physics and Institute for Theoretical Astrophysics at the University of Oslo for this opportunity. Life here has been quite challenging and enriching, from living by myself in a strange land, away from everyone that I knew before, living in darkness and snowy winters, and in bright summers, to travelling and taking up adult hobbies like cooking and gardening. It benefited me in more ways than I could have ever imagined. While the worldwide pandemic certainly dampened the spirits of everyone, the people around me made this transition from a simple curious girl to a <functioning adult with broadened horizons, who might just make it through academia>, seem effortless.

Firstly, I would like to express my sincere gratitude to my supervisor, Sven Wedemeyer. My sincere thanks to you, Sven, for your encouragement, valuable advice, stimulating discussions, guiding me in the right direction, and showing that you believe in me. I have learnt a lot from you, and I believe that this is just the beginning of a wonderful collaboration.

Thank you Mats Carlsson for being a constant pillar of strength sitting in the next office. The poise that you carry yourself with is very motivating and your excitement for new science is very inspiring. I am very lucky to have you as a collaborator.

I would like to express my heartfelt appreciation to Atul Mohan. Thanks, Atul for being there whenever I wanted to discuss ideas, for providing invaluable inputs and for pushing me to strive for better. Thanks for the in-depth discussions not only about interferometry, TP maps and stellar activity but also about politics, cultures, foods and I believe everything under the sun! And thanks Anuvinda for making me miss my family a little less with your warmth.

Luc Rouppe van der Voort, thank you for the conversations about sports, movies, food and the sun of course. Thank you, Tiago Pereira, for the help in the technical aspects of the thesis and for being a source of inspiration. Mikolaj Szyldarski, thank you for being a generous provider of coding solutions and inspiring me to be more brave and close to nature as a city girl. Thank you, Shahin Jafarzadeh, for the introduction to the Norwegian bureaucracy. Thank you Sonal and Jayant Joshi for providing a place with so much understanding and warmth. Thank you Maryam Saberi for the walks and our tea-time conversations. Thanks are also due to the PIs and current and former scientists at the Rosseland Centre of Solar Physics and the Institute of Theoretical Astrophysics. Specifically,

Acknowledgements

I would like to mention Boris Gudiksen, Viggo Hansteen, Guadalupe Barrios, Reetika Joshi, Ana Belén Grinon Marin, Carlos Quintero Noda, Avijeet Prasad, Killian Krikova, Ignasi Pouquet, Michael Haahr, George Cherry, Aditi Bhatnagar, Sondre Furuset, Quentin Noraz, Elias Roland Udnæs, Jonas Thoen Faber for making time at RoCS very pleasant and memorable. I want to thank my colleagues and friends Souvik, Henrik and Juan for helping me get assimilated into the culture of academia and Norway. A special thanks to Becca Robinson, Helle Bakke, Øystein Færder, Fredrick Clemmensen and Nicolas Poirier for the Room 216 lunches, day trips, occasional to regular break conversations and hugs. Hearty thanks to Thore Espedal Moe, Mats Ola Sand, Eilif Sommer Øyre, Vasco Henriques, and Carlos José Díaz Baso for discussions about specific and broad topics in the thesis and for making the work environment much more enjoyable.

My sincere thanks go out to all the IT and administration staff at the institute. Thank you, Benedikte Fagerli Karlsen, Sara Nettum, Heidi Haugsand, Kristine All Knudsen, Brenda Apili Atubo, Morsal Saba, Ida Emilie Moe, and Eyrun Thune for shielding me from the bureaucratic work and making the experience here more colourful. Special thanks to Kjell Andresen and Torben Leifsen for the quick technical solutions with my laptop and workstation.

I would like to express my appreciation for the memorable experiences I had with Chinmayi and Shreeshti, who made my stay in Norway easier, more enjoyable and were always there for me when I needed them. I want to mention my dance Guru Deepa tai and Revati tai, for showing me a graceful way out of the COVID times through the online dance sessions and encouraging me in the completion of my Bharatanatyam diploma. For the occasional family time that I needed during the festive seasons, I would like to thank Poonam-Vishal, Aarav and Aryan. I would also like to mention the support that our Vestli Cricket Klubb showed, especially Paridhi, Pooja, Bijeyta, Solly, Ramya, and Gopi-coach.

A special mention to Gayatri, Sagnik, Gaurav, Shamim, Pratyasha, and Swapnali, for being the friends that I can count on even from large distances. It is not possible to name everyone with whom I crossed paths on this journey, so I would also like to thank the unnamed inspirations that I got through travelling and hiking.

My family has been the bedrock of my existence. It is because of you, Aai-Baba ani Aji-Ajoba, that I believe in myself and am able to achieve my goals. Throughout my life, you have believed in me, encouraged me, and stayed true to yourself. Thank you so much! Aai ani baba, you are my inspiration and I wouldn't be where I am without you. I would also like to thank my new family, aai-baba, dada-vahini ani choti Chiku, for bringing much joy and support.

Lastly, to my person: Aniket, who has been here throughout this turmoil, for better or for worse, thanks for being a patient and curious listener, my personal critic and my source of encouragement. It has not been an easy journey for either of us, staying thousands of kilometres away from each other for months, and years. I'm looking forward to the amazing times ahead of us!

• **Sneha Pandit**

Oslo, November 2023

List of Publications

Paper I

Comparison of chromospheric diagnostics in a 3D model atmosphere:
H α linewidth and mm continua

S. Pandit, S. Wedemeyer, M. Carlsson, M. Szydlarski.

Published in: *Astronomy and Astrophysics*, Vol. 673, no. A137 (2023)

DOI: [10.1051/0004-6361/202245412](https://doi.org/10.1051/0004-6361/202245412)

arXiv link: <https://arxiv.org/abs/2303.15612>

Paper II

EMISSA (Exploring Millimeter Indicators of Solar-Stellar Activity).
III. Comparison of Ca II indices and millimetre continua in a 3D
model atmosphere

S. Pandit, S. Wedemeyer, M. Carlsson.

Under review

Paper III

EMISSA (Exploring Millimeter Indicators of Solar-Stellar Activity).
IV. Full-disk observations of the Sun

S. Pandit, S. Wedemeyer, A. Mohan, Sowmya K., H. Eklund.

Soon to be submitted for publication.

List of Publications Not Included in this Thesis

- **EMISSA (Exploring Millimeter Indicators of Solar-Stellar Activity): I. The initial millimeter centimeter main-sequence star sample**
Atul Mohan, Sven Wedemeyer, **Sneha Pandit**, Peter H. Hauschildt, Maryam Saberi
Published in: *Astronomy and Astrophysics*, Vol. 655, no. A113 (2021)
DOI: [10.1051/0004-6361/202142095](https://doi.org/10.1051/0004-6361/202142095)
arXiv link: <https://arxiv.org/abs/2110.13339>
- **EMISSA (Exploring Millimeter Indicators of Solar-Stellar Activity): II. Towards a robust indicator of stellar activity**
Atul Mohan, Sven Wedemeyer, Peter H. Hauschildt, **Sneha Pandit**, Maryam Saberi
Published in: *Astronomy and Astrophysics*, Vol. 664, no. L9 (2022)
DOI: [10.1051/0004-6361/202244385](https://doi.org/10.1051/0004-6361/202244385)
arXiv link: <https://arxiv.org/abs/2208.04217>

Contents

Abstracts	iii
English Abstract	iii
Norsk Sammendrag	iv
Preface	v
Acknowledgements	vii
List of Publications	ix
List of Publications Not Included in this Thesis	xi
Contents	xiii
List of Figures	xv
List of Tables	xxi
1 Introduction	1
1.1 Stellar Structure	3
1.2 Photosphere	5
1.3 Chromosphere	7
1.4 Transition Region and Corona	11
1.5 Solar Wind and Space Weather	13
2 Formation Mechanisms for Radiation	15
2.1 Continuum Radiation	16
2.2 Formation Heights of the mm radiation	18
3 Instruments and Simulations	21
3.1 Optical Observations	22
3.2 Interferometric Observations	23
3.3 Synthetic Observations	32
4 Stellar Activity	39
4.1 Activity indicators	40
5 Contextual Description and Summary of Papers	49
5.1 Comparison of chromospheric diagnostics in a 3D model atmosphere: H α linewidth and mm continua	49
	xiii

Contents

5.2	EMISSA (Exploring Millimeter Indicators of Solar-Stellar Activity). III. Ca II indices and mm continua	50
5.3	EMISSA (Exploring Millimeter Indicators of Solar-Stellar Activity). IV. Full-disk observations of the Sun	51
5.4	Concluding Remarks and Future Prospects	51
Papers		54
I	Comparison of chromospheric diagnostics in a 3D model atmosphere: Hα linewidth and mm continua	55
II	EMISSA (Exploring Millimeter Indicators of Solar-Stellar Activity). III. Comparison of Ca II indices and millimetre continua in a 3D model atmosphere	77
III	EMISSA (Exploring Millimeter Indicators of Solar-Stellar Activity). IV. Full-disk observations of the Sun	95
Bibliography		117

List of Figures

1.1	In the Hertzsprung-Russell diagram the temperatures of stars are plotted against their luminosities. The position of a star in the diagram provides information about its present stage and its mass. Image Credit: ESO	2
1.2	The naming system of stars based on the stellar classification in spectral class, subclass and luminosity class is depicted in a flow chart. Image Credit: Sven Wedemeyer	2
1.3	The image shows the structure of the Sun including the interior with core, radiative zone and convective zone, as well as the atmospheric layers, namely the photosphere, chromosphere and corona. The image also shows some active phenomena like sunspots, flares, prominence and coronal hole. Image Credit: NASA	3
1.4	The average temperature (solid line) and density (dashed line), in accordance to the 1D semi-empirical VAL model (Vernazza, Avrett, and Loeser, 1981), of the different layers in the solar atmosphere, as a function of height.	4
1.5	Stellar interiors vary based on their mass and spectral type. Low-mass stars, less than half a solar mass, are fully convective from core to surface due to high opacity at low temperatures. Intermediate-mass stars, like the Sun, have a convective region above a stagnant core. Their surfaces retain the same composition as the cloud from which they formed. At 1.5 solar masses, the convective layer almost disappears, and the star becomes fully radiative. Beyond 1.5 solar masses, the CNO cycle dominates energy production, leading to a convective core due to the concentration of energy in the centre. Image source: commons.wikimedia	5
1.6	A high-resolution wide-band image of the quiet sun photosphere with distinct granulation pattern as observed with the Swedish 1-m Solar Telescope at La Palma, Spain. The area is 49 Mm × 31 Mm, with a resolution of about 28 km/pixel. The area was located close to the disk centre. Courtesy of Luc Rouppe van der Voort.	7

List of Figures

1.7	The full-disc solar image was taken with the Helioseismic and Magnetic Imager (HMI) on board the Solar Dynamics Observatory (SDO). The image of the full solar disk was taken in the continuum in the red visible part of the spectrum. A cooler, darker sunspot is visible in the disc, and a visual comparison is shown alongside the image from ALMA Band 6 at a wavelength of 1.25 millimetres. Image Credit: ALMA (ESO/NAOJ/NRAO), NASA.	8
1.8	High-resolution Ca II H core image observed at the same observation with the same technical configuration as in Figure 1.6. It shows a quiet sun chromosphere with magnetic network regions with (short) chromospheric fibrils and internetwork regions with weaker magnetic fields. Courtesy of Luc Rouppe van der Voort.	9
1.9	The global picture of the structure of solar atmosphere: the different layers in the solar atmosphere, different physical phenomena as a function of height. Image Credit: Wedemeyer-Böhm, Lagg, and Nordlund, 2009	10
1.10	The composite image of the solar corona, created using three different passbands, is displayed as an RGB composition. The red colour represents the 211 Å passband, which is formed at temperatures around 2 million Kelvin. The green colour represents the 193 Å passband, corresponding to temperatures of approximately 1.3 million Kelvin. Lastly, the blue colour represents the 171 Å passband, formed at around 800,000 Kelvin. This image was captured using NASA's SDO/AIA instrument. Image Credit: Heliophysics Events Knowledgebase, Lockheed Martin Solar and Astrophysics Lab, Palo Alto.	12
1.11	The illustration shows the interaction between the magnetic fields of the Sun and the earth along with the possibility of flares and solar wind directed towards the earth. The particles will eventually be directed to the auroral ovals. Image Credit: Chukwuma Anoruo, University of Nigeria, Nsukka obtained from the PAGES Early-Career Network (ECN) blog	14
2.1	The temperature distribution in the solar atmosphere can be described based on the widely recognised VAL semi-empirical model. The photosphere extends up to approximately 500 km in height. Beyond 500 km and up to around 2000 km, the temperature increases, marking the presence of the chromosphere. The transition region, located beyond 2000 km, exhibits a rapid temperature rise, serving as the boundary between the chromosphere and the extremely hot corona, which reaches temperatures in the millions of degrees. Various atomic species are responsible for the observed spectral lines, marked on the plot, each indicating a specific ionisation state and average formation heights. Image credit: Vernazza, Avrett, and Loeser, 1981	16

2.2	The average contribution functions of the continuum mm intensity, at the different heights in the solar atmosphere, as a function of height. Credit: Wedemeyer et al., 2016.	18
3.1	This high-resolution spectrum of the Sun was obtained from a digital atlas observed with the Fourier Transform Spectrometer (FTS) at the McMath-Pierce Solar Facility at the National Solar Observatory on Kitt Peak, Arizona. The image resembles an echelle spectrum, with wavelength increasing from left to right and from bottom to top. Each of the 50 slices covers 6 nm, providing a complete spectrum across the optical range from 400 to 700 nm. Image Credit: N.A.Sharp, NOAO/NSO/Kitt Peak FTS/AURA/NSF	22
3.2	This snapshot captures a segment of the ALMA facility. In the centre, you can observe the closely grouped Atacama Compact Array, consisting of twelve 7-meter antennas. They are encircled by four total power antennas and several additional antennas belonging to the main array, which stretches over several kilometres beyond what is visible in the photograph. Image Credit: ALMA (ESO/NAOJ/NRAO)	25
3.3	The observations taken on 23rd April 2017 with ALMA Bands 3 and 6. Credit for the dataset: ALMA ADS/JAO.ALMA2016.1.01532.S	28
3.4	The co-observations taken on 23rd April 2017 from IRIS slit jaw imager, IBIS and SDO AIA channels 1600, 1700 and 304, and HMI magnetogram are compared with the co-aligned observations from ALMA Band 3. Credit for the co-aligned dataset: Kevin Reardon, Johnathan Strauffer	29
3.5	Same as Figure 3.4, for ALMA Band 6. Credit for the co-aligned dataset: Kevin Reardon, Johnathan Strauffer	30
3.6	The figure displays a double-circle pattern representing a 2400'' diameter field of view with a "map spacing" of 30''. Inside this, a dashed-line circle at a radius of 600'' represents the "major circle" track of the individual minor circles' centres. Additionally, a dotted line marks the (average) solar limb at a radius of 960''. The telescope track is colour-coded with a rainbow colour table, indicating the pointing location's progress over time. Mapping commenced and concluded approximately at the "3 o'clock" location in the figure. Taken from White et al., 2017	31

3.7	Full disk (FD) non-rescaled images of the Sun in different wavelengths from the less active period in 2019, the top row shows FD maps from ALMA bands 3 (from April), 6 (from November) and 7 (from December), and the rest of FD maps are from the different channels of AIA onboard SDO (co-temporal to Band 6 data). Different wavelengths probe different layers, 304 Ångstroms being the closest to ALMA maps. The limb effects: brightening in ALMA FD maps, and limb darkening in SDO AIA channels 1600, and 1700 is clearly visible.	33
3.8	The deep-red visible spectral line of the hydrogen atom has a wavelength of 656.28 nm in air and 656.46 nm in a vacuum. This line belongs to the Balmer series and represents the first spectral line emitted when an electron transitions from the third- to the second-lowest energy level of a hydrogen atom. Image Credit: commons.wikimedia	35
3.9	For all transitions, the line centre or threshold wavelengths are given in Ångströms. The atomic levels are shown with the valence electron configuration nl on the left, the total angular momentum J on the top, and the term configuration $2S+1L^P$ at the bottom row. Solid line for bound-bound transition, dashed line for forbidden transition, orange line for PRD transitions and dotted line for bound-free transitions connecting levels to the Ca II continuum. Taken from (Bjørgeren et al., 2018).	36
3.10	Typical features of Ca II K (b) and H (c) quiet sun lines for observed Fourier Transform Spectrometer (FTS) spectra (black) and the spectra synthesised with the RH code (red). The y-axis is the intensity in SI units and the x-axis is the wavelength in Ångströms. The dashed black lines represent the triangular filters for the s index described further in Chapter 4. Taken from Sowmya et al., 2021.	36
4.1	The variation in the number of sunspots over 400 years. The number of sunspots on the solar disk varies over a period of approximately 11 years. Image source: commons.wikimedia . . .	40
4.2	Full disk (FD) non-rescaled images of the Sun in different wavelengths from the more active period in December 2015, the top row shows FD maps from ALMA bands 3 (from 16th), 6 (from 18th) from the science verification data, and the rest of FD maps are from the different channels of AIA onboard SDO (co-temporal to Band 6 data). Different wavelengths probe different layers, 304 Ångstroms being the closest to ALMA maps, similar to Figure 3.7. Band 6 data shows sunspots aligned to 1600 and 1700 channels and plage regions as seen in 304 channel. Channels 131 and 335 are omitted due to bad datasets, Band 7 data was not commissioned in 2015.	41

4.3	Full disk (FD) non-rescaled images of the Sun in different wavelengths from another more active period in 2022, the top row shows FD maps from ALMA bands 3 (from October), 6 and 7 (from April), and the rest of FD maps are from the different channels of AIA onboard SDO (co-temporal to Band 6 data). Plage regions and bright features are seen clearly. The band 7 data had some extreme temperatures owing to severe antenna response.	42
4.4	Sunspot Area Butterfly Diagram. This shows the distribution of sunspot area as a function of latitude since 1874. As of 2023, we are in cycle 25. Image Credit: SolarCycleScience.com	43
4.5	Scatter plot for the values of the numerator and denominator of the s index as described in Equation (4.1) for the Bifrost model as described in Chapter 3. The contours and the histograms on the right and top show the density distribution for the numerator and the denominator respectively. Datapoints for FAL models (Fontenla, Avrett, and Loeser, 1993) are plotted for comparison with a reference.	47
4.6	Contour plot same as in Figure 4.5 shown in pink filled contours, the green and black contours on the left and right show the difference in density distribution in more active enhanced network patch and a quieter patch shown in respective insets.	48

List of Tables

2.1	Average formation heights (in Mm) of the mm continuum formed in chromosphere as calculated by Martinez-Sykora et al., 2020 based on 2D atmospheric models with different methods for treating the ionisation balance: (i) in LTE and (ii) non-equilibrium for hydrogen and helium compared with the results from Wedemeyer-Böhm et al., 2007 and Loukitcheva et al., 2015	19
3.1	The wavelength and frequency coverage of ALMA bands 1 - 10. Bands 3, 5, 6 and 7 (shown in Bold) are offered for solar observations. Band 3 and 6 have been in operation for solar observations since 2015, and Band 7 and 5 are offered more recently in 2019 and 2023 respectively. Credit: ALMA (ESO/NAOJ/NRAO)	26

Chapter 1

Introduction

"We are just an advanced breed of monkeys on a minor planet of a very average star. But we can understand the Universe. That makes us something very special." Stephen Hawking told the German paper *Der Spiegel* in 1988. Scientists believe that the universe is currently made of less than 5% matter¹ distributed among galaxies, stars, clusters, and gas clouds. Within galaxies or gas clouds, gravity causes matter to interact and accrete. As gas and dust within interstellar clouds collapse due to gravitational forces, they release thermal energy, forming protostars. When nuclear reactions, such as hydrogen to helium conversion, become the primary energy source, a star is born, appearing on the Hertzsprung-Russell (HR) diagram shown in [Figure 1.1](#)

The HR diagram is a graphical representation of stars that illustrates the correlation between their absolute magnitudes or luminosities and their stellar classifications or effective temperatures. Formulated independently by Hertzsprung, 1911 and Russell, 1914, this diagram marked a significant milestone in comprehending stellar evolution.

The stars that fuse hydrogen into helium in their cores, and lie on the main branch of the HR diagram, are called main sequence stars. These stars can be represented on the HR diagram as the main continuous branch. Depending on the surface temperatures, these are classified into O, B, A, F, G, K and M spectral classes, O being the hottest (nearly 30,000 K) and M being the coolest (about 3,000 K). Within the stellar spectral classes, the stars are classified into decimal sub-divisions based on the temperature of the surface. Further based on the luminosity the stars are divided into different luminosity classes (I - VI) as explained in [Fig. 1.2](#). The Sun is a **G2V** type star.

The Sun is not a first-generation star, as it contains heavier elements (Asplund, Amarsi, and Grevesse, 2021), like iron, which we observe to understand the structure of the solar atmosphere, like in [Figure 1.10](#), which can not be produced by the nuclear fusion reactions. These heavier elements must have already existed within the nebula in which our Sun formed. All the planets and subsequently life on the Earth are made from stardust from previous stars and nebula(e) and sustained entirely by our host star, the Sun. The light, energy and energetic particles reaching the Earth, have their origin deep within the solar interior, where the Sun's global magnetic field is generated through the differential rotation of plasma. The interaction of this magnetic field with convective drivers results in complex processes that convert its energy into thermal and kinetic energy.

¹<https://chandra.harvard.edu/darkuniverse/>

1. Introduction

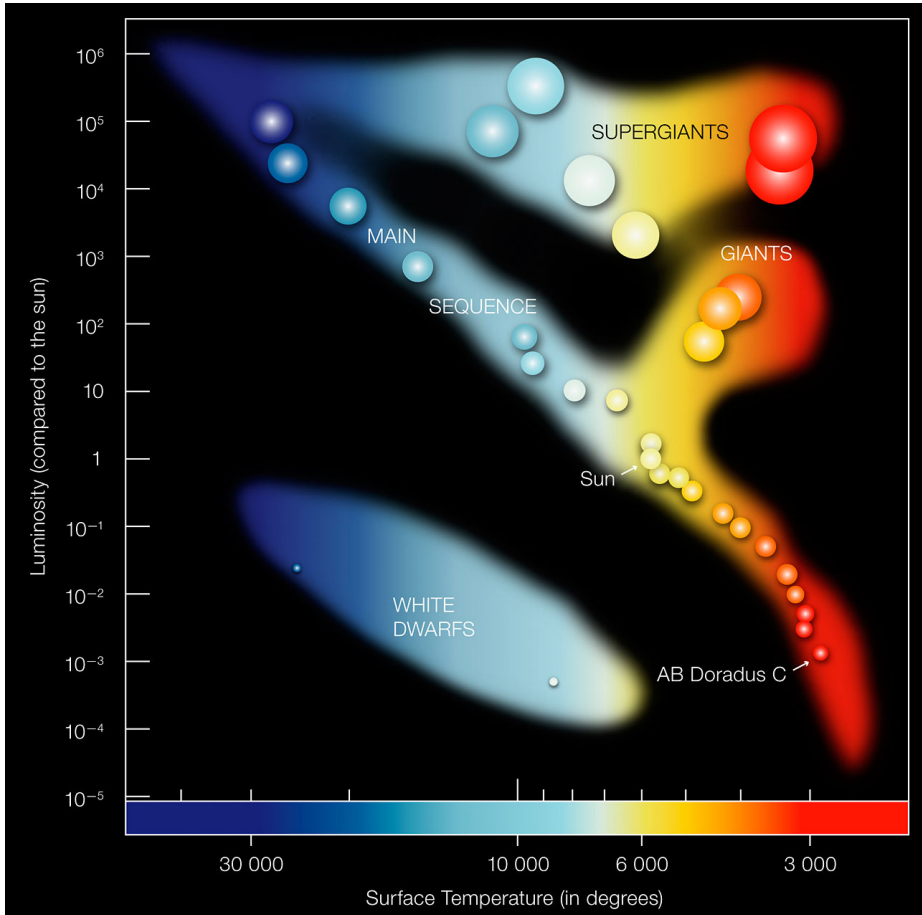


Figure 1.1: In the Hertzsprung-Russell diagram the temperatures of stars are plotted against their luminosities. The position of a star in the diagram provides information about its present stage and its mass. Image Credit: ESO

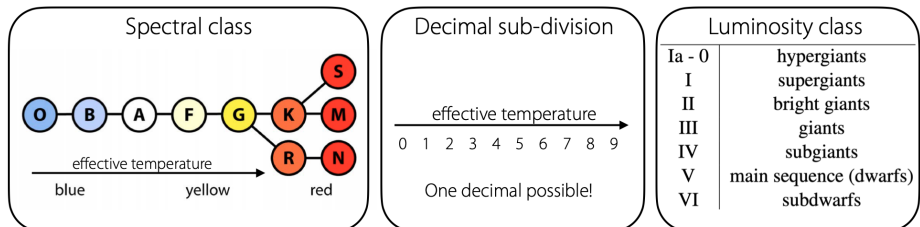


Figure 1.2: The naming system of stars based on the stellar classification in spectral class, subclass and luminosity class is depicted in a flow chart. Image Credit: Sven Wedemeyer

1.1 Stellar Structure

The main sequence stars can be divided into two parts, the interior, below the visible surface called the photosphere, and the atmosphere which is extensively observed with several telescopes and observatories. The structure of the Sun is shown in Figure 1.3. The interior consists of the core, where the energy is produced and then the surrounding volume, where the energy is transported, and these layers are named according to the transport mechanism of the energy. This is elaborated further in this section. The outer atmospheric layers called the photosphere, chromosphere and corona, are further described in this chapter.

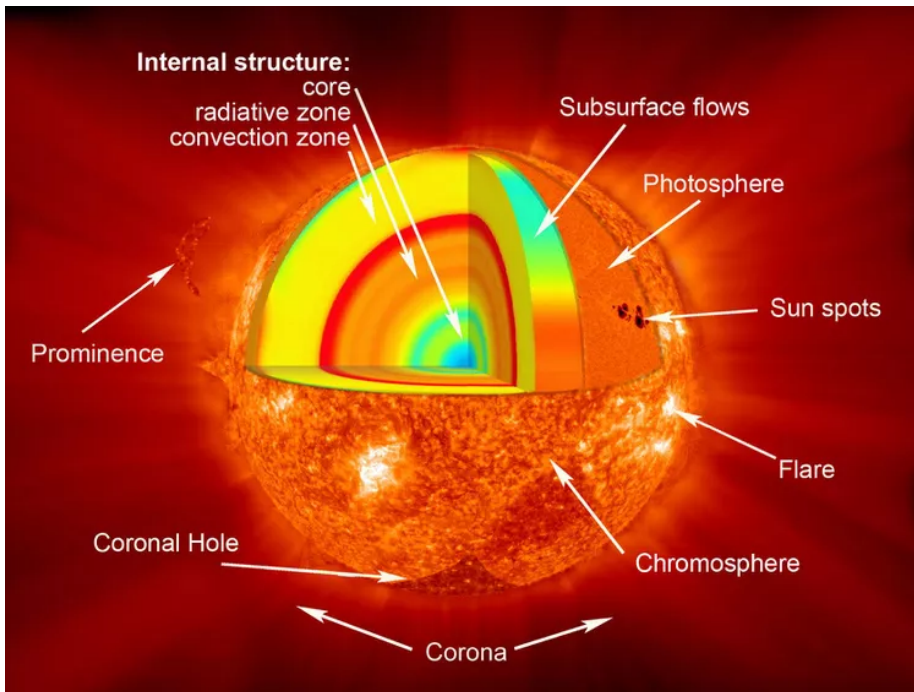


Figure 1.3: The image shows the structure of the Sun including the interior with core, radiative zone and convective zone, as well as the atmospheric layers, namely the photosphere, chromosphere and corona. The image also shows some active phenomena like sunspots, flares, prominence and coronal hole. Image Credit: NASA

Figure 1.4 depicts the average temperature and density of different layers in the solar atmosphere based on the one-dimensional semi-empirical VAL model (Vernazza, Avrett, and Loeser, 1981). The photosphere is defined to be near a height of $1 R_{\odot}$ (indicated as height zero in Fig. 1.4) and serves as the lower boundary of the solar atmosphere. More precisely, the photosphere's height is commonly defined as the point where the gas becomes transparent for radiation for a large range in wavelength which impacts the energy transport and thus

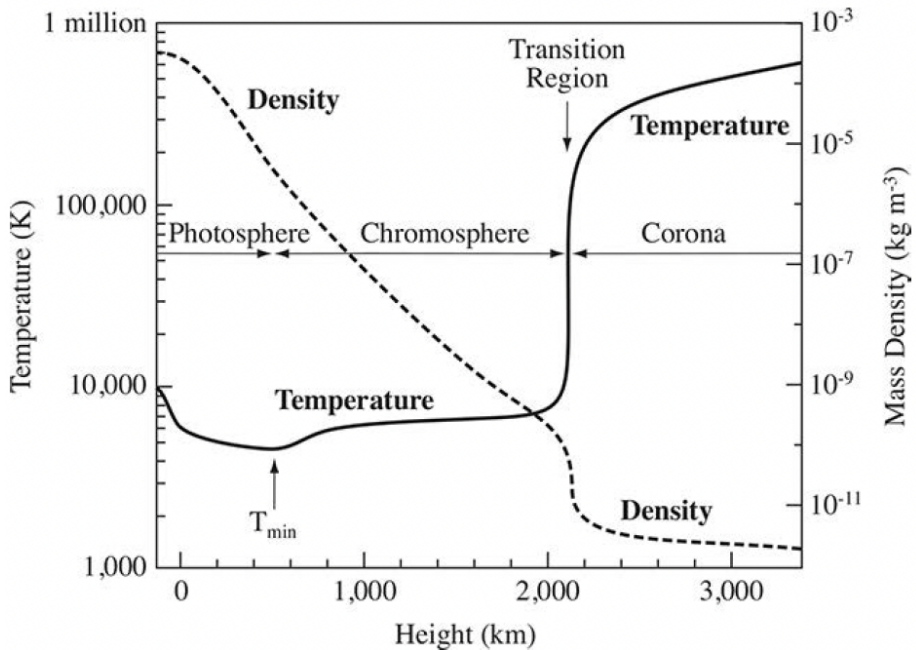


Figure 1.4: The average temperature (solid line) and density (dashed line), in accordance to the 1D semi-empirical VAL model (Vernazza, Avrett, and Loeser, 1981), of the different layers in the solar atmosphere, as a function of height.

creates a boundary between the convection zone and the atmosphere, i.e., the region where the radiation at a wavelength of 500 nm reaches an optical depth of one, that suggests that approximately half² of the photons will escape (Hubeny and Mihalas, 2014). With an average upper limit of 500 km, the photosphere has a thickness of a few hundred kilometres. The temperature within the photosphere averages around 6 kK and decreases with increasing height until reaching approximately 4 kK at the temperature minimum (T_{\min}) in VAL-type models (Avrett, 2003). Acting as an interface between the solar interior and the outer atmosphere, the photosphere is the densest layer of the solar atmosphere.

A main sequence star undergoes nuclear fusion in its core, hydrogen is converted to helium and this releases an immense amount of energy. Plasma motions and energy transport within the stellar interiors are shown in Figure 1.5³. The outer atmospheric layers of the stars are of different extents based on the interiors, mass, surface temperatures, metallicity and spectral types. In a G2V star like our Sun, high pressure and temperature ($T \approx 15$ MK) enable nuclear fusion in the core, converting hydrogen to helium. This energy is transferred to

²An approximation of $1/e$. 37% to be exact.

³The mentioned CNO cycle, i.e. the carbon-nitrogen-oxygen cycle, is a process of stellar nucleosynthesis in which Main Sequence stars produce energy by fusion reactions converting hydrogen into helium

the radiative zone, extending to about 0.7 solar radii ($R_{\odot} \approx 7 \times 10^5$ km). High opacity limits photon travel, taking roughly 170,000 years for photons to move from $0.25R_{\odot}$ to $0.7 R_{\odot}$.

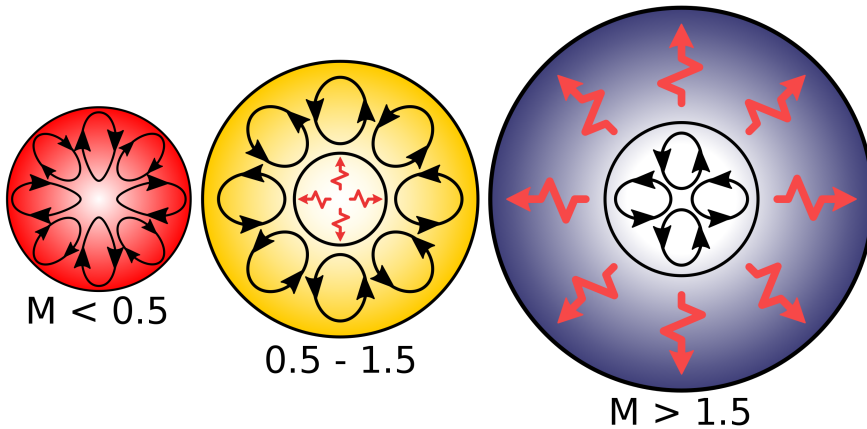


Figure 1.5: Stellar interiors vary based on their mass and spectral type. Low-mass stars, less than half a solar mass, are fully convective from core to surface due to high opacity at low temperatures. Intermediate-mass stars, like the Sun, have a convective region above a stagnant core. Their surfaces retain the same composition as the cloud from which they formed. At 1.5 solar masses, the convective layer almost disappears, and the star becomes fully radiative. Beyond 1.5 solar masses, the CNO cycle dominates energy production, leading to a convective core due to the concentration of energy in the centre. Image source: [commons.wikimedia](https://commons.wikimedia.org/)

Beyond the radiative zone, the convective zone, which is driven by plasma convection, spans from $0.7 R_{\odot}$ to $1.0 R_{\odot}$. Heated plasma rises in the central regions of convection cells, while cooler plasma descends along the edges. The convection zone experiences a rapid temperature decrease and increased opacity due to the formation of neutral hydrogen and helium. Convection instabilities occur at around $0.7 R_{\odot}$, allowing energy to be transported through plasma convection. The radiative zone exhibits rigid body rotation, and the convective zone displays differential rotation. The transition region between the two zones, known as the tachocline, exhibits significant shear. Now, we will focus on the Solar atmospheric layers, as it is the parent star to Earth, and the proximity ensures the study of the star with high resolution and precision.

1.2 Photosphere

The plasma that ascends from the convection zone ultimately reaches a condition where its opacity becomes inadequate to obstruct the escape of radiation.

1. Introduction

Consequently, it expands and experiences radiative cooling, releasing energy to the higher layers. This leads to a local density rise, bringing the plasma back to a state of convective stability (Priest, 2014). The granules, which appear bright in the observations such as Figure 1.6, are upward-moving hot parcels of gas, and the dark intergranular lanes are the cooler downward-moving material. Naturally, the up-drafts are isolated and the downdrafts are connected. The vertical flow is driven by the pressure gradient and gravity. Beyond $1.0 R_{\odot}$, the overlying medium becomes optically thin for electromagnetic radiation, constituting the solar atmosphere. This transition occurs in the photosphere, the visible layer to the naked eye, characterised by numerous granular patterns originating from convection cells in the underlying layer. These cells represent the tops of hot plasma blobs originating from the convection zone and covering most of the solar disk as seen in a quiet sun (QS)⁴ observation in Fig. 1.6. New granules evolve from the disintegrating old granules. Active granules are the ones that undergo the evolutionary cycle of granules: expansion, fragmentation, expansion of fragments, and fragmentation of fragments. The average life span of a granule is 6 minutes. Additionally, mesogranulation is a large-scale extension of granulation, while supergranulation occurs when many granulated paths come together to form large convection patterns (Featherstone and Hindman, 2016; Roudier et al., 2009). Supergranules can be envisioned as an internetwork of granules, which have a lifespan of 1-4 days.

In the photosphere, strong magnetic flux concentrations like sunspots, pores, vortex tubes, tornadoes, faculae, bright regions, and plages can modify the granulation pattern. Sunspots are formed when bundles of intense magnetic fields rise to the solar surface due to magnetic buoyancy. Magnetic loops are formed during emergence, partially inhibiting energy transmission by convection and conduction, as the total magnetic flux through the solar surface is zero. In some cases, only one major visible sunspot may be observed, known as a unipolar sunspot. In this case, the flux of the other polarity is either distributed around the observable sunspot, diminished, located far away, or undetectable. A sunspot is comprised of an umbra (dark central part) and a penumbra (intermediate intensity region), with the Evershed flow representing the radial outflow of penumbral material parallel to the magnetic field. The sunspot shown in Fig. 1.7 is bipolar with one of those being stronger than the other.

The formation and disappearance of sunspots have been observed for centuries and form the basis of the solar activity cycle further described in Chapter 4. Their number fluctuates with an 11-year periodicity, with the solar maximum corresponding to the period of highest sunspot count, which is also associated with more frequent active phenomena such as flares and coronal mass ejections.

⁴The area on the Sun without 'active' phenomena, like sunspots, plages, flares, prominences, CMEs, etc. (further described in this chapter).

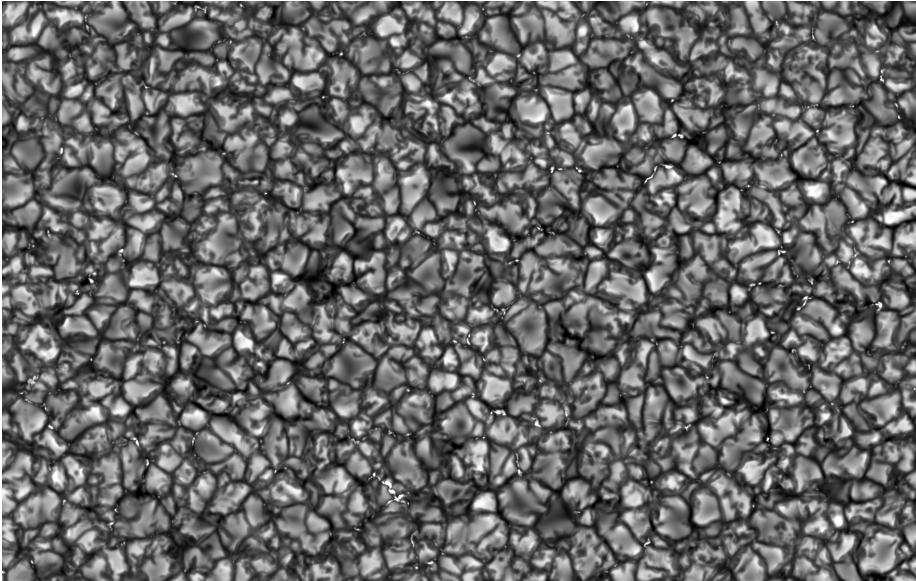


Figure 1.6: A high-resolution wide-band image of the quiet sun photosphere with distinct granulation pattern as observed with the Swedish 1-m Solar Telescope at La Palma, Spain. The area is $49 \text{ Mm} \times 31 \text{ Mm}$, with a resolution of about 28 km/pixel . The area was located close to the disk centre. Courtesy of Luc Rouppe van der Voort.

1.3 Chromosphere

The chromosphere lies just above the photosphere, visible during a solar eclipse as a colourful aura around the covered disk. In solar eclipses, the layer can be seen as a reddish-coloured layer, hence its name derives from the Greek word *chroma* (colour) (Lockyer, 1868). The colour is mostly due to the radiation emitted by neutral hydrogen atoms at 656 nm and the corresponding absorption line is the $H\alpha$ spectral line, which is one of the strongest lines observed in the chromosphere (see [Paper I](#)).

The chromosphere is known to play a crucial role in the heating and mass loading of the million-degree solar corona since most of the energy that drives these mechanisms propagates through this layer. The chromosphere is supposed to be heated due to magnetoacoustic waves. The heating can be due to electric current dissipation and flow accelerating due to waves. Phenomena like Alfvén waves, magnetohydrodynamic waves discovered and formulated by Alfvén, 1947, and nanoflare reconnection events have been discovered (De Moortel and Browning, 2015; Klimchuk, 2015; Parker, 1988; Testa et al., 2013). Still, the propagation and dissipation of the immense energy involved require further study and understanding. Various dynamic energy transport mechanisms are observed, also in synthetic data, later described in [Section 3.3.1.1](#), including,

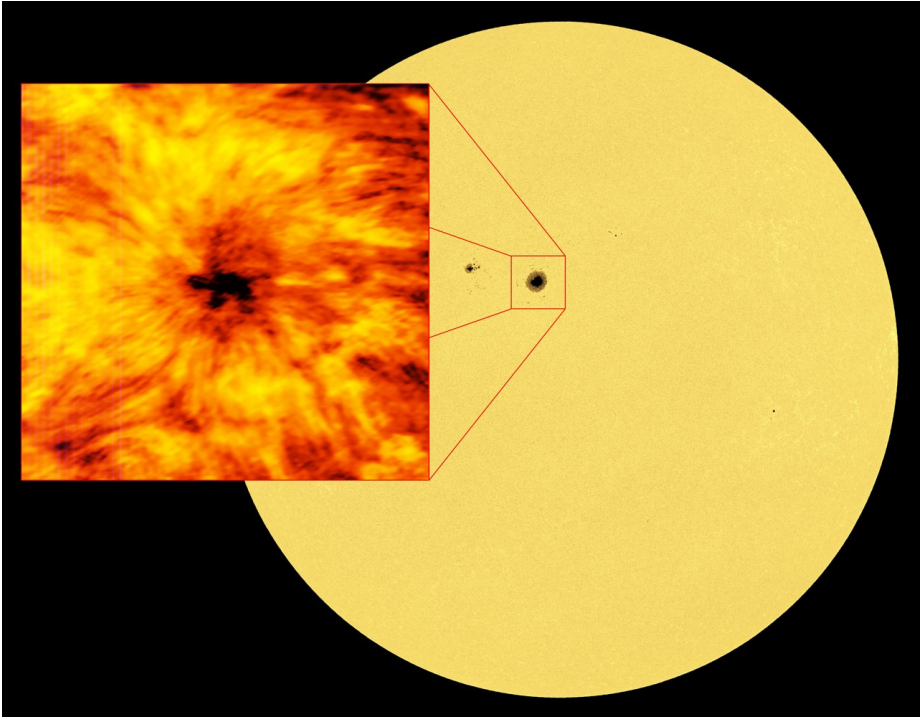


Figure 1.7: The full-disc solar image was taken with the Helioseismic and Magnetic Imager (HMI) on board the Solar Dynamics Observatory (SDO). The image of the full solar disk was taken in the continuum in the red visible part of the spectrum. A cooler, darker sunspot is visible in the disc, and a visual comparison is shown alongside the image from ALMA Band 6 at a wavelength of 1.25 millimetres. Image Credit: [ALMA \(ESO/NAOJ/NRAO\)](#), NASA.

and not limited to, elongated filaments (the long strands of plasma suspended above the Sun by magnetic forces) (Schmieder, Raadu, and Wiik, 1991), spicules (the short-lived, relatively small radial jets of gas in the chromosphere or lower corona) (De Pontieu, Erdélyi, and James, 2004), macrospicules (long jets of chromospheric plasma), spicular upflow (Withbroe and Noyes, 1977), mottles, short fibrils (short-lived and dynamic hairy vertical filaments) and long fibrils (long-lived and horizontal) (Hansteen et al., 2006), and magnetic tornadoes (Wedemeyer-Böhm et al., 2012). The chromosphere holds clues to the answer to the coronal heating question, as the energy needed to heat the corona should be transported through it from the solar interior. Although not reaching the same high temperatures as the corona, the chromosphere requires more energy per unit volume to increase its temperature compared to the corona due to its higher density.

In order to understand the chromosphere completely, there are many factors to consider, such as its highly dynamic nature encompassing plasma heating and

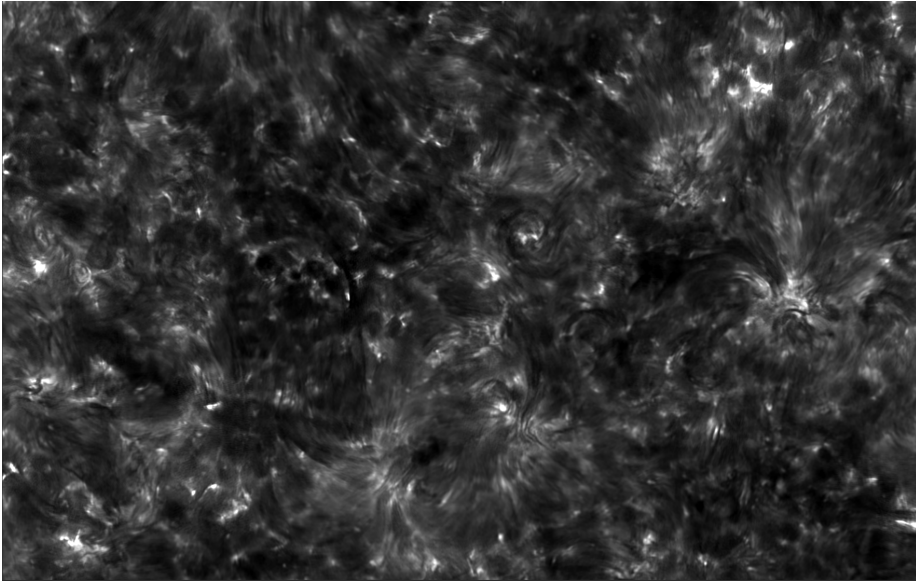


Figure 1.8: High-resolution Ca II H core image observed at the same observation with the same technical configuration as in Figure 1.6. It shows a quiet sun chromosphere with magnetic network regions with (short) chromospheric fibrils and internetwork regions with weaker magnetic fields. Courtesy of Luc Rouppe van der Voort.

cooling processes that unfold across spatial and temporal scales that present challenges for direct observation (Carlsson, De Pontieu, and Hansteen, 2019; Wöger, Wedemeyer-Böhm, and Rimmele, 2009). Figure 1.8 shows a high-resolution picture of the Sun taken with the Swedish Solar Telescope (SST) in the Ca II H line core which captures the mid-upper and lower chromosphere, respectively. Furthermore, in this zone, the β parameter of the plasma (the ratio between the gas pressure and the magnetic pressure) changes from greater than 1 to less than 1 and the plasma goes from partially ionised to fully ionised. Unlike the photosphere in which the radiation can be considered to be transported in a Local Thermodynamic Equilibrium (LTE), the non-thermal processes dominate the chromosphere. There are a large variety of different features co-existing at different spatial scales. This complexity of the chromosphere makes its modelling more difficult. However, because of its intrinsic dynamic nature, there exist variations depending on local magnetic field strength and therefore the ionisation degree can vary strongly.

As seen in Fig. 1.4 of the semi-empirical 1D model of a stratified atmosphere by VAL (Vernazza, Avrett, and Loeser, 1981), the onset of the chromosphere is marked by an increase in the temperature beyond the temperature minimum, which appears to be a region in which the temperature increases monotonically from the minimum of 4300 K at 500 km in height, until it reaches a height

1. Introduction

of about 2000 km, to then increase drastically to 10^6 K in just about 100 km in the so-called transition region (Linsky, 2017). The chromosphere can also be conceptualised as a region where, as the cooling agents, like Mg^+ , Ca^+ , Fe^+ , deplete at the temperature minima, the temperature rises, ionising these species further. The VAL 1D semiempirical model suggests that this layer is roughly 1500 km thick, and is largely homogeneous, which can be used as a first approximation. However, the observations and advanced simulations reveal that the chromosphere is highly dynamic with variations on small spatial and temporal scales, which makes it difficult to define precise heights for the lower or upper boundaries. However, the average extent of the chromosphere can be estimated to be between roughly 0.5–2.5 Mm. Based on abundant observations in the past (Rutten, 2007), and from the high-resolution observations, such as the one in Figure 1.8, it is clear that the chromosphere is not only far from homogeneous, but it is also very dynamic. Therefore, as suggested by Carlsson, De Pontieu, and Hansteen, 2019, current numerical modelling attempts rely on physics-based definitions of the solar chromosphere rather than purely geometrical arguments⁵.

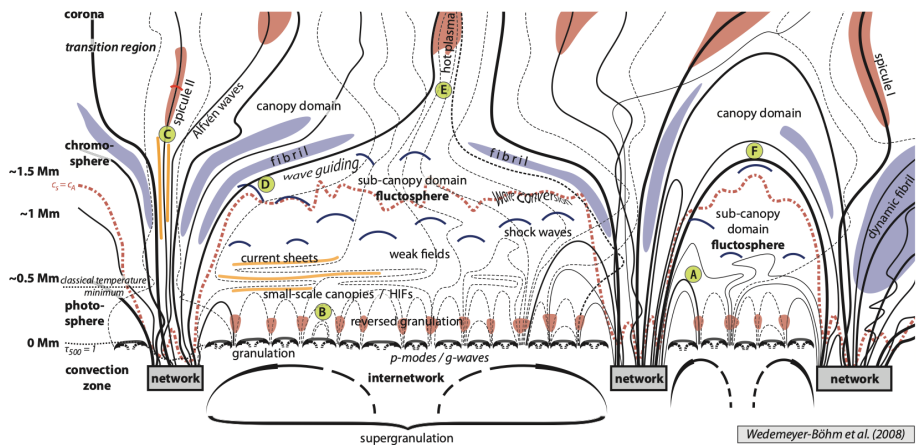


Figure 1.9: The global picture of the structure of solar atmosphere: the different layers in the solar atmosphere, different physical phenomena as a function of height. Image Credit: Wedemeyer-Böhm, Lagg, and Nordlund, 2009

Figure 1.9 provides a schematic representation of the diverse phenomena taking place within the solar chromosphere depicting a network-internetwork region. The regions where the plasma β changes (indicated by the pink dashed line), signify the dominance of the magnetic field. They also serve as conduits for various phenomena such as spicules, Alfvén waves, fibrils, and magnetohydrodynamic (MHD) waves. Additionally, below the canopy region, other phenomena occur including shock waves, vortex flows, and current sheets. It is highly probable that the combined effect of these phenomena is responsible for supplying sufficient energy to sustain the hot chromosphere. It is important

⁵physical properties like temperature, density, electron density based on height

to note that the actual 3D magnetic field structure in the solar atmosphere is considerably more intricate. Consequently, observing and interpreting any given phenomenon entails a high level of complexity and necessitates the simultaneous use of multiple diagnostic tools, such as observations in various wavelengths and the utilisation of simulated models whenever feasible.

1.4 Transition Region and Corona

In [Figure 1.4](#) we can see that the temperature is swiftly increasing from roughly 8000 K to 30,000 K over a short distance of approximately 100 km. This region, known as the transition region (TR), exists between the chromosphere and the corona. Within the TR, the plasma experiences a significant shift from chromospheric to coronal temperatures. Although the TR exhibits high temperatures (lower than those of the solar corona), most of the hydrogen becomes ionised, resulting in the dominance of emission spectral lines from heavier elements like carbon, oxygen, silicon, and magnesium. These ions can exhibit ionisation states ranging from +1 to +8, indicating temperatures as high as 100,000 K (Peter, Gudiksen, and Nordlund, 2004). The radiation emitted by these ions primarily falls within the ultraviolet part of the electromagnetic spectrum, necessitating space-based observations, similar to those conducted for the corona.

The solar corona represents the outermost layer of the solar atmosphere, visible to us, only during a solar eclipse. The temperature of this layer is significantly hotter (by several orders of magnitude) than the average temperature of the photosphere. In terms of thickness, it extends from the top of the chromosphere and stretches into the solar wind, filling the entire heliosphere. Despite its extremely high temperature, the radiation from the corona is approximately a million times dimmer than that of the photosphere, primarily due to the extremely low plasma density in this region. Numerous spectral lines of ions of heavier elements such as carbon, oxygen, silicon and magnesium with higher ionisation states that suggest temperatures in this region can reach at least a million Kelvin (Edlén and Swings, 1942; Grotrian, 1939; Peter, Gudiksen, and Nordlund, 2004; Priest, 2014).

The coronal plasma is $10^4 - 10^7$ times less dense than the photosphere. The so-called chromospheric-coronal heating puzzle does not revolve around high temperatures but rather the high heat capacities of the plasma. Plasma can possess multiple temperatures simultaneously. Ions and electrons exhibit distinct Maxwellian distributions with different temperatures. Same species collision rates are higher than collision rates between different species like ions and electrons (Hernandez and Marsch, 1985). In the presence of a magnetic field, even a single species can exhibit two distinct temperatures. This occurs due to the differential effects of B_{\parallel} and B_{\perp} , leading to the separation of velocity components into distinct Maxwellian distributions – one parallel and the other perpendicular to the magnetic field. Due to the low density of plasma in the corona, the heat capacity is small. Therefore, high temperatures do not necessarily imply

1. Introduction

extremely high heat or energy content.

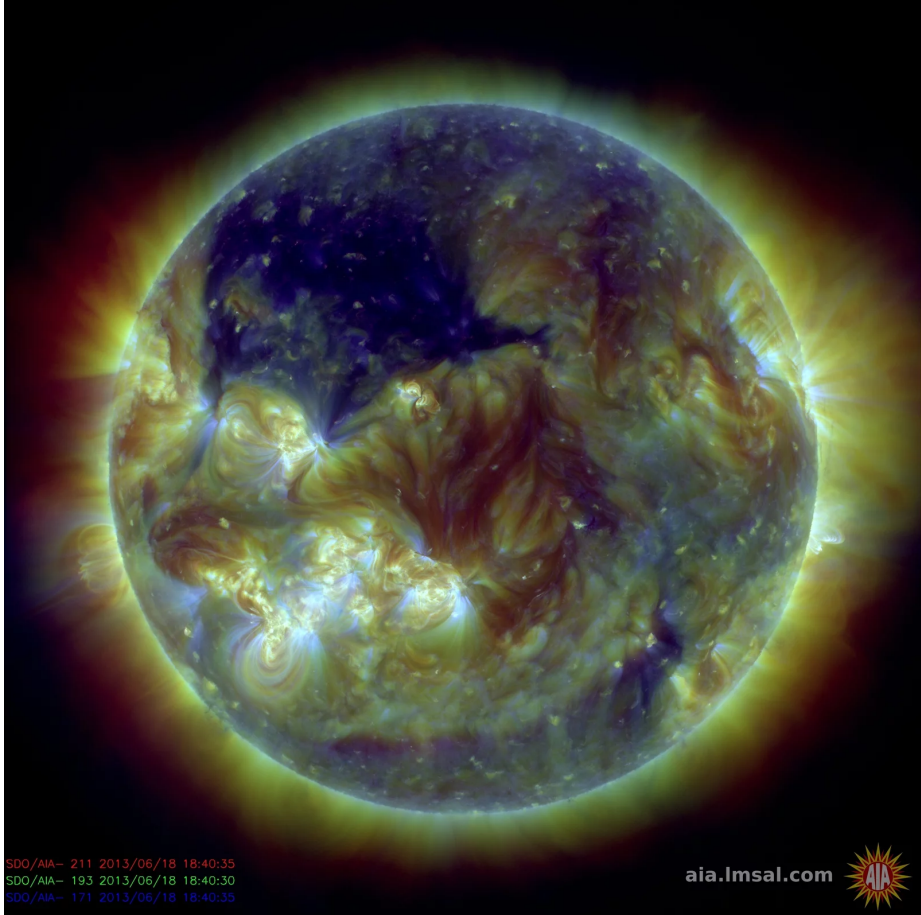


Figure 1.10: The composite image of the solar corona, created using three different passbands, is displayed as an RGB composition. The red colour represents the 211 Å passband, which is formed at temperatures around 2 million Kelvin. The green colour represents the 193 Å passband, corresponding to temperatures of approximately 1.3 million Kelvin. Lastly, the blue colour represents the 171 Å passband, formed at around 800,000 Kelvin. This image was captured using NASA’s SDO/AIA instrument. Image Credit: Heliophysics Events Knowledgebase, Lockheed Martin Solar and Astrophysics Lab, Palo Alto.

There are three wavelength channels in [Figure 1.10](#), two of which sample temperature regimes exceed 1 million degrees K, namely 193 Å and 211 Å, showing a representative image of the solar corona. The coronal layers exhibit a variety of phenomena that fluctuate in intensity and frequency because of solar activity, which is discussed further in [Chapter 4](#). Various eruptive events occur in the coronal region, including flares, prominences, radio bursts,

coronal holes (Cranmer, 2009), coronal mass ejections (CMEs), coronal X-ray jets (Shibata et al., 1992; Sterling et al., 2015), filament eruptions, and more (see for eg. Aschwanden, 2002; Wedemeyer-Böhm, Lagg, and Nordlund, 2009). Flares represent chromospheric eruptions characterised by a sudden increase in brightness followed by a slow decay. They involve a mixture of high-energy particles and heated plasma. Flares typically exhibit different phases, including a pre-flare phase lasting 10-30 minutes, an impulsive phase lasting 10-100 seconds, a rise or flash phase lasting 5-60 minutes, and finally the main phase. Flares have a multi-waveband response and their nature is different in different bands, and high energy emissions tend to coincide temporally with the rate of rise of lower-energy (soft) X-ray emission (Neupert, 1968; Veronig et al., 2005). Prominences are dark, thin, and elongated filaments that are significantly denser than the surrounding corona. They originate within the corona but extend outward, becoming embedded in it. Radio bursts are caused by energetic electrons via various emission mechanisms under different conditions that propagate outward through the corona. Depending on formation mechanism and energy outputs these were classified into 5 types in 1960's (Wild, Smerd, and Weiss, 1963). Type III bursts, described in the review by White, 2007, are studied in detail for the impact on space weather described further in Section 1.5. Coronal mass ejections (CMEs) are accompanied by eruptive prominences and flares, with velocities ranging from approximately 10^5 to 10^6 m/s. These events involve the release of significant amounts of magnetic energy. Coronal waves (Afanasyev and Zhukov, 2018) and Moreton waves (Moreton, 1960) are large-scale transient disturbances in the coronal region. Their speeds, of the order of 1 Mm/s, exceed the sound speed in the corona, resulting in the generation of fast magnetoacoustic shocks to release magnetic energy. Within coronal loops, the plasma undergoes processes of heating, evaporation, cooling, and draining (Ionson, 1978; Pettit, 1943). Since the plasma density is extremely low, the magnetic fields govern the environment of this layer. These energetic processes contribute to the overall dynamics and behaviour of the coronal plasma.

1.5 Solar Wind and Space Weather

The heliosphere, the vast influence region around the Sun, stretches well beyond Pluto's orbit. The corona generates solar wind, which consists mainly of charged particles, including electrons, protons, α particles and more (Formisano and Moreno, 1971; Noble and Scarf, 1963; Signer, Eberhardt, and Geiss, 1965). The solar wind interacts with the interplanetary atmospheres within the solar system and can impact space weather around Earth and other planets. We constantly experience the impact of the Sun's magnetic field and the solar wind, so studying solar-stellar activity is of utmost importance.

As the solar wind reaches Earth, our magnetic field shields us from highly ionised plasma particles (Beard, 1964). Efficient coupling between the solar plasma and our magnetic field leads to some plasma draining on Earth's day side, with some travelling to the night side as seen in Figure 1.11. Particles

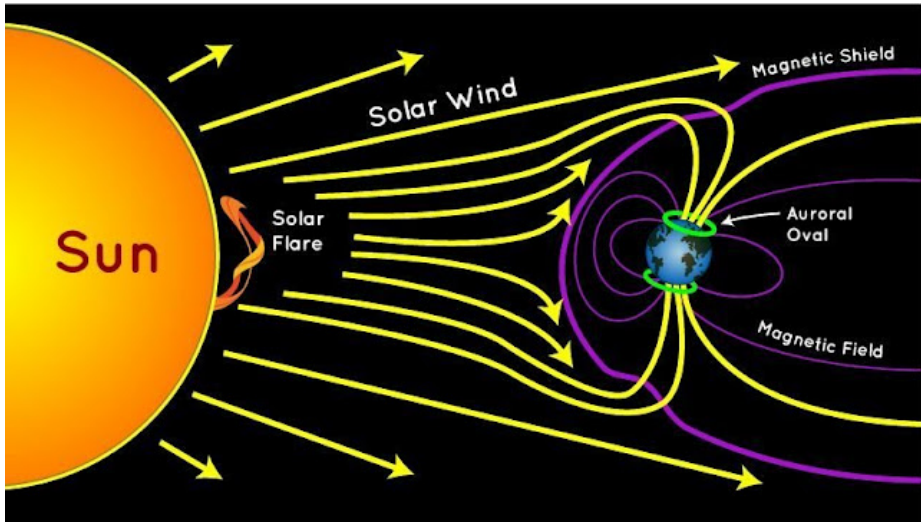


Figure 1.11: The illustration shows the interaction between the magnetic fields of the Sun and the earth along with the possibility of flares and solar wind directed towards the earth. The particles will eventually be directed to the auroral ovals. Image Credit: Chukwuma Anoruo, University of Nigeria, Nsukka obtained from the [PAGES Early-Career Network \(ECN\) blog](#)

reaching the night side force the magnetic field to snap back, propelling them toward the magnetic poles. In the ionosphere, they interact with nitrogen and oxygen ions, creating beautiful auroras.

The solar wind and activity, further described in [Chapter 4](#), affect the space weather in different ways. But it also affects satellites, communication, power grids, and navigation systems. It interferes with the signals, stops the satellites from working and in extreme cases, damages the machinery in the satellites (Horne et al., 2018). These stellar winds, if stronger, could also affect the possibility of life on exoplanets. The magnetic field of the earth plays an important role in saving us from these frantic attacks of ionised particles and hot high-speed plasma.

The solar atmosphere is described in this chapter with sufficient details in order to motivate the understanding of the problem statement of the thesis. In the next chapter, we will learn how the energy from the Sun's interior is converted into radiation in the solar atmosphere, which propagates to the Earth, allowing us to observe it. The majority of solar physicists use observations of the Sun from modern instruments with a high spatial, spectral and temporal resolution, along with state-of-the-art simulations, which is elaborated in [Chapter 3](#). In [Chapter 4](#) I have attempted to describe the variation in the activity of the Sun and how the activity is quantified in the case of distant stars. In conclusion, the [Chapter 5](#) provides an overview of the three papers that form the basis of this thesis, as well as concluding remarks and future research possibilities.

Chapter 2

Formation Mechanisms for Radiation

Solar spectral lines have been a critical tool in analysing and interpreting the solar atmosphere ever since they were first detected by Hyde Wollaston, 1802. As discussed in [Section 1.3](#), observing the solar chromosphere poses challenges due to the overwhelming brightness of the photosphere, despite the chromosphere being approximately 1500 km thick on average. In essence, the medium is mostly transparent to continuum radiation. Until recently, high-resolution observations of the chromosphere were primarily limited to specific spectral lines that serve as diagnostic tools, such as $H\alpha$, Ca II H & K lines, Ca II IR triplet, and Mg II h & k. As Richard Feynman wrote in *The Relation of Physics to Other Sciences*, "*The most remarkable discovery in all of astronomy is that the stars are made of atoms of the same kind as those on the earth.*"

The spectral lines are formed in the solar atmosphere through various processes involving the interaction of photons and particles, including spontaneous emission, induced emission, radiative excitation (absorption), photo-ionisation, and collisional transitions. The transfer of energy via electromagnetic radiation is called radiative transfer. In the chromosphere, spectral lines are formed outside of LTE, meaning they are decoupled from the local conditions of the medium where they originate. Consequently, the use of inversion codes is necessary to model the atmosphere based on the observed data. This approach has proven to be a valuable tool for characterising the chromosphere. However, it has a significant limitation: it requires incorporating realistic approximations for all relevant physical processes to accurately reproduce the observations. Additionally, depending on the desired complexity of the model employed, the computational cost can be substantial. Many spectral lines and their supposed formation heights are illustrated by Vernazza, Avrett, and Loeser, 1981 shown in [Figure 2.1](#).

In addition to the spectral lines, the chromosphere also emits continuum radiation in the millimetre range, which is assumed to be formed under LTE conditions, and which would complement the description of the solar atmosphere at chromospheric layers. However, this diagnostic tool has been used only with limited spatial and temporal resolution. Fortunately, nowadays, ALMA provides sufficient temporal and spatial resolutions to study chromospheric dynamics. This chapter depicts the physics behind the emission at millimetre/sub-millimetre (mm/sub-mm) wavelengths. A more detailed description of the processes demonstrated in this chapter can be found in (Hubeny and Mihalas, 2014; Krüger, 2012; Nindos, 2020; Rybicki and Lightman, 1986; Wedemeyer et al., 2016).

2. Formation Mechanisms for Radiation

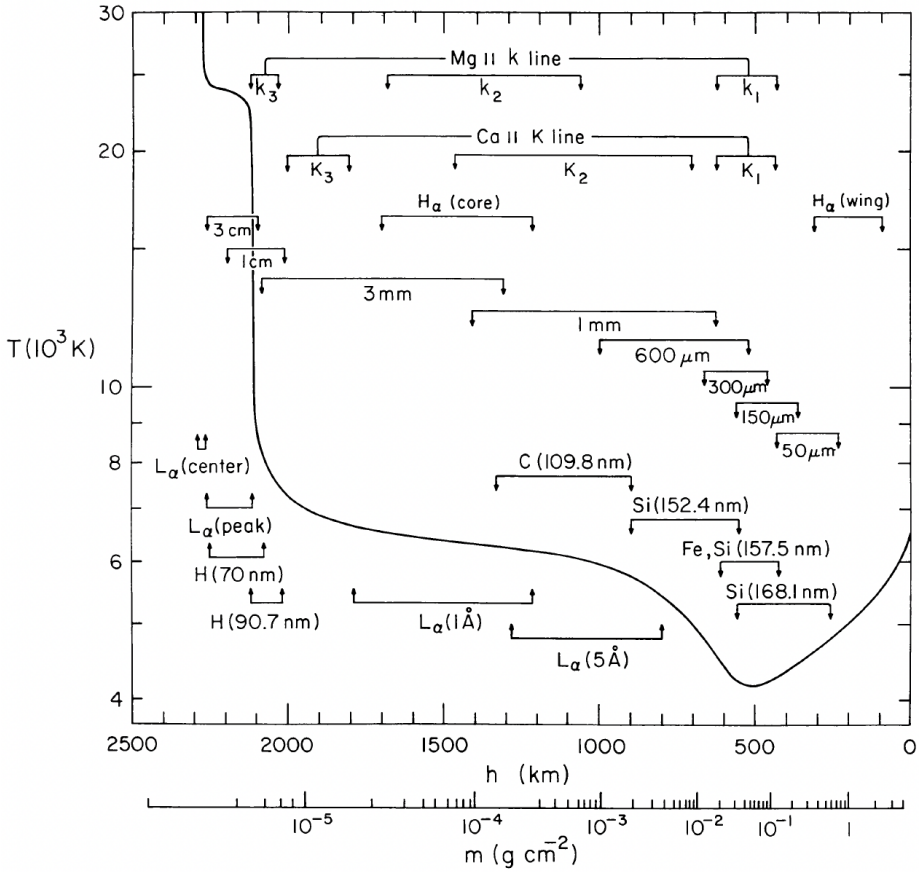


Figure 2.1: The temperature distribution in the solar atmosphere can be described based on the widely recognised VAL semi-empirical model. The photosphere extends up to approximately 500 km in height. Beyond 500 km and up to around 2000 km, the temperature increases, marking the presence of the chromosphere. The transition region, located beyond 2000 km, exhibits a rapid temperature rise, serving as the boundary between the chromosphere and the extremely hot corona, which reaches temperatures in the millions of degrees. Various atomic species are responsible for the observed spectral lines, marked on the plot, each indicating a specific ionisation state and average formation heights. Image credit: Vernazza, Avrett, and Loeser, 1981

2.1 Continuum Radiation

ALMA (Atacama Large Millimetre/sub-millimetre Array; discussed in Section 3.2) offers a valuable new tool for solar observations in the mm continuum. As a result of free-free emission, the solar atmosphere emits continuous radiation at millimetre-submillimetre wavelengths. This occurs when electrons interact

with ionised atoms carrying a positive charge. The non-quantised energies of unbound electrons permit the emission of radiation across a wide range of energies, resulting in a continuous spectrum. The free-free radiation process is thermal and can be assumed to happen within the framework of local thermodynamic equilibrium (LTE). LTE radiation follows the spectral distribution of a black body, as defined by Planck's law. The source function S_ν can be equated to the spectral irradiance B_ν of the black body at a temperature T as,

$$S_\nu = B_\nu(T) = \frac{2h\nu^3}{c^2} \frac{1}{e^{\frac{h\nu}{k_B T}} - 1}, \quad (2.1)$$

where ν is the frequency of light, h is Planck's constant, c is the speed of light, k_B is Boltzmann's constant and T is the local temperature of the plasma (Rutten, 2003). At millimetre and sub-millimetre wavelengths (0.3 mm to 8.5 mm: the theoretical range of ALMA) it is possible to use the approximation given by the Rayleigh-Jeans limit ($h\nu \ll k_B T$), which implies that

$$e^{\frac{h\nu}{k_B T}} \approx 1 + \frac{h\nu}{k_B T}. \quad (2.2)$$

Hence, Planck's function described in Equation (2.1) can be simplified as

$$B_\nu(T) = \frac{2k_B}{c^2} T\nu^2. \quad (2.3)$$

By employing the Radiative Transfer Equation (RTE), one can determine the specific intensity I_ν . The intensity is obtained by integrating the source function $B_\nu(T)$ with respect to the optical depth τ along the line of sight.

$$I_\nu = \int_0^{\tau_{\max}(\nu)} B_\nu(T(\tau')) e^{-\tau'} d\tau', \quad (2.4)$$

where, τ_{\max} represents the maximum range of optical depth for the frequency ν where substantial contributions to the source function occur. Typically, in optically thick scenarios, τ_{\max} is considered to be infinite ($\tau_{\max} = \infty$). This specific intensity I is integrated over the angular area dW to get the flux density F

$$F = \int I(\nu) dW \quad (2.5)$$

which is just power per unit area for a given frequency, observable in radio astronomy. Considering this, in the field of radio astronomy, the brightness temperature, denoted as T_b , is defined as the temperature of a black body that generates an equivalent intensity to the observed value. The brightness temperature is also readily derived from the directly detected flux in radio telescopes (refer to Chapter 3 for more details).

$$T_b = \frac{c^2}{2k_b\nu^2} I_\nu = \frac{\lambda^4}{2ck_B} I_\lambda \quad (2.6)$$

2. Formation Mechanisms for Radiation

Observations provide a sampling of the local plasma conditions and offer a direct measurement of its electron temperature. Consequently, the direct relationship between specific intensity denoted as I_ν , and brightness temperature, denoted as T_b , is the key factor that makes millimetre/sub-millimetre radiation a valuable diagnostic tool. This facilitates a straightforward interpretation of the observations, despite the potential influences of deviations in hydrogen ionisation equilibrium or departures from the Maxwellian distribution of electron velocities. Although these effects are typically considered small, they could still be detectable, and it is not feasible to separate the individual contributions to the observed temperature in a straightforward manner (Wedemeyer et al., 2016). To gain a better understanding of the impact of these effects, it is crucial to study them through 3D numerical simulations, which are addressed in Section 3.3.1.1.

2.2 Formation Heights of the mm radiation

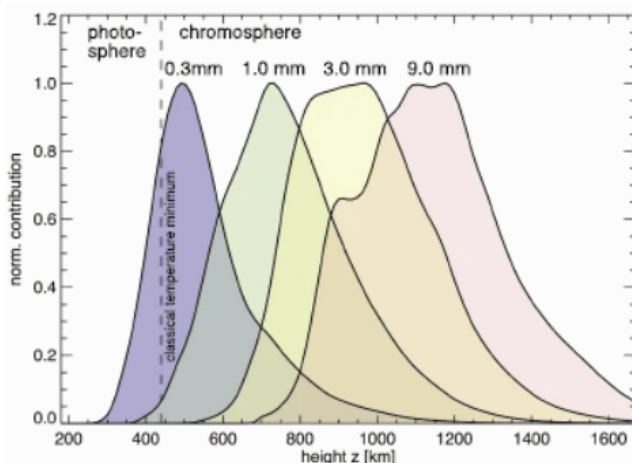


Figure 2.2: The average contribution functions of the continuum mm intensity, at the different heights in the solar atmosphere, as a function of height. Credit: Wedemeyer et al., 2016.

The Sun emits mm and sub-mm continuum radiation primarily from the chromosphere, as depicted in Figure 2.1 (Vernazza, Avrett, and Loeser, 1981; Wedemeyer et al., 2016). The formation height of this radiation varies with wavelength due to opacity, with longer wavelengths corresponding to higher average formation heights. In static classical 1D models like VAL (Vernazza, Avrett, and Loeser, 1981) and FAL (Fontenla, Avrett, and Loeser, 1993) the formation height does not vary, but it is influenced by the small-scale dynamical structure in dynamic 1D, 2D, and 3D models.

In addition to the intensity's linear dependence on temperature, the millimetre radiation also depends on the observed wavelength. Specifically, the opacity

Band/ λ	LTE	NE ionisation	Wedemeyer-Böhm et al., 2007	Loukitcheva et al., 2015
3 / 3.0 mm	1.8	2.8	0.96	1.5
6 / 1.2 mm	0.9	2.7	0.73	0.9

Table 2.1: Average formation heights (in Mm) of the mm continuum formed in chromosphere as calculated by Martínez-Sykora et al., 2020 based on 2D atmospheric models with different methods for treating the ionisation balance: (i) in LTE and (ii) non-equilibrium for hydrogen and helium compared with the results from Wedemeyer-Böhm et al., 2007 and Loukitcheva et al., 2015

increases with wavelength. Consequently, changing the observed wavelength alters the height from which the radiation originates. In general, wavelengths close to 0.5 mm primarily originate near the temperature minimum region, while a wavelength of 10 mm corresponds to radiation originating near the transition region (see Figure 2.1). Thus, observing the Sun in the millimetre range can act as a thermometer to map the local plasma conditions and construct a 3D tomography of the solar chromosphere (Wedemeyer et al., 2016). However, there are challenges associated with this approach. The formation height of the radiation only indicates where the atmosphere becomes optically thick at the observed wavelength, while the plasma along the observed line of sight (LOS) can contribute in a non-uniform manner depending on the plasma properties. These contributions are described by the contribution function $CF(h)$. This function quantifies the contribution of each height in an observation column to the observed intensity (Morgachev et al., 2020).

Numerical simulations and radiative transfer calculations have been used to investigate the contribution function for millimetre radiation in the solar atmosphere, which are summarised in Table 2.1. Wedemeyer-Böhm et al., 2007 conducted numerical modelling of the quiet sun using three-dimensional (3D) simulations and estimated the formation heights. The wide contribution functions seen in Figure 2.2) for each wavelength indicate that the intensity is the sum of the contributions along the LOS. These wide ranges of formation heights are consistent with radiative transfer calculations based on other numerical models. Loukitcheva et al., 2015 used the Bifrost enhanced-network 3D model (see Chapter 3). The higher average heights compared to Wedemeyer-Böhm et al., 2007 can be attributed to the presence of canopies formed by magnetic field loops in the chromosphere, which exhibit increasing optical thickness with longer wavelengths (Eklund et al., 2021).

Treating the plasma in local thermodynamic equilibrium (LTE), in Martínez-Sykora et al., 2020 reported average formation heights that align with the previous findings. However, the approach with non-equilibrium (NE) ionisation of H and He yielded significantly higher average formation heights at both $\lambda = 1.2$ mm and $\lambda = 3.0$ mm. There is a negligible difference in average formation height between $\lambda = 1.2$ mm and $\lambda = 3.0$ mm (around 0.11 Mm). Consequently, the continuum radiation at both wavelengths is optically thick and samples similar

2. Formation Mechanisms for Radiation

structures at high altitudes. This contradicts observations and the results based on the Bifrost 3D model (Eklund et al., 2021; Loukitcheva et al., 2015)) might be caused by the restrictions due to 2D. Loukitcheva et al., 2004 demonstrated that the formation height varies significantly at mm-wavelengths in a time-dependent 1D simulation involving propagating shock waves that disturb the chromosphere. Observing comparable structures at the mm wavelengths, as presented in the 2D simulations by Martinez-Sykora et al., 2020, would provide valuable constraints to assess the realism of the models. This potentially improves their ability to reproduce millimetre observations. In this context, observations of features with presumably large formation heights, such as magnetic loop structures reported by Wedemeyer et al., 2020, could provide further clarification.

The presence of the magnetic field also affects the formation height. For instance, just above footpoints of these enhanced network loops, where the brightness temperature is enhanced, the peak in the contribution function appears at heights of about 1300 km for $\lambda = 1.2$ mm and 1600 km for $\lambda = 3.0$ mm in the Bifrost model based on the enhanced network. Therefore, the formation height appears to be larger in these regions compared to quieter areas (see Panel C in Figure 5 of Loukitcheva et al., 2015). Additionally, the formation height can change over time, influenced by the propagation of shock waves, MHD waves, or even the occurrence of flares. Accordingly, relative height differences between layers where radiation originates at mm millimetre wavelengths would not differ significantly within the relevant height range if the whole atmosphere is similarly affected. To use this to our advantage, we use synthesised and observed mm data to get better insights into the chromospheric temperature stratification. In the next chapter, I will touch upon the choice of instruments and simulation models used in this thesis.

Chapter 3

Instruments and Simulations

In different layers of the Sun, different wavelengths of radiation are emitted depending on the composition of the atmosphere, the opacity and the physical processes contributing at different heights and the amount of energy propagating through it. Consequently, based on the wavelength of radiation we can look at different layers of the Sun. The namesake of the Hubble telescope, Edwin Powell Hubble, said in *The Nature of Science* "*Equipped with our five senses – along with telescopes and microscopes and mass spectrometers and seismographs and magnetometers and particle accelerators and detectors sensitive to the entire electromagnetic spectrum – we explore the universe around us and call the adventure science.*"

Different wavelength regimes require different observation techniques and instruments. The solar telescopes used for ultraviolet (UV), optical to near-infrared (NIR) wavelengths have been in use for a long time in both, (i) ground-based, like the Swedish Solar Telescope (SST), Udaipur Solar Observatory, Goode Solar Telescope, etc and (ii) space-based, like, Solar Dynamics Observatory (SDO), Interface Region Imaging Spectrograph (IRIS), Solar Orbiter, Parker Solar Probe (PSP), and upcoming Multi-slit Solar Explorer (MUSE). Earth's atmosphere mostly blocks UV and extreme ultraviolet (EUV) wavelengths, and atmospheric turbulence degrades ground-based solar observations. While space-based telescopes offer unobstructed views, their operation costs are considerably higher than ground-based telescopes, and they face limitations in terms of size due to cost and telemetry constraints. Yet all telescopes mentioned above share the same conceptual structure: light from the Sun reaches the observatory, passes through the optical assembly and hits the detector, which measures the intensity. On the other hand, the far infrared to the high-frequency regime, the submillimetre and radio wavelengths are observed in different manners, described in [Section 3.2](#). The primary submillimetre data used in this thesis is from the Atacama Millimetre-submillimetre Array (ALMA). Millimetre and radio data from another radio observatory in Japan, Nobeyama Radio Observatory are used in [paper III](#).

In solar physics, numerical simulations have become as crucial as observations, especially in recent times. Observations have unveiled the dynamic and non-equilibrium nature of the solar atmosphere, making interpretation challenging. Therefore, simulations play a vital role in understanding the underlying physics behind these observations. However, simulating the solar atmosphere (or a part of it) can be computationally demanding, particularly in 3D geometry, and may even surpass current computational capabilities (Leenaarts, 2020). Nonetheless, advanced simulations are pivotal in interpreting existing observations and, at times, predicting new ones. Over the past two decades, various simulation

3. Instruments and Simulations

codes, such as Stagger (Stein and Nordlund, 1998), MURaM (Vögler et al., 2005), Bifrost (Gudiksen et al., 2011) and COBOLD (Freytag et al., 2012), have been developed to model solar and stellar atmospheres in 3D geometry. The simulations used in this thesis are described in Section 3.3.

3.1 Optical Observations

Our Sun is not a first-generation star as described in Chapter 1. So, it is formed from the dust of previous stars and hence, it contains higher elements with very low abundance (Asplund, Amarsi, and Grevesse, 2021). These can be used to study the thermal profiles. The solar spectrum in the optical range from 400 to 700 nm is shown in Figure 3.1.

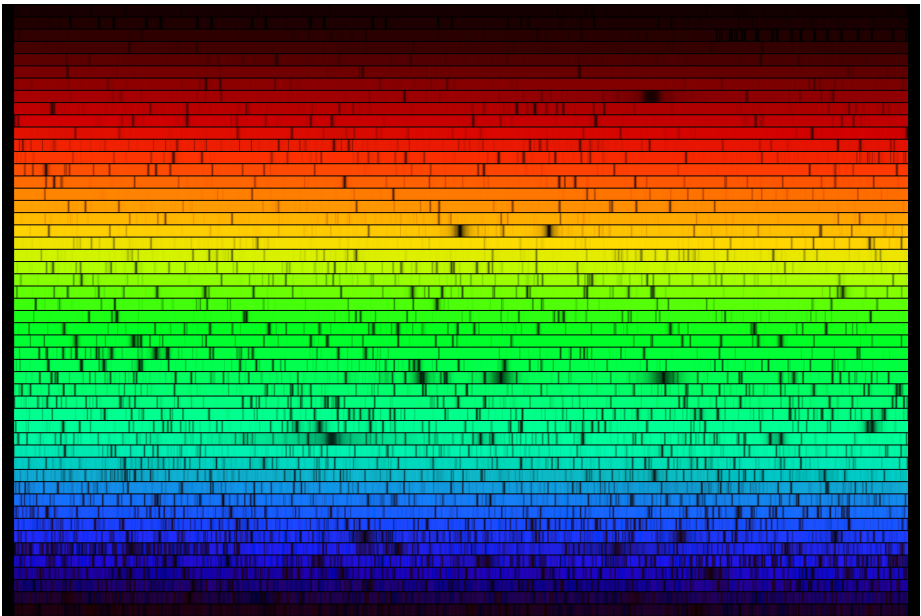


Figure 3.1: This high-resolution spectrum of the Sun was obtained from a digital atlas observed with the Fourier Transform Spectrometer (FTS) at the McMath-Pierce Solar Facility at the National Solar Observatory on Kitt Peak, Arizona. The image resembles an echelle spectrum, with wavelength increasing from left to right and from bottom to top. Each of the 50 slices covers 6 nm, providing a complete spectrum across the optical range from 400 to 700 nm. Image Credit: N.A.Sharp, NOAO/NSO/Kitt Peak FTS/AURA/NSF

The outer part of the observed solar disk is called the limb. While observing the phenomena from the limb, the atmosphere is tilted with respect to the observer. The light rays have to travel farther through solar atmospheric layers to reach the observer because the line of sight (LOS) has already increased by the stellar radius compared to the disk centre. Hence, the optical depth reaches

unity at a slightly greater height in the atmosphere depending on the angle of inclination. Effectively, in theory, the layer observed is higher for a tilted atmosphere than the unslanted one. This phenomenon is crucial in chromospheric studies as the temperature reaches a minimum and depending on the wavelength, the layer observed can be above or below the temperature minimum. So, the limb can get brighter in the case of upper chromosphere, and darker in the case of lower chromosphere.¹ These limb effects are seen in the full disk images of the Sun in different wavelengths shown further in [Figure 3.7](#).

The places where the spectrum is darker are absorption lines and many of these, like Ca II H&K, H α , and Mg II h&k, are observed for a long time (Hearnshaw, 1986). It happens that the core and the wings of the spectra form at different heights and this gives us insights into the variation in the temperature of those layers. Small filters observe precise heights in the chromosphere and hence, the full disk images will have limb brightening. But the broader filter will start to have contributions from the photosphere which has higher intensity, hence photospheric contributions will dominate. As the temperature decreases with height in the height range of upper photosphere - lower chromosphere, as seen in [Figure 2.1](#), limb darkening will be seen. The telescopes with which the spectra are observed are extremely sensitive. They can sense the Doppler shift in the spectral lines due to outflows or shocks having a velocity of the order of tens of km/s. The evolution of shocks can thus be traced. In this thesis, H α and Ca II lines have been used as diagnostics for chromospheric activity. We will delve into these spectral lines more specifically in [Section 3.3](#).

In this thesis, the solar optical observations used are mainly from IBIS, IRIS, and the Atmospheric Imaging Assembly (AIA) and Helioseismic and Magnetic Imager (HMI) instruments onboard SDO. Along with these, the optical and infrared spectra used in [paper I](#) and [II](#) for a Sun-like star α Cen A are acquired from [Lorenzo-Oliveira et al., 2016](#). These observations are collected at Observatório do Pico dos Dias (OPD), operated by the Laboratório Nacional de Astrofísica (LNA), CNPq, Brazil on the ESPCOUDE 1.60 m telescope.

3.2 Interferometric Observations

The distant sky source produces spherical waves at the source, which become plane waves, get altered by the earth's atmosphere, and then reach the observatory. The full sky source is a superposition of many emitting regions all producing plane waves. What we get is an infinite series of plane waves at the telescope - a Fourier series. The final image is the Fourier transform of all these series elements observed by the aperture.

To get bigger apertures and images with higher resolution, radio astronomy employs an aperture constructed from scattered dishes. Thus, the principle of radio interferometry hinges on the concept of aperture synthesis, a technique aimed at creating an extensive effective aperture through the utilisation of a

¹<https://www.astro.uvic.ca/~tatum/stellatm/atm6.pdf>

3. Instruments and Simulations

finite set of small aperture radio antennas strategically distributed in space. The size of the aperture is governed by the greatest separation between the antennas.

These Fourier components are determined by the baselines, representing the distances between pairs of telescopes and the orientation of the baseline. Each baseline corresponds to a data point in the Fourier space, and a larger number of antennas involved in the observation provides better image reconstruction capabilities. The configuration of the antennas plays a crucial role in the image reconstruction process. The specific arrangement of antennas influences the visibility coverage in the Fourier domain, affecting the quality and resolution of the final image produced by the radio telescope. Therefore, optimising the configuration of the antennas is essential to achieve accurate and high-resolution imaging in radio astronomy.

For N_A number of antennas, the number of Fourier components, or the number of baselines, i.e. the number of pairs of antennas (N_P) is

$$N_P = \frac{N_A(N_A - 1)}{2}. \quad (3.1)$$

The angular resolution θ that can be achieved with a particular configuration of antennas set at the observation scales as

$$\theta = \epsilon \frac{\lambda}{d}, \quad (3.2)$$

where $\epsilon = 1.22$, the wavelength of the radiation (λ) and the diameter of the aperture (d), and can be roughly estimated according to angular resolution = wavelength/synthesised aperture diameter.

3.2.1 Atacama Large Millimetre/submillimetre Array (ALMA)

The Atacama Large Millimetre/sub-millimetre Array (ALMA) is an impressive interferometric array radio telescope, considered the largest ever built in the mm range. Positioned on the Chajnantor plateau in Chile at an elevation of approximately 5,100 meters above sea level, ALMA resulted from a collaborative effort involving ESO, NRAO, NAOJ, Chile and minor partners. This sophisticated array consists of 50 antennas boasting a diameter of 12 meters. The additional Atacama Compact Array (ACA), also known as the Morita Array, consists of twelve 7-m antennas and four 12-m Total Power (TP) antennas. (Iguchi et al., 2009).

The objective of the interferometer is to perform measurements at small angular scales providing unprecedented resolution in the millimetre/sub-millimetre range with baselines of up to 16 km, while the ACA measures large scales. The four 12 m antennas in the ACA, referred to as the total-power (TP) antennas, are used for single-dish measurements and thus measure the largest scales. The antennas of ALMA are mobile and can be moved to accommodate different baseline configurations. The configuration of ACA is so far kept constant, with baselines between 9–45 m, but the 12-m array is reconfigured throughout each observing cycle. There are 10 configurations,



Figure 3.2: This snapshot captures a segment of the ALMA facility. In the centre, you can observe the closely grouped Atacama Compact Array, consisting of twelve 7-meter antennas. They are encircled by four total power antennas and several additional antennas belonging to the main array, which stretches over several kilometres beyond what is visible in the photograph. Image Credit: ALMA (ESO/NAOJ/NRAO)

from the most compact configuration C1 with a maximum baseline of about 0.16 km to the most extended configuration C10 with a maximum baseline of about 16.0 km (Cortes et al., 2023). With a minimum baseline of the 12 m array of 15 m, the combination of the 12 m array, the 7 m array and the TP antennas thus offers measurements at all lengths of baselines up to 16 km. The following description of ALMA capabilities is based on the information provided in the ALMA Technical Handbook (Cortes et al., 2023). In general, ALMA is equipped with receivers capable of observing between 0.3-8.5 mm as described in Table 3.1. This range of wavelengths, which is used in Papers I and II, corresponds precisely to the radiation that is formed in the solar chromosphere (see Figure 2.1, Figure 2.2). Consequently, ALMA has become the natural instrument that helps to understand what is happening in this region of the Sun. With a relatively high angular resolution and sensitivity, ALMA provides a very good tool to study the chromosphere of the Sun.

The receiver bands have a combined bandwidth of 8 GHz each and measurements can only be performed for one receiver band at a time. The combination of the 12-m array and ACA, with a total of 62 antennas, amounts to a total number of 1891 baselines (following Equation (3.1)). The locations of the antennas in the different configurations are well considered to create an

3. Instruments and Simulations

ALMA Band	Wavelength coverage (mm)	Frequency (GHz)
1	6–8.6	35 – 50
2	2.6–4.5	67 – 116
3	2.6–3.6	84 – 116
4	1.8–2.4	125 – 163
5	1.4–1.8	163 – 211
6	1.1–1.4	211 – 275
7	0.8–1.1	275 – 373
8	0.6–0.8	385 – 500
9	0.4–0.5	602 – 720
10	0.3–0.4	787 – 950

Table 3.1: The wavelength and frequency coverage of ALMA bands 1 - 10. Bands 3, 5, 6 and 7 (shown in Bold) are offered for solar observations. Band 3 and 6 have been in operation for solar observations since 2015, and Band 7 and 5 are offered more recently in 2019 and 2023 respectively. Credit: [ALMA \(ESO/NAOJ/NRAO\)](#)

even nearly Gaussian-shaped distribution of sampling in the Fourier space (or uv-space). The resulting Point Spread Function (PSF) for the full ALMA array, i.e. the synthesised beam, shows a clear main lobe and only a very weak side-lobe pattern, which allows for very precise measurements.

Each combination of antennas in ALMA makes a point in the uv-plane. Consequently, the Fourier transform of visibilities for a point source corresponds to the radio interferometer’s PSF, referred to as the synthesised beam in radio astronomy (Thompson, Moran, and Swenson, 2017). However, when the source is extended, an additional deconvolution is required to obtain the source structure. In practice, each configuration of ALMA antennas has two relevant quantities associated. The first, called the Maximum Recoverable Scale (θ_{MRS}) is given by the shortest baseline. The second quantity is the angular resolution (θ_{res}) given by the longest baseline. The angular resolution corresponds to the synthesised beam of the interferometric array. In order to define the angular resolution of ALMA, the team conducted simulations and arrived at the following empirical equation

$$\theta_{res} \approx 0.574 \frac{\lambda}{L_{80}}, \quad (3.3)$$

where λ corresponds to the observed wavelength and L_{80} to the 80th percentile projected longest baseline in meters. The maximum recoverable scale can also be calculated using the 5th percentile projected shortest baseline in meters L_5 using the following empirical equation:

$$\theta_{MRS} \approx 0.983 \frac{\lambda}{L_5} \quad (3.4)$$

The decreasing resolution with increasing wavelength is visible in our study in papers I and II.

In radio interferometry, the primary beam is approximated as Gaussian distribution. Hence the sensitivity is maximum in the centre and declines towards the edges. The Field of View (FOV) is initially defined as the Full Width at Half Maximum (FWHM) of the primary beam of a single antenna, which can be calculated using Equation (3.2) and $D = 12$ m. However, the final FOV depends on the selected primary beam cutoff. The FOV measured is directly related to the primary beam response of each antenna (equivalent to its PSF) and its wavelength. Longer wavelengths result in larger FOV according to the relation (Cortes et al., 2023; Wedemeyer et al., 2016):

$$\theta_{FOV} \approx 1.13 \frac{\lambda}{D} \approx 19\lambda(mm) \quad (3.5)$$

For instance, measurements at 1.2 mm (Band 6) result in $\theta_{FOV} \approx 23$ arcsec, while measurements at 3 mm (Band 3) lead to $\theta_{FOV} \approx 57$ arcsec. A Gaussian distribution can be used to approximate the primary beam response, so its sensitivity is maximal in the middle and decreases toward the edges. Hence, it is logical to confine observations to regions with reasonably high sensitivity. A typical approach is to constrain the primary beam response to approximately 0.5 or 0.3 of the full width at half maximum (FWHM).

3.2.1.1 Solar observations with ALMA

ALMA commenced its solar observations during Cycle 4 (years 2016-2017). During this period, a collaborative effort among international solar physicists resulted in a comprehensive document (Wedemeyer et al., 2016) outlining ALMA's prospective capabilities for studying phenomena in both the quiet Sun and active regions. The prospect of directly observing brightness temperature, a physical parameter closely aligned with local gas temperature, held the promise of providing invaluable insights into comprehending the mechanisms driving chromospheric-coronal heating. Hence, there have been several reports on solar ALMA data with various scientific goals, reporting observations of various phenomena, including sunspots (Jafarzadeh et al., 2019; Rodger et al., 2019), chromospheric plages (Chintzoglou et al., 2021a), type II spicules (Chintzoglou et al., 2021b), on-limb spicules (Shimojo et al., 2020), oscillations (Guevara Gómez et al., 2021; Jafarzadeh et al., 2019; Patsourakos et al., 2020) and transient brightening events (da Silva Santos et al., 2020; Eklund et al., 2020; Molnar et al., 2019; Nindos et al., 2021; Nindos, 2020; Shimojo et al., 2017).

Solar observations with ALMA need more caution, as the Sun is an *extended source*, i.e. cannot be approximated to a point source. Hence there are certain restrictions in place. The limitations and constraints are consistently and comprehensively detailed in the ALMA observation proposer's guide (Cortes et al., 2023). The altitude of the target in the sky is important because of the resulting shape of the PSF. The closer the target is to the horizon, the resulting PSF is increasingly eccentric, which introduces quite severe uncertainties, particularly in the analysis of small-scale structures.

3. Instruments and Simulations

As a consequence of the heavily dynamic nature of the chromosphere with small-scale phenomena evolving at short time scales, a high cadence is necessary to be able to resolve them properly. The interferometric measurements probe relative differences in intensity or brightness temperature (following the Rayleigh-Jeans approximation; Equation (2.6)). Because of the high cadence² of the time series for solar ALMA data, challenges are encountered that typically do not arise for radio observations of other more static targets. Hence, the Solar ALMA Pipeline (SoAP), a Python-based code, is developed which calls necessary tools in CASA (Common Astronomy Software Applications package) for performing post-processing of the observational data, after the cleaning (an iterative technique to deconvolve the beam from the image) and imaging of the interferometric data, by employing a self-calibration algorithm on pre-calibrated measurement set to construct high-cadence time-series ready for scientific analysis. SoAP has been already used to produce 26 datasets of solar observation with ALMA which are now collected in the so-called Solar ALMA Science Archive (SALSA) available online at <http://sdc.uio.no/salsa/> (Henriques et al., 2022). One of the datasets from this repository is used in this thesis, in Paper I.

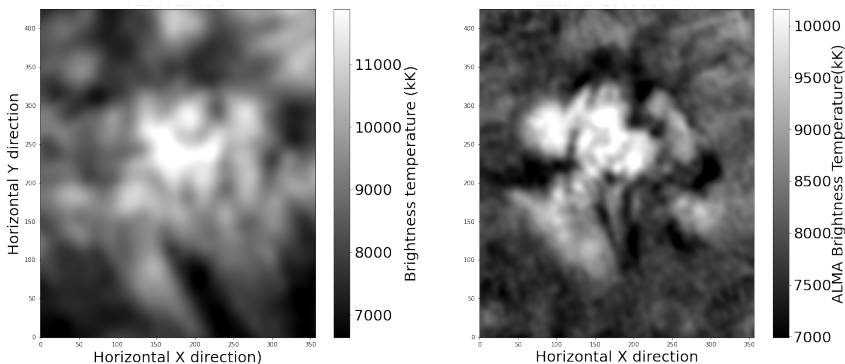


Figure 3.3: The observations taken on 23rd April 2017 with ALMA Bands 3 and 6. Credit for the dataset: ALMA ADS/JAO.ALMA2016.1.01532.S

One of the well-studied interferometric datasets from April 2017 from ALMA Bands 3 and 6 is shown in Figure 3.3. The data from other diagnostics are spatially resampled in order to match the resolution of ALMA. In Figures 3.4 and 3.5, the comparison between observed ALMA interferometric data and other diagnostics is illustrated. The Pearson correlation coefficients are calculated based on the pixel-to-pixel comparison for the whole dataset and two subsets based on the temperature, the enhanced network (EN) dataset is selected to be the central region above 11 kK for Band 3 and 9.5 kK for Band 6, whereas the quiet sun (QS) dataset is selected to be near to the central region below 7 kK for Band 3 and 7.6 kK for Band 6.

²Frequency of the observations. For example, for ALMA Band 3 interferometric solar data in cycle 4 there is one observation every 2 seconds.

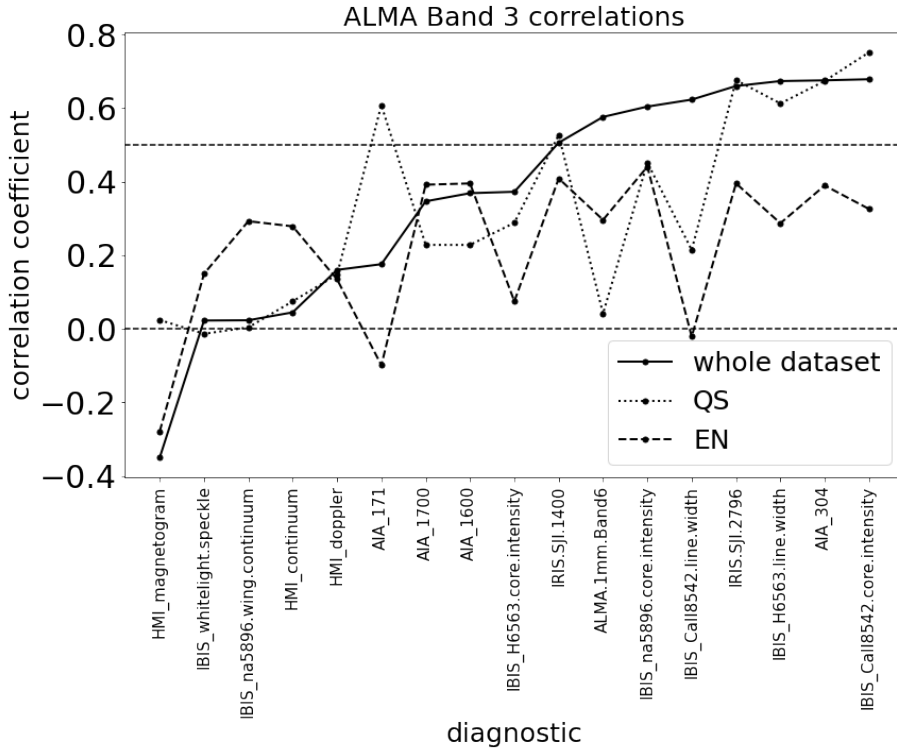


Figure 3.4: The co-observations taken on 23rd April 2017 from IRIS slit jaw imager, IBIS and SDO AIA channels 1600, 1700 and 304, and HMI magnetogram are compared with the co-aligned observations from ALMA Band 3. Credit for the co-aligned dataset: Kevin Reardon, Johnathan Strauffer

The correlation coefficients of ALMA Band 3 and 6 with the chromospheric diagnostics, like $H\alpha$ linewidth, Ca II 8542 line core and linewidth, as illustrated in Figure 2.1 are the highest. Whereas, for more photospheric diagnostics like HMI magnetogram, AIA channels 1600, 1700, 171, etc., the correlations are close to zero. This experiment was done partly as a sanity check, as the work done in papers I and II is based on synthetic data. The observed data shows good agreement with the results in the paper as the correlations with $H\alpha$ linewidth, SDO AIA channel 304 and Ca II 8542 are highest for the ALMA data. The band 6 radiation is formed below band 3 (Alissandrakis, 2023; Alissandrakis, Bastian, and Brajša, 2022). As seen in papers I and II, the indices formed from $H\alpha$ and Ca II are representatives of similar regions in height as the lower mm wavelengths. Because of the difference in the FOV as discussed before and summarised in Equation (3.5), the correlation coefficients are inherently lower for Band 6 in comparison to Band 3, owing to a smaller FOV in the observational box. The slight differences in these correlation coefficients and the

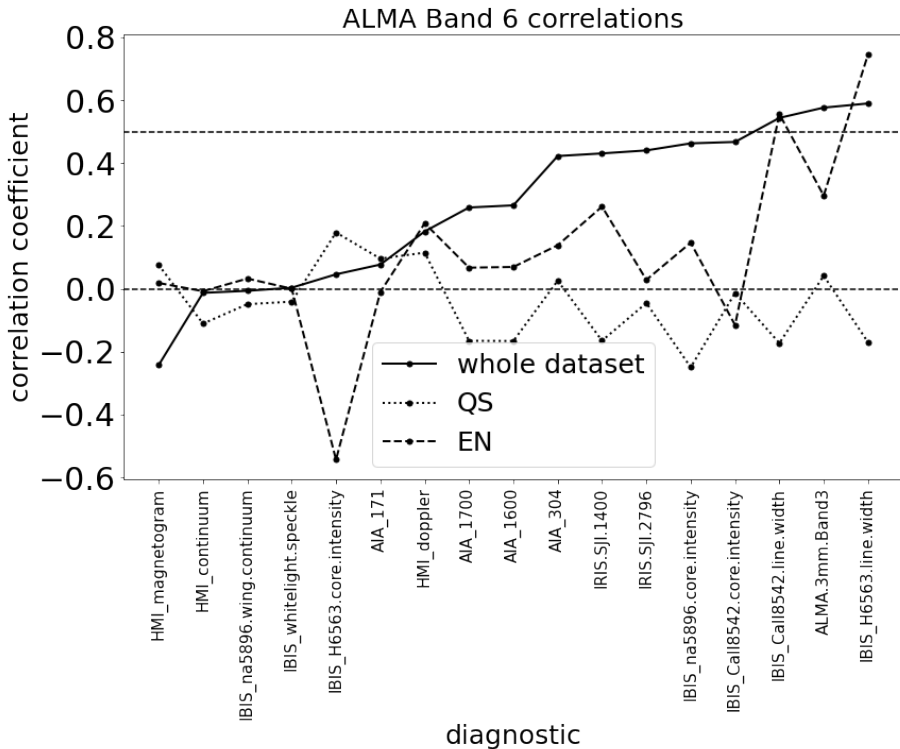


Figure 3.5: Same as Figure 3.4, for ALMA Band 6. Credit for the co-aligned dataset: Kevin Reardon, Johnathan Strauffer

results presented in paper I can be attributed to the difference in the activity levels, the difference in cadence and resolution in the observational data used here and the synthetic data used in the paper. Also, for Ca II 8542 linewidth, the correlation is higher for Band 6, which is in agreement with our findings in the paper II.

3.2.1.2 Total Power Observations

In addition to the relative interferometric intensity measurements to probe the absolute calibration, the total-power antennas are used to measure the average temperature of the Sun. Complimentary to the interferometric data which provides the relative temperature for a smaller FOV as described in the previous section, the full disk (FD) data is collected from a single dish (SD) observation for the absolute value of the average temperature of the Sun. TP maps give the temperature profile for the full disk at a lower resolution. Relative power fluctuations are already given by interferometric data. Thus now we have full disk observations with lower resolution and observations of the region of interest with higher resolution, both in terms of absolute brightness temperatures.

The measurements are performed by a repetitive cyclic motion over the entire solar disc as shown in [Figure 3.6](#), during the time of the interferometric observations. It usually takes around 5 minutes to scan the whole disk to the Band 3 beam (because the beam has a bigger diameter), and around 10 (9.67) minutes to the Band 6 beam (owing to the beam's comparatively smaller diameter). These measurements are then used as the offset for the interferometric measurements to absolute temperatures. A sample of ALMA TP (FD) observation for Band 3, 6 and 7 from 2019 is shown in the top row of [Figure 3.7](#) in comparison with the optical observations from SDO AIA channels. The small-scale features are captured by ALMA Bands, in height ranges similar to SDO channel 304. This aspect is further addressed in [Paper III](#).

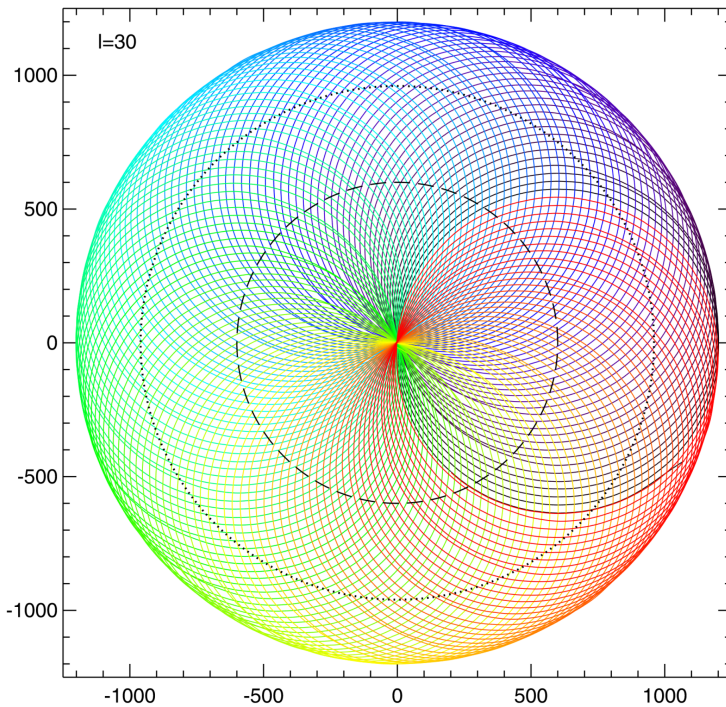


Figure 3.6: The figure displays a double-circle pattern representing a $2400''$ diameter field of view with a "map spacing" of $30''$. Inside this, a dashed-line circle at a radius of $600''$ represents the "major circle" track of the individual minor circles' centres. Additionally, a dotted line marks the (average) solar limb at a radius of $960''$. The telescope track is colour-coded with a rainbow colour table, indicating the pointing location's progress over time. Mapping commenced and concluded approximately at the "3 o'clock" location in the figure. Taken from White et al., 2017

The single dish data is calibrated using correction factors as described in White et al., 2017. The data is further rescaled to quiet sun values at the disk

3. Instruments and Simulations

centre of 7300 K for Band 3 and 5900 K for Band 6. These values are known to have statistical uncertainties of about 100 K, but systematic uncertainties in the temperature scale may be significantly larger (White et al., 2017). Their analysis of sample images showed that the temperature on the disk can vary over about a 2000 K range at the 25'' resolution of the Band 6 data. The interferometric images should show an even wider range of variation as a result. The rescaling temperatures are based on early science verification data before 2017 when the Sun was more active than most of the datasets. But the solar activity fluctuates with time and there was a minimum around 2019-2020 (this is further discussed in Chapter 4). This rescaling could introduce synthetic scaling errors in the TP datasets, as it is based on the pilot dataset being limited in time. In Paper III we used non-rescaled data and tried to address this issue.

3.3 Synthetic Observations

The observations are synthesised by using a model atmosphere as input for a radiative transfer code. Depending on the requirements, the model atmospheres and radiative transfer codes are chosen. Further, the synthesised data is curated according to the details of the observational data for a fair comparison. As described in the following subsections, these steps are used for the synthesis of data for my thesis.

3.3.1 Numerical Simulations

In this thesis, papers I and II utilised a simulation of an enhanced network region generated with the 3D rMHD Bifrost code.

3.3.1.1 Bifrost

Bifrost employs MHD partial differential equations to create a model of the solar atmosphere, a box-in-a-star, capturing all physical parameters of the plasma at every 3D snapshot. Bifrost produces the solar atmosphere in high resolution (Gudiksen et al., 2011). The name of the model used in this project is publicly available³ en024048-hion, ‘en’ standing for the enhanced network which is a magnetic field configuration in the solar chromosphere. The computational box is 24 Mm \times 24 Mm horizontally, with periodic boundary conditions and it extends 2.4 Mm below the visible surface and 14.4 Mm above. It encompasses the upper part of the convection zone, the photosphere, chromosphere, transition region and corona (Carlsson et al., 2016). Notably, this simulation incorporates non-LTE radiative transfer and a time-dependent equation of state to handle non-equilibrium hydrogen ionisation (Leenaarts, Carlsson, and Rouppe van der Voort, 2015). The computational box is 504 \times 504 \times 496 grid points giving 48 km resolution horizontally corresponding to an angular size of approximately 0.066 arcsec. It has a variable grid separation in the vertical direction varying

³<http://sdc.uio.no/search/simulations>

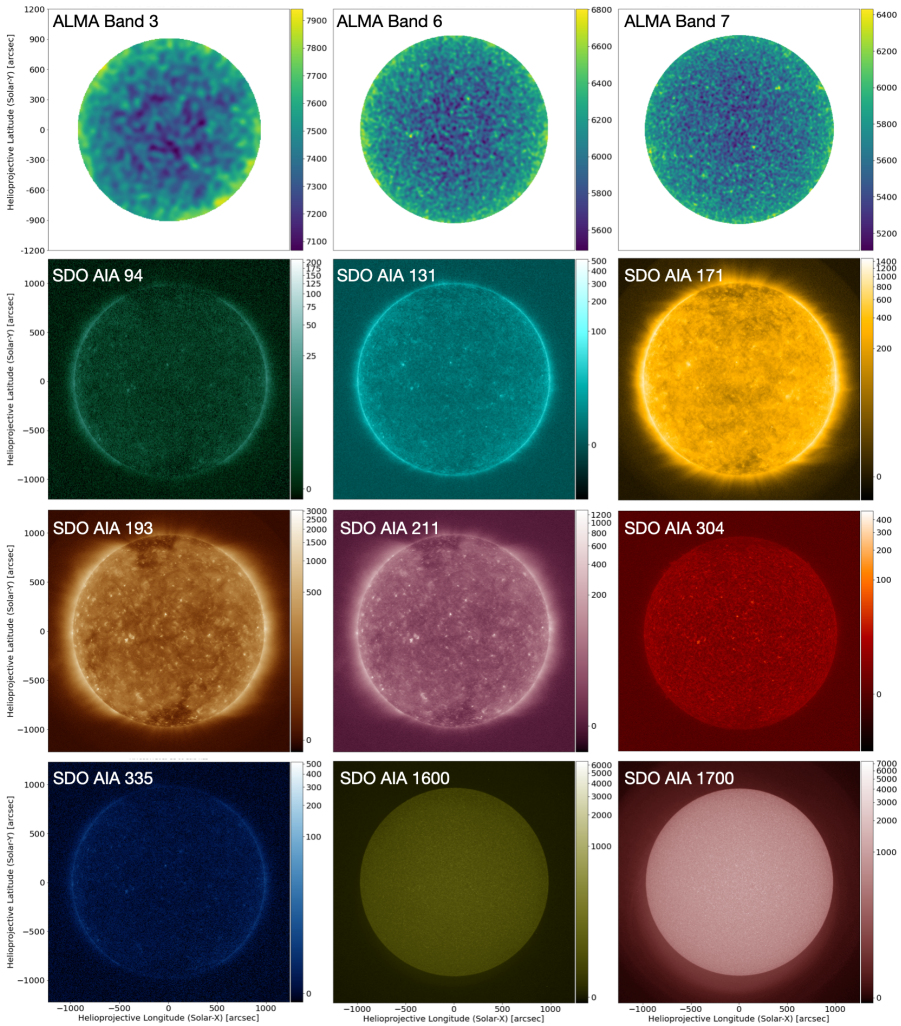


Figure 3.7: Full disk (FD) non-rescaled images of the Sun in different wavelengths from the less active period in 2019, the top row shows FD maps from ALMA bands 3 (from April), 6 (from November) and 7 (from December), and the rest of FD maps are from the different channels of AIA onboard SDO (co-temporal to Band 6 data). Different wavelengths probe different layers, 304 Ångstroms being the closest to ALMA maps. The limb effects: brightening in ALMA FD maps, and limb darkening in SDO AIA channels 1600, and 1700 is clearly visible.

3. Instruments and Simulations

from 19 km in the photosphere and chromosphere up to 5 Mm height and then increasing to 100 km at the top boundary, with approximately 20 km resolution at chromospheric heights. Both the top and bottom boundaries are transparent. At the bottom boundary, the magnetic field is passively advected with no extra field fed into the computational domain (Carlsson et al., 2016). For a detailed description of the Bifrost code and the enhanced network simulation, please refer to Carlsson et al., 2016; Gudiksen et al., 2011. For a cross-section of temperature and absolute magnetic field in the chromosphere, please refer to Figure 1 in paper I.

3.3.1.2 1D Semi-empirical models

The 1D semi-empirical reference models representative of quiet sun conditions VAL (Vernazza, Avrett, and Loeser, 1981) (see Figure 2.1 for VAL C model), FAL (Fontenla, Avrett, and Loeser, 1993) and the sunspot models by Maltby et al., 1986 are used to compare with the 3D results. Corresponding line profiles and mm continuum intensities for these 1D semi-empirical atmosphere models are calculated with the radiative code RH 1.5D (Pereira and Uitenbroek, 2015; Uitenbroek, 2001).

These models capture the temperature stratification of the Sun at different activity levels but being simplified miss the variation and nuances that the dynamic sun has. The advantage is the simplicity, and as these are semi-empirical, meaning based on a set of observations, these are still used for sanity checks. The limitations of these are discussed in papers I and II.

3.3.2 Radiative Transfer

3.3.2.1 Theoretical background of Radiative Transfer

The H α line is one of the very well-studied chromospheric lines as it is deep and is not surrounded by any other strong lines⁴. Spectral lines can be described in atomic physics in simple-to-understand illustrations, e.g. for H α line as shown in Fig. 3.8. In the Paper I we have used H α data in comparison to the sub-mm data.

The term diagram in Fig. 3.9 shows us the five-level plus continuum model atom of the Ca II ion. The reason behind looking at the Ca II H and K lines is that those are distinctively dark lines whose cores are formed in the chromosphere. They form due to the most probable transition, i.e. the energy absorption between 4s, the highest populated energy level, and 4p, the immediate higher shell available (Uitenbroek, 1990b; Wedemeyer-Böhm and Carlsson, 2011). The infrared triplet of Ca II on the other hand is between 3d and 4p. It consists of three strong lines at 849.8018, 854.2089, and 866.214 nm, whose cores are formed in the chromosphere similar to Ca II H & K (Björgeren et al., 2018; Jorgensen, Carlsson, and Johnson, 1992). They have smaller energy gaps. The H and K lines are formed much higher in the less dense upper chromosphere where 3D and

⁴wavelength-wise

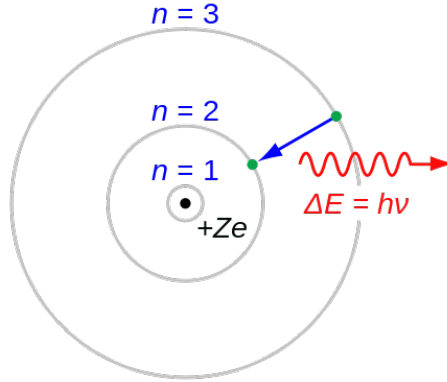


Figure 3.8: The deep-red visible spectral line of the hydrogen atom has a wavelength of 656.28 nm in air and 656.46 nm in a vacuum. This line belongs to the Balmer series and represents the first spectral line emitted when an electron transitions from the third- to the second-lowest energy level of a hydrogen atom. Image Credit: [commons.wikimedia](https://commons.wikimedia.org/)

partially-coherent scattering i.e. partial redistribution (PRD) effects play a more essential role in line formation than in the infrared triplet of Ca II (Uitenbroek, 1990a).

The core and the wings of Ca II H & K are formed at different heights. The core is formed at chromospheric heights and the wings are formed way deeper inside the photosphere following local thermodynamic equilibrium (LTE). The Ca II H & K lines have high intensity in the observations. The temperature stratification can be traced by this line. The signatures of chromospheric temperature rise can be seen. The K line is one of the deepest and widest lines for F, G and K-type stars. Its core shows the characteristic double reversal profile, i.e. an emission with central self-absorption (Frasca et al., 2010; Pace, Pasquini, and Ortolani, 2003). The typical features of the lines are shown in Figure 3.10. The outer wings are $K_1(H_1)$ features and V and R represent the blue or red side of the wing. Similarly, the $K_2(H_2)$ feature is the intermediate emission feature with blue and red sides for the wings, and the line core ($K_3(H_3)$) is the absorption feature of the line. The Doppler shift of the line core, i.e. the wavelength position of K_3 , is a very accurate probe for velocities in the upper chromosphere (Sowmya et al., 2021).

In Table 1 from Paper II, the formation heights of the line features from the solar surface (photosphere) are listed. In Bjørngen et al., 2018, the formation height range is constrained using SST/CHROMIS observations using different models for Ca II absorption-emission peaks generated from FAL atmospheres. The average formation heights for the Ca II K line are provided from the photosphere and the Ca II H formation height range is provided in reference to the K line. It is important to note that the difference in formation heights has an impact on the generated spectra from a tilted atmosphere.

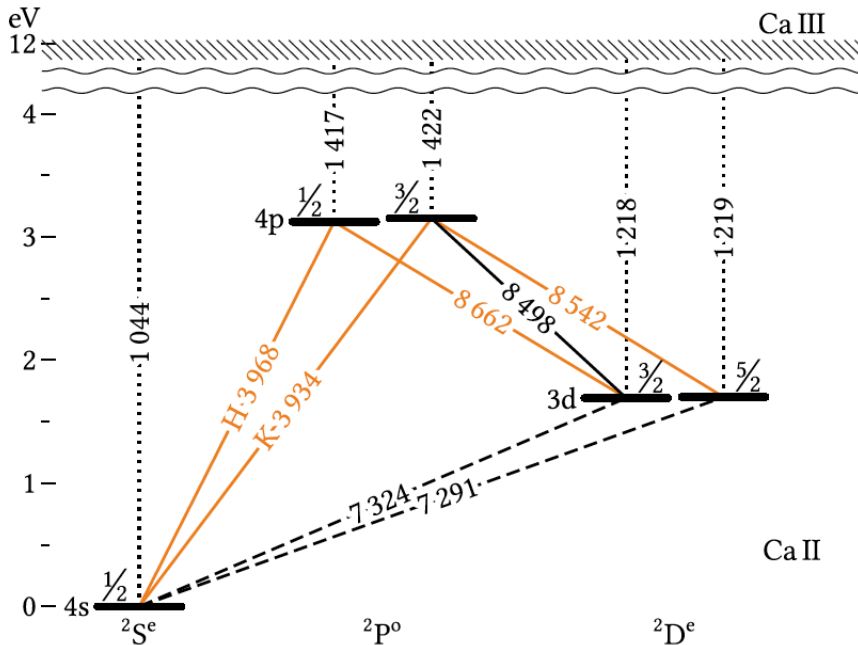


Figure 3.9: For all transitions, the line centre or threshold wavelengths are given in Ångströms. The atomic levels are shown with the valence electron configuration nl on the left, the total angular momentum J on the top, and the term configuration $2S+1LP$ at the bottom row. Solid line for bound-bound transition, dashed line for forbidden transition, orange line for PRD transitions and dotted line for bound-free transitions connecting levels to the Ca II continuum. Taken from (Björgeren et al., 2018).

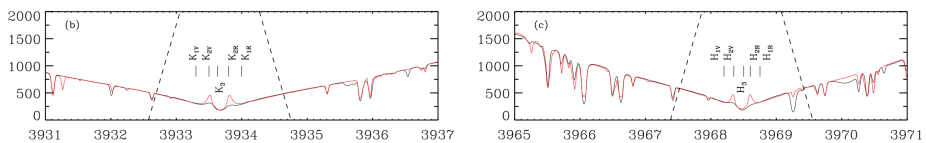


Figure 3.10: Typical features of Ca II K (b) and H (c) quiet sun lines for observed Fourier Transform Spectrometer (FTS) spectra (black) and the spectra synthesised with the RH code (red). The y-axis is the intensity in SI units and the x-axis is the wavelength in Ångströms. The dashed black lines represent the triangular filters for the s index described further in Chapter 4. Taken from Sowmya et al., 2021.

Different radiative transfer (RT) codes were used based on the requirement of the computational treatment. In the case of the Ca II line synthesis, RH1.5D was used with a 5-level atom, as the computational power can be saved using 1.5D instead of 3D. Whereas for the hydrogen Balmer α line, the 3D treatment was necessary, so the Multi3D code was used. In the case of the synthesis of mm wavelengths, the Advanced Radiative Transfer (ART) code was used. It uses the Bifrost models and generates the mm intensities. A quick description of the used RT codes is given in subsequent subsections.

3.3.2.2 Multi3D

Multi3D employs the accelerated lambda iteration method developed by Rybicki and Hummer, 1992 with the extension to treat effects of partial frequency redistribution using the angle averaged approximation by Uitenbroek, 2001. We used the five-level plus continuum hydrogen model atom. Microturbulence⁵ is not introduced as it is shown in Leenaarts, Carlsson, and Rouppe van der Voort, 2012 that the synthesised spectra are similar to observational spectra even without using microturbulence. Further details of synthesising the H α spectra in 3D using Multi3D can be found in Leenaarts, Carlsson, and Rouppe van der Voort, 2012

3.3.2.3 RH1.5D

The publicly available RH1.5D⁶ code solves the equations of statistical equilibrium and radiative transfer self consistently for multilevel atoms and molecules (Pereira and Uitenbroek, 2015). This RH1.5D code is an extensively parallelized adaptation of the previous RH radiative transfer code, originally developed by Uitenbroek, 2001. This updated version is capable of conducting multi-atom, multi-level, non-LTE radiation transport, accommodating complete and partial frequency redistribution (CRD and PRD) of photons.

The Ca II H and K wings form in the photosphere under LTE, whereas the cores form in the chromosphere, where the densities are so low that departures from LTE become significant. If the LTE approximation is used for synthesising line cores, it gives rise to unrealistic emission profiles, because the temperature increases in the chromosphere (Sowmya et al., 2021), hence while synthesising Ca II spectra, non-LTE conditions are employed. As discussed earlier, PRD effects are important for the formation of these lines (Uitenbroek, 1991). Hence, the non-LTE PRD capability of RH is used to synthesise spectra in the case of Ca II H & K lines (Bergemann et al., 2019; Bjørgen and Leenaarts, 2017).

3.3.2.4 ART

The intensity of the continuum radiation at mm wavelengths for the 3D input model, Bifrost (described in Section 3.3.1.1), is calculated with the

⁵Turbulence at small spatial scales.

⁶<https://github.com/ITA-Solar/rh>

3. Instruments and Simulations

publicly available Advanced Radiative Transfer (ART)⁷ code by Cruz Rodríguez, Szydlarski, and Wedemeyer, 2021 in LTE conditions. In addition, ART considers non-equilibrium electron densities provided by the Bifrost simulations, since these densities contribute to continuum radiation at wavelengths at sub-mm and mm. ART produces a continuum brightness temperature map at the specified frequency as the final product. In total, maps for 34 mm wavelengths are computed from the Bifrost en024048 model, covering the range described in Table 3.1 that in principle can be observed with ALMA. This includes both, currently available receiver bands and bands that might be offered for solar observations in the future.

3.3.3 PSF for data degradation

Papers I and II presented in this thesis extensively employed simulated data to complement observational studies, allowing for a more comprehensive interpretation of the results. However, it is crucial to exercise caution when using simulated data. Simulated data is with customised spatial, and spectral resolution based on the input parameters. When comparing with the observational data, it would be unfair and potentially misleading to use the simulated data directly. To address this concern, the approach taken in this investigation was to replicate the instrument's (ALMA) effects in the simulations, including temporal cadence and the point spread function (PSF) or the beam. The beam used for this study is idealised to be a circular Gaussian based on the mm wavelength. The beam's width is set to $2''$ at a wavelength of $\lambda = 3.0$ mm, as a first approximation from the ALMA observations, and then linearly scaled as a function of the observing wavelength.

In Paper III, the data used from SDO AIA is also treated with the PSF from corresponding observational ALMA data for a fair comparison. By doing so, data similar to the actual observations, or observations possible in the future, were obtained, facilitating a thorough review of the original resolution. Consequently, this methodology ensured that the identified elements in the observations were grounded in reality and not merely artefacts or errors arising from the instruments or computational processes.

This approach makes the synthetic observations with the same angular resolution as the ALMA data. By using idealised PSF on the synthetic data we are ignoring the limited uv coverage of an actual interferometric observation (Wedemeyer et al., 2022). The uv sampling depends upon the antenna setup for each observation, and it is not taken into account in our study. Also, the effects due to Earth's atmosphere are not taken into account in this approach. The water vapours absorb and scatter the IR wavelengths which is not accounted for in the synthetic observations (He, Dent, and Wilson, 2022).

⁷<https://zenodo.org/record/4604825>

Chapter 4

Stellar Activity

Scientists define habitable zones as the range of orbits around a star where the planets can hold liquid water depending on the stellar irradiance, surface temperature and atmospheric pressure. It is this very special Earth-Sun relationship that has led to the possibility of sustainable life. It is important to understand the stellar activity to predict the possibility of life on the planets revolving around that star. The stellar activity would influence the temperature, radiation, elements and the physical constitution of the planet, the possibility of an atmosphere and many more factors. Understanding the relation between stellar activity and these factors determining the possibility of life would be the first step in looking for alien life (Gallet et al., 2017; Tayar et al., 2022). As Carl Sagan said in *Contact*, “*The universe is a pretty big place. If it’s just us, seems like an awful waste of space.*”

Astronomers in the 1800s discovered the cyclic appearance of sunspots over an approximately 11-year period (Schwabe, 1844). As new solar features were found, it was observed that they also varied in sync with the frequency of sunspots, because all these features are related to the magnetic activity (Hale, 1908; Leighton, 1969; Saar, 2011). The sunspot number is now commonly used as a measure of solar activity, which has been linked to satellite failures, electrical power outages and disruptions in the communication and navigation systems. The impact of solar activity on Earth and technology has led to a growing need for better understanding and predicting solar activity.

A solar cycle, also known as a solar magnetic activity cycle or sunspot cycle, follows about an 11-year periodic pattern of the Sun’s activity. During this cycle, the number of sunspots on the Sun’s surface varies as shown in [Figure 4.1](#) for a span of 400 years. The anomalous period of low activity is called the Maunder minimum (Eddy, 1976). The formation of the sunspots is due to the differential rotation of the Sun, i.e. the equator takes 25 days to complete one rotation, but the poles rotate slower, taking 35 days as discovered by Carrington, 1859. The global magnetic field configuration of stars changes in a cyclic manner between toroidal and poloidal due to the dynamo processes, convection and rotation. This is believed to be one of the reasons for the fluctuation in stellar activity and for energy transport (Babcock, 1961; Babcock and Babcock, 1955; Baliunas et al., 1995; Phillips, 1992). There are synchronised fluctuations in solar radiation levels, sunspot numbers, solar flares, and coronal mass ejections (CMEs). These are active events as described in [Chapter 1](#). The activity cycle involves periods of minimum activity, followed by periods of maximum activity, and then returning to periods of minimum activity (Lockwood et al., 2007). In other words, as the activity increases, the number and intensity of flares, prominences, CMEs and solar wind also increase (Hazra et al., 2021; McComas

4. Stellar Activity

et al., 2003). This is visible when we compare data from 2015, when the activity was high, (Figure 4.2) with the data from 2019, when the activity was lowest (Figure 3.7). The activity is on the rise again, in 2022, as seen in Figure 4.3.

Over the past 150 years, sunspot activity has shown varying amplitudes from one cycle to the next as seen in Figure 4.4. The butterfly diagram shows the appearance of sunspots at higher latitudes at solar maximum and near the equator, at solar minimum, as discovered by Carrington, 1858. The average cycle typically reaches a peak sunspot number of around 150. However, there have been times, such as during the Maunder Minimum between 1645 and 1715, when solar activity became so weak that it seemed to disappear for several decades (Eddy, 1976). Another way of looking at this phenomenon is that the sunspot cycle/ solar cycle is the inversion of magnetic polarity in the average period of 11 years which was discovered by Hale and Nicholson, 1925; Hale et al., 1919. The magnetic dipole in the core of the Sun flips every 11 years and this is also observed in several other stars. Magnetic polarity inversion has been an active field of research since the discovery by Hale et al., 1919. A further account is given in the living reviews by Hathaway, 2015; Usoskin, 2023.

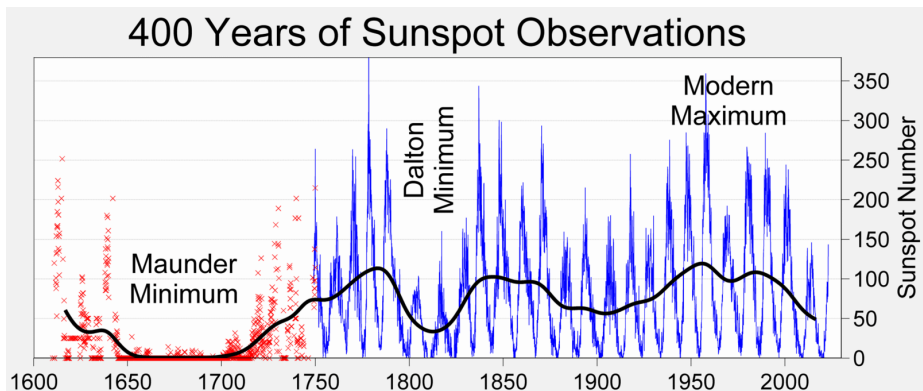


Figure 4.1: The variation in the number of sunspots over 400 years. The number of sunspots on the solar disk varies over a period of approximately 11 years. Image source: [commons.wikimedia](https://commons.wikimedia.org/wiki/File:Sunspot_number_1600-2000.png)

4.1 Activity indicators

The Sun being the closest star, spatiotemporally resolved solar spectra can be observed. On the other hand, observed stellar spectra are not as spatially resolved. The number of spots as an indicator of the activity cannot be used for other stars as the stars are far away and the observations of the stars are with significantly lower resolution, usually just the spectra. Counting sunspots on the stellar disk is not possible in that case¹. But it is evident that the stars have

¹Its possible to infer a large spot on the stellar disk by using a method called Zeeman Doppler imaging (eg.Strassmeier, Carroll, and Ilyin, 2019), but it requires the spot to be

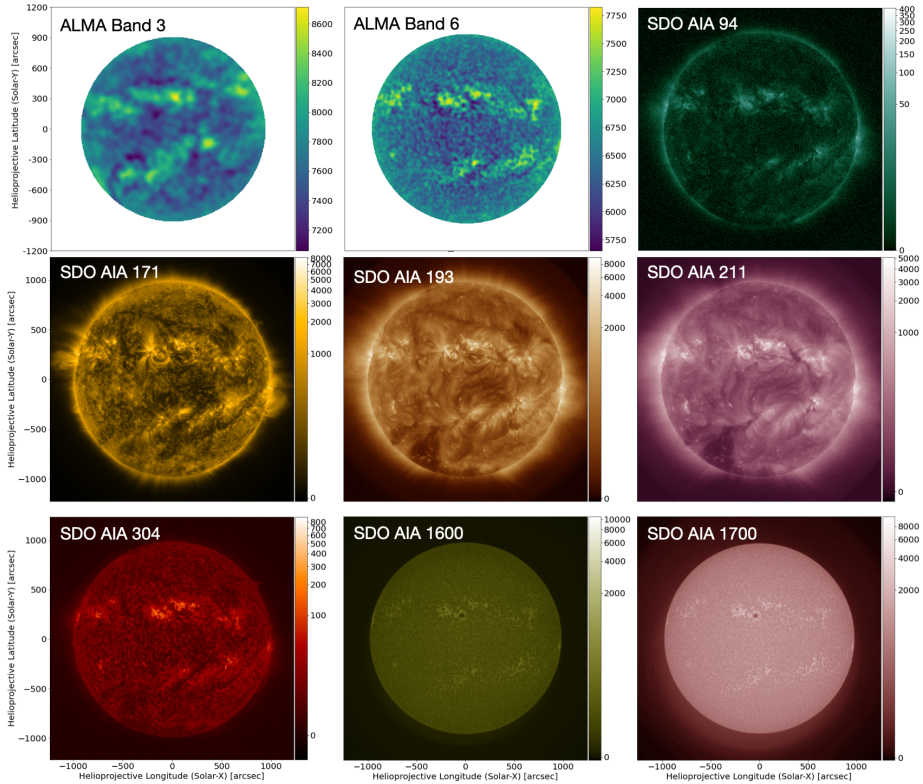


Figure 4.2: Full disk (FD) non-rescaled images of the Sun in different wavelengths from the more active period in December 2015, the top row shows FD maps from ALMA bands 3 (from 16th), 6 (from 18th) from the science verification data, and the rest of FD maps are from the different channels of AIA onboard SDO (co-temporal to Band 6 data). Different wavelengths probe different layers, 304 Ångstroms being the closest to ALMA maps, similar to Figure 3.7. Band 6 data shows sunspots aligned to 1600 and 1700 channels and plage regions as seen in 304 channel. Channels 131 and 335 are omitted due to bad datasets, Band 7 data was not commissioned in 2015.

4. Stellar Activity

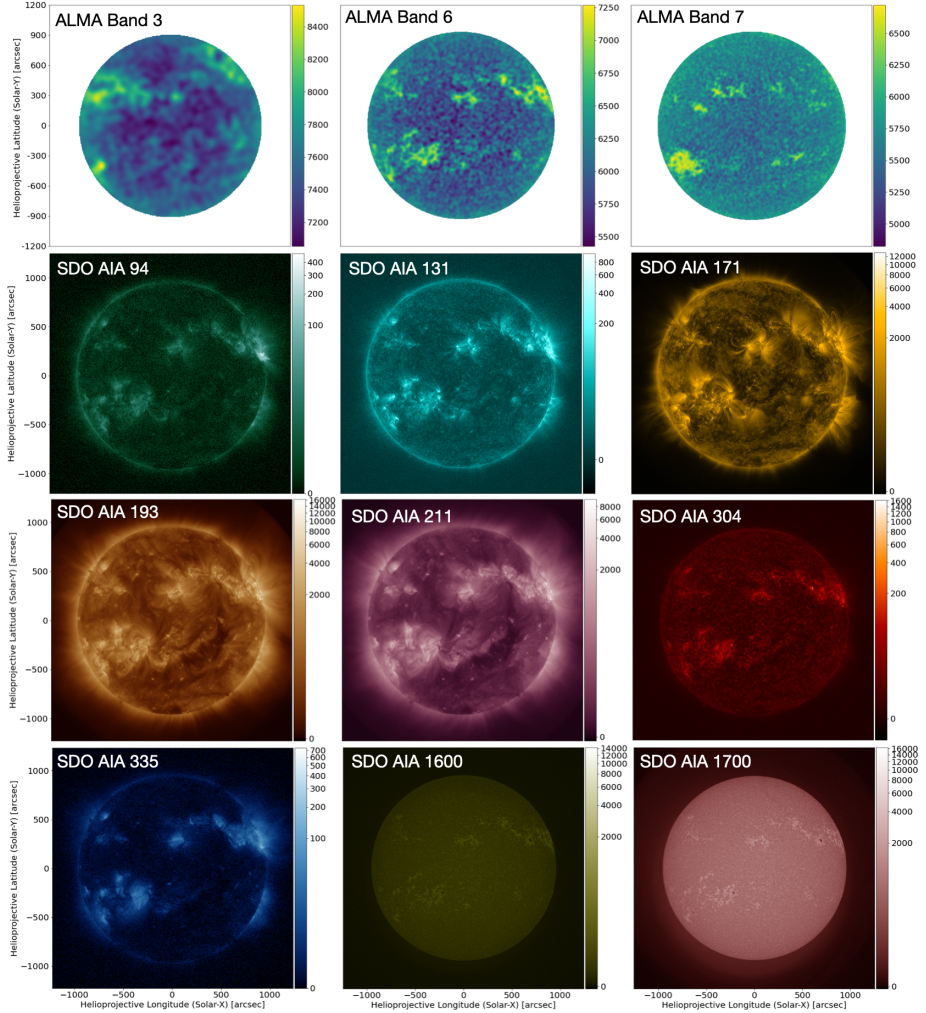


Figure 4.3: Full disk (FD) non-rescaled images of the Sun in different wavelengths from another more active period in 2022, the top row shows FD maps from ALMA bands 3 (from October), 6 and 7 (from April), and the rest of FD maps are from the different channels of AIA onboard SDO (co-temporal to Band 6 data). Plage regions and bright features are seen clearly. The band 7 data had some extreme temperatures owing to severe antenna response.

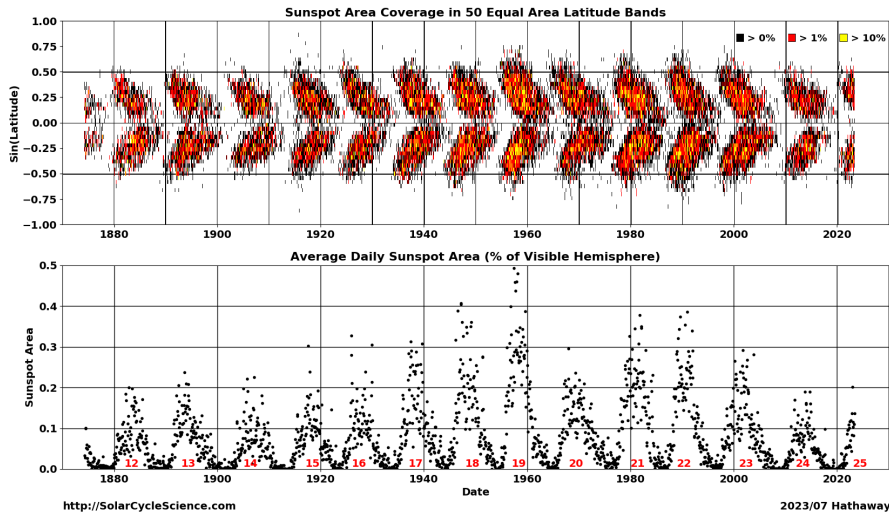


Figure 4.4: Sunspot Area Butterfly Diagram. This shows the distribution of sunspot area as a function of latitude since 1874. As of 2023, we are in cycle 25. Image Credit: SolarCycleScience.com

cyclic fluctuations in the activity and changes in the activity periods (Baliunas et al., 1995; Boro Saikia et al., 2018; Brandenburg, Mathur, and Metcalfe, 2017; Saar and Brandenburg, 1999). Hence scientists had to come up with some other ways that stellar activity can be gauged, which is using proxies of coronal, chromospheric and photospheric radiation (Salabert et al., 2017). These need to be normalised based on the observatories and filters used to observe the stellar spectra. These proxies are called stellar activity indicators.

The oldest of those indicators is the s index, which is based on Ca II lines described in Section 3.3. Along with the s index, there are a number of indicators discussed in the following section. There are coronal activity indicators which are from the x-ray regime, but that is not the focus of the thesis. The zoo of activity indicators has emerged in past decades of stellar physics research and we will look into the types in the next section and specifically the indicators used in Paper II and Paper III.

The stellar activity and the rotation decrease with age. The activity indicators are dependent on the rotation rate (dependent on age), spectral type (dependent on the mass) of the star and hence the size of the convection zone, or the convection turnover time (Noyes et al., 1984). Hence stellar physicists study the relation between these quantities (Skumanich, 1972). The activity indicators along with the metallicity, age and rotation rate can give us more information about the stellar atmospheric structure and possibly temperature stratification of the star (Amard and Matt, 2020; Karoff et al., 2018; See et al., 2021). The

substantially large.

temperature stratification of the Sun is a very important topic of study because of the so-called chromospheric heating problem as described in [Chapter 1](#). In short, the temperatures observed in the corona are severely higher than a close-to-ideal black body. The temperature of the solar surface is 5770 K, which goes down to around 3500 K in the lower chromosphere and in the transition region, it starts to go up very sharply reaching around $1\text{-}2 \times 10^6$ K. The density is very low in the coronal region in comparison to the density near the surface, hence it becomes even more puzzling. There are mechanisms proposed for this heating and those explain the phenomenon up to a certain extent, but not completely. Hence, learning about the atmospheres of other stars can give us new insight into this problem.

Using the Sun-as-a-star approach, for calculating activity indicators for the Sun, the resolved spectra are collapsed; that is, they are averaged, integrated, or convolved with a filter (Strassmeier et al., 1989). As much more spatiotemporally resolved data is available for solar spectra, the indices generated for an activity indicator can be used again to retrieve information about the atmosphere. The index thus generated, could further be used to compare the stellar spectra of the Sun-like stars with the solar spectra, which can give insights into the stellar atmospheres and their stratification (White, 2004).

4.1.1 Ratios

The ratios are activity indicators defined as the flux of a spectral feature that necessarily needs to be normalised with the flux of the nearby continuum. The S index is a Ca II activity indicator defined for the Mt. Wilson observatory by Vaughan, Preston, and Wilson, 1978 as described in [Equation \(4.1\)](#). The definition for the filters is based on the sensitivities of the filters back then. The filter for the H spectral line is twice as sensitive as the filter for the K spectral line. The lines and the position of the triangular filters are graphically shown in [Figure 3.10](#). The integration of the fluxes over these filters thus defines the s-index as follows:

$$s \text{ index} = \frac{F_H + F_K}{F_V + F_R}, \quad (4.1)$$

where F_H and F_K are the integrated fluxes over the triangular filter over the lines H and K, and F_R and F_V are the integrated fluxes over the rectangular filter over the continuum bands on the red (R) and blue (V) sides of the lines, respectively.

Similarly, the Ca infrared triplet index is defined based on the definition of the S-index as follows:

$$\text{Ca}_{\text{IRT}} \text{ index} = \frac{F_{8498} + F_{8542} + F_{8662}}{F_{V_{\text{IRT}}} + F_{R_{\text{IRT}}}}, \quad (4.2)$$

where F_{8498} , F_{8542} and F_{8662} are the fluxes measured in 2 \AA rectangular bandpasses centred on the respective Ca II IRT lines, while $F_{V_{\text{IRT}}}$ and $F_{R_{\text{IRT}}}$ are the fluxes in 5 \AA rectangular bandpasses centred on two continuum points, 8475.8 \AA and 8704.9 \AA , either side of the IRT lines (Marsden et al., 2014).

The index for H α is defined as

$$\text{H}\alpha \text{ index} = \frac{F_{H\alpha}}{F_{V_H} + F_{R_H}}, \quad (4.3)$$

where $F_{H\alpha}$ is the flux in a 3.6 Å rectangular bandpass centered on the H α line and F_{V_H} and F_{R_H} are the fluxes in two 2.2 Å rectangular bandpasses centered on the continuum points 6558.85 Å and 6567.30 Å. Equation (4.2) is taken from Petit et al., 2013 while Equation (4.3) is taken from Gizis, Reid, and Hawley, 2002.

4.1.2 R_x Indicators

In addition to these basic indices, there are R_x ² indices which are corrected for the photospheric or bolometric flux (Wright et al., 2004). The definition of the R_{HK} index is followed by Noyes et al., 1984 and Middelkoop, 1982 using the s index (S) and the B-V flux³

$$R_{HK} = 1.34 \times 10^{-4} C_{cf} S$$

, where C_{cf} is an empirical cubic fit defined by Middelkoop, 1982 as,

$$C_{cf}(B - V) = 1.13 \times (B - V)^3 - 3.91 \times (B - V)^2 + 2.84 \times (B - V) - 0.47. \quad (4.4)$$

The R'_x indicators are constructed using the R_x indicators and subtracting the photospheric flux to get rid of the photospheric component from the index and to determine the contribution of the star's luminosity in the particular spectral line. For Ca II H & K lines R'_{HK} index is defined by Hartmann et al., 1982 as follows:

$$R'_{HK} = R_{HK} - R_{phot},$$

where, R_{phot} is defined as

$$\log R_{phot} = -4.898 + 1.918 \times (B - V)^2 - 2.893 \times (B - V)^3. \quad (4.5)$$

While calculating these indices, as the stellar flux is very low in many cases, relatively broad filters are used to capture the photons. The ratio indices have integrated fluxes in their numerators and denominators. The line core and the wings are formed at different heights in the stellar atmosphere. For example, the cores of H α and the Ca II H & K lines are formed in the chromosphere. But as wavelength increases or decreases with respect to the line core, the radiation is formed further down in the atmosphere and towards the wings of the line (for e.g. the $K_1(H_1)$ features of the Ca II H & K lines), is formed in the photosphere. So we integrate the fluxes from different layers of the star to calculate the index.

² x can represent the HK flux, IRT, or H α , or in the x-ray regime, x-ray flux.

³the B-V colour index is defined by taking the difference between the magnitudes, or brightness of the star in the blue (400 nm) and visual regions (500 nm) of the spectrum.

4. Stellar Activity

These indices are ‘stellar activity indices’ and not solely chromospheric indices, but as the line cores of Ca II H & K and H α are formed in the chromosphere, these are often misinterpreted as chromospheric activity indicators.

On the other hand, mm continuum radiation is formed in the chromosphere; shorter wavelengths in the lower chromosphere and longer wavelengths in the higher chromosphere until the transition region. As the mm continuum is formed in LTE, these can be readily transformed into brightness temperatures which can give us temperature stratification with observations at different mm wavelengths. Owing to these advantages, chromospheric activity can be traced by using mm continua. The challenge that this diagnostic has is that the observations are scarce and difficult to calibrate as seen in [Chapter 3](#). The chromospheric activity indicator (α_{mm}) constructed by Mohan et al., 2022 is sensitive to the thermal stratification in the chromosphere, thus captures only the chromospheric activity of the star.

4.1.3 Understanding the ratios

In the papers in this thesis, the focus had been the traditional activity indicators described in [Section 4.1.1](#). In the case of stellar studies, the spectra are not resolved, i.e. for the whole star, there is one spectrum with which the indicators are calculated. In the Sun-as-a-star case, i.e. when we are looking at the star in a resolved manner, there are significant fluctuations in the photospheric and chromospheric activity which contributes to the indicators. To understand the effects of the contributions in a very well-resolved atmospheric model like Bifrost (described in [Chapter 3](#)) from different atmospheric layers to these indices, I performed a case study.

For the publicly available Bifrost model, we performed the synthesis of a Ca II model atom with 5 levels and calculated s index as per [Equation \(4.1\)](#) for each pixel. The density plots and contour plots of the *numerator*, i.e. the sum of integrated fluxes over the triangular filters over H and K lines, are plotted against the *denominator* which is the sum of the integrated fluxes over the rectangular filters over the V and R continuum bands. This is seen in [Figure 4.5](#). The upper and right side panels are plotting denominator and numerator histograms, respectively. The numerator shows one clear peak from the quiet region, and a decreasing tail goes off to higher activity, owing to fewer pixels with the enhanced network, as the model is mainly a quiet sun model (photospheric magnetic field strength seen in Fig.2 of Carlsson et al., 2016). The denominator shows two clear peaks, one sharp peak with a lower intensity which would be from intergranular lanes and a broader lower peak from granules, as their intensity would be higher than the lanes.

The denominator clearly shows the photospheric activity and that is also seen in the inset s index plane. The colour bar is truncated in this case to 1, which clearly shows the photospheric granulation features and the enhanced network footpoints are washed out in this case. This signifies that if the activity is not prominent, the s index reports photospheric activity rather than chromospheric or general stellar atmospheric activity. In the plot, the FAL F and D 1D models

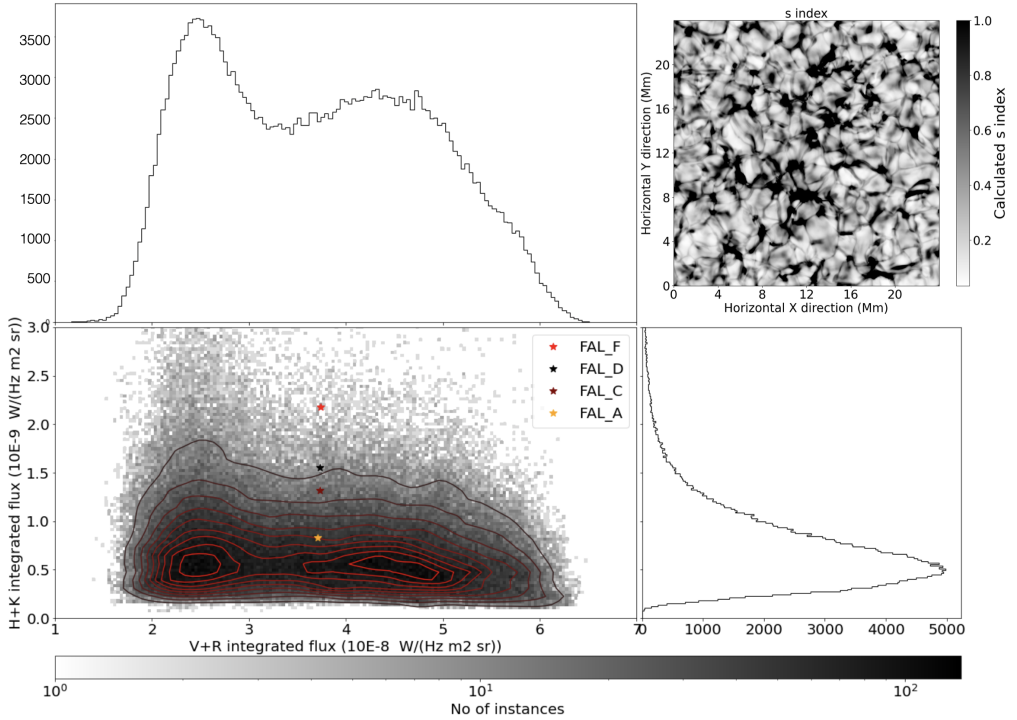


Figure 4.5: Scatter plot for the values of the numerator and denominator of the s index as described in Equation (4.1) for the Bifrost model as described in Chapter 3. The contours and the histograms on the right and top show the density distribution for the numerator and the denominator respectively. Datapoints for FAL models (Fontenla, Avrett, and Loeser, 1993) are plotted for comparison with a reference.

are also plotted for reference (Fontenla, Avrett, and Loeser, 1993). These are quiet sun models, F being the most active and A, being the least active. They fit right in the average activity between granules and intergranular lanes and in the case of the numerator, they show the level of activity as per their definitions.

To understand the numerator vs denominator behaviour of the s index depending on activity, different regions of the simulation box were isolated. In Figure 4.6, the left panel is for the enhanced network patch and the right one is for the quiet sun patch. The colour bar in both cases indicates the extent of the s index. For the enhanced network regions, the s index goes beyond 5 for some pixels and for the quiet region, it goes up to 2. The pink contours are for the whole simulation box (same as in Figure 4.5), whereas the green on the left and black on the right are the line contours for enhanced network and quiet sun, respectively. We can see the two distinct population densities in the denominator, which correspond to intergranular lanes at lower intensity and granules at higher intensity. These values are similar to each other and the whole

4. Stellar Activity

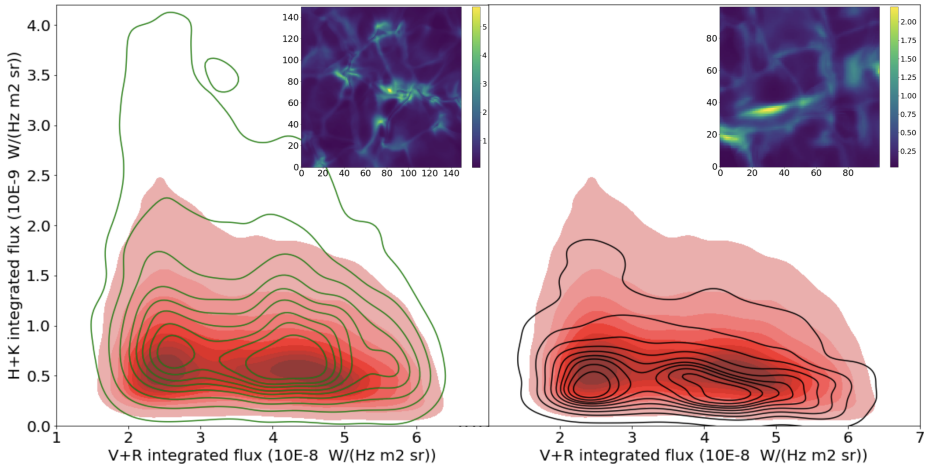


Figure 4.6: Contour plot same as in Figure 4.5 shown in pink filled contours, the green and black contours on the left and right show the difference in density distribution in more active enhanced network patch and a quieter patch shown in respective insets.

simulation box. On the other hand, the numerator varies in the three cases. For the enhanced network patch, it is much higher than the whole simulation box and for the quiet sun patch, it is much lower. This indicates that the integrated H and K fluxes are more sensitive to activity.

Therefore, in Paper II, while calculating the activity indicators, we use the averaged photospheric V and R fluxes as intended by the stellar physics definitions, by using averaged photospheric continuum values. This avoids any contributions to the indicator from the photosphere, making the s index and CaII IRT index a comparatively truer chromospheric indicator in this case. But, the filters are so broad that the contributions from the lower chromosphere and upper photosphere still seep in the integrated fluxes and make these indices representatives of the lower atmospheric layers, rather than the chromosphere. This is further addressed in Paper II.

Chapter 5

Contextual Description and Summary of Papers

The preceding four chapters laid the foundation for my specific scientific research, which I will now summarise and further justify. Here, you will find an account of the challenges we aimed to address. This chapter provides a brief summary of the papers that make up this thesis. It is spread over three papers (Pandit, Wedemeyer, and Carlsson, 2023; Pandit et al., 2023a,b)(Paper I, Paper II and Paper III) which broadly focus on the comparison of mm data with H α linewidth, Ca II activity indicators in synthetic data, and the long term variation in the activity indicators, like s index, using various observational data including ALMA total power maps. In addition, Paper I and Paper II included the observational data for a solar-like star α Cen A. Detailed summaries of the papers are provided below.

5.1 Comparison of chromospheric diagnostics in a 3D model atmosphere: H α linewidth and mm continua

In Paper I, we use the enhanced network Bifrost model to generate synthetic observables, namely, H α and the brightness temperatures at mm wavelengths observable through ALMA (0.3 mm to 8.5 mm). The H α linewidth compared with the brightness temperatures for one observational dataset by Molnar et al., 2019 is used for comparison. We encountered different definitions of linewidths and for our study, we used definitions by Leenaarts, Carlsson, and Rouppe van der Voort, 2012, called line core widths, and by Cauzzi et al., 2009 for the datasets. We also explored the effect of both the spatial and temporal resolution, on the correlations. Reducing the spatial resolution, or temporal resolution, of these synthetic observations to ALMA resolution decreases the standard deviations of the synthetic observables, leading to increased correlations between them. The H α line core widths correlate best with the mm continuum brightness temperatures at a wavelength of 0.8 mm, i.e. ALMA Band 7 at both, higher and lower spatial resolutions, as well as for the time-averaged datasets.

The definition of the linewidths considered was used exactly as in Molnar et al., 2019 so that the work can be directly compared. It is important to note that the calculated chromospheric line profiles from the Bifrost model are narrower than the observations in the literature and this affects the comparison with observations. An alternative definition of linewidth for comparison with Molnar et al., 2019 would have been to use a definition of the "continuum" wavelengths based on a similar position in the narrower Bifrost mean profile

as in the wider observed profile. This would have potentially led to a higher formation height, more similar to that in Molnar et al., 2019.

However, it is important to stress that a *formation height for the linewidth*, i.e. the average formation height of the red and blue wavelengths for calculation of linewidths, based on the optical depth unity height is at best indicative. For the H α line, the opacity is very temperature sensitive (because the lower level is a highly excited energy level). This means that the optical depth unity height jumps from the chromosphere to the photosphere discontinuously when going from the line core towards the line wing, as there is basically no opacity in the H α line in the temperature minimum region. The contribution to the intensity at the wavelengths close to the line core can then come predominantly from the chromosphere, even when the optical depth unity height is in the photosphere. This is what happens for our widths based on the Molnar et al., 2019 definition — the optical depth unity height for the red and blue wavelengths for calculation of linewidths is mostly in the photosphere but the width map is chromospheric in appearance. A further study with a narrower definition of the continuum will enhance the scientific understanding.

5.2 EMISSA (Exploring Millimeter Indicators of Solar-Stellar Activity). III. Ca II indices and mm continua

The [Paper II](#) is third in the series "*EMISSA (Exploring Millimeter Indicators of Solar-Stellar Activity)*" which focuses on the Ca II activity indices in comparison to the brightness temperatures observable through ALMA, using the synthetic observables computed with the RT code RH1.5D in the case of Ca II intensities, and with ART in the case of mm brightness temperatures, with the enhanced network Bifrost model as the input. This publication can be seen as the natural follow-up of the first paper. Here, we compared the Ca II activity indices, described in [Chapter 4](#), in [Equation \(4.1\)](#) and [Equation \(4.2\)](#), with the ALMA brightness temperatures. The Ca II indices and mm brightness temperatures are closely linked, forming in similar layers in the atmosphere for a wavelength range of 0.3-1.0 mm and providing constraints on the thermal stratification of a star. The s index and Ca II IRT index reveal mid-photosphere - lower chromosphere features, such as reverse granulation and internetwork structures. These indices demonstrate a remarkable similarity and exhibit the highest correlation with the ALMA Band 10 data. Therefore, these indicators of stellar activity are heavily influenced by photospheric emission, even though the line cores are formed in the chromosphere. Consequently, based on this study with the 3D enhanced network model of the solar atmosphere, they should not be considered solely chromospheric activity indicators as previously described in the literature. As the correlation between the two diagnostics is high even in the case of lower resolution, this study in addition to the work presented in [Paper I](#) may prove useful in mitigating the challenging task of calibrating mm continuum solar data obtained from ALMA.

5.3 EMISSA (Exploring Millimeter Indicators of Solar-Stellar Activity). IV. Full-disk observations of the Sun

Following [Chapter 4](#), all available total power (TP) maps are used to find out the variation in the ALMA data due to the solar activity cycle. Even though the data is sparse and sporadic the solar activity cycle is observed in the brightness temperatures and the active region area coverage of the ALMA TP data, detailed in [Paper III](#). Other datasets such as the s index and microwaves from the Nobeyama observatory in the range of 1 to 17 GHz are used as reference time-series for the solar activity. We present the first-ever long-term solar activity variation found in ALMA data. With the change in the activity, the correlation between the full disk data from SDO AIA channels and the ALMA TP data fluctuates. ALMA data also shows short-term variation. Considering the strong correlation with ALMA data outlined in this paper, it is worth exploring the potential of incorporating SDO AIA data from the 304, 1600, and 1700 channels, which originate from similar altitudes, to enhance the TP calibration process.

5.4 Concluding Remarks and Future Prospects

The results in [Paper I](#) and [Paper II](#) are based on the synthetic data from the Bifrost model. The model is observed to underestimate the chromospheric activity, like temperature, $H\alpha$ linewidth, Mg II h & k fluxes, Ca II H & K fluxes, to name a few. The work in this thesis is affected by this limitation, but comparison with the ALMA observation can push the 3D model to account for physical phenomena in a better manner.

It is important to note that the correlation coefficients used in the work to compare two quantities, like synthetic ALMA brightness temperatures to activity indicators like $H\alpha$ linewidth or s index in [Paper I](#) and [Paper II](#), or like comparing SDO AIA maps to ALMA TP maps in [Paper III](#), are calculating one number using two 2D datasets. The Pearson correlation coefficient is a robust measure, but cannot account for the spatial structures and hence we use power spectral density (PSD) in [Paper I](#) to address this limitation to account for the spatial structures.

As per expectation based on observational studies, like [Molnar et al., 2019](#), the mm data in Band 3, or near 3 mm, would have been the closest match (with the highest correlation coefficient), but the results from the synthetic data in [Paper I](#) did not agree with this hypothesis. We found in [Paper II](#) that the ALMA band probing even lower atmospheric layer correlated best with the s index. This could be one of the limitations of the model atmosphere, but also, there are hardly any observations available to verify this result right now. Hence, I am eagerly waiting for ALMA to start observing the Sun in other bands to use the full potential of ALMA for looking at the outer atmospheres of the closest main sequence star and potentially getting better insights into its temperature stratification.

The *chromospheric-coronal heating problem* is tirelessly studied from different

vantage points by the solar physicist community. One hurdle can be overcome by calibrating the solar ALMA data better. Using closely correlated SDO AIA data from 304, 1600 and 1700 channels, it is possible to use the nonrescaled TP data and get better-calibrated data. We conclude that the calibration process for ALMA solar data needs to be revisited and one of the suggestions for calibration can be using SDO data. Also, we find that the SDO 1600 and 1700 data is not corrected precisely for the instrumental degradation and we suggested that correction will be useful for the solar community at large. Another way to look at the problem at hand is to look further away, at other stars and to use the power of statistics of stellar data. The use of activity indicators in the GHz range for comparison of stellar activity to solar activity using the Sun-as-a-star approach is described in the first two EMISSA papers (Mohan et al., 2021, 2022), and the [Paper III](#) in the thesis. Superior sensitivity of millimetre continuum observations towards chromospheric structures gives a 3D perspective of the chromosphere in a better manner. Hence, mm brightness temperatures can be used as alternative and complementary chromospheric activity indicators.

Using these indicators, the stellar samples can be studied in a more comprehensive manner. The stellar activity, which is inherently dependent on age, rotation speed and metallicity, can be corrected and the stellar evolution can be studied in better detail. The question of habitability and sustainability of life on exoplanets revolving around Sun-like stars depends heavily on this understanding.

Papers

Paper I


Comparison of chromospheric diagnostics in a 3D model atmosphere: $H\alpha$ linewidth and mm continua

Sneha Pandit, Sven Wedemeyer, Mats Carlsson, Mikołaj Szydlarski

Published in: *Astronomy and Astrophysics*, Vol. 673, no. A137 (2023)
DOI: [10.1051/0004-6361/202245412](https://doi.org/10.1051/0004-6361/202245412)

Comparison of chromospheric diagnostics in a 3D model atmosphere

H α linewidth and millimetre continua

Sneha Pandit^{1,2} , Sven Wedemeyer^{1,2} , Mats Carlsson^{1,2} , and Mikołaj Szydlarski^{1,2}

¹ Rosseland Centre for Solar Physics, University of Oslo, Postboks 1029 Blindern, 0315 Oslo, Norway

² Institute of Theoretical Astrophysics, University of Oslo, Postboks 1029 Blindern, 0315 Oslo, Norway
e-mail: sneha.pandit@astro.uio.no

Received 8 November 2022 / Accepted 24 March 2023

ABSTRACT

Context. The H α line, one of the most studied chromospheric diagnostics, is a tracer of magnetic field structures, while the intensity of its line core provides an estimate of the mass density. The interpretation of H α observations is complicated by deviations from local thermodynamic equilibrium (LTE) or instantaneous statistical equilibrium conditions. Meanwhile, millimetre (mm) continuum radiation is formed in LTE, and therefore the brightness temperatures from Atacama Large Millimetre-submillimetre Array (ALMA) observations provide a complementary view of the activity and the thermal structure of stellar atmospheres. These two diagnostics together can provide insights into the physical properties of stellar atmospheres, such as their temperature stratification, magnetic structures, and mass density distribution.

Aims. In this paper, we present a comparative study between synthetic continuum brightness temperature maps at mm wavelengths (0.3 mm to 8.5 mm) and the width of the H α 6565 Å line.

Methods. We used the 3D radiative-transfer codes Multi3D and Advanced Radiative Transfer (ART) to calculate synthetic spectra for the H α line and the mm continua, respectively, from an enhanced network atmosphere model with non-equilibrium hydrogen ionisation generated with the state-of-the-art 3D radiation magnetohydrodynamics (rMHD) code Bifrost. We use a Gaussian point spread function (PSF) to simulate the effect of ALMA's limited spatial resolution and calculate the H α versus mm continuum correlations and slopes of scatter plots for the original and degraded resolution of the whole box, quiet sun, and enhanced network patches separately.

Results. The H α linewidth and mm brightness temperatures are highly correlated and the correlation is highest at a wavelength of 0.8 mm, that is, in ALMA Band 7. The correlation systematically increases with decreasing resolution. On the other hand, the slopes decrease with increasing wavelength. The degradation of resolution does not have a significant impact on the calculated slopes.

Conclusions. With decreasing spatial resolution, the standard deviations of the observables, H α linewidth, and brightness temperatures decrease and the correlations between them increase, but the slopes do not change significantly. These relations may therefore prove useful in calibrating the mm continuum maps observed with ALMA.

Key words. radiative transfer – Sun: chromosphere – Sun: radio radiation – line: profiles – methods: numerical – radio continuum: stars

1. Introduction

One of the most commonly used chromospheric diagnostics is the H α line, that is, the transition between atomic levels 3 and 2 in the hydrogen atom (Cram & Mullan 1985). Because of its high opacity in the line core, the H α line core forms in the low plasma beta regime, where there is more dominant magnetic pressure than the plasma pressure, which results in magnetic fields being the main structuring agent in the upper chromosphere (Leenaarts et al. 2012). For this reason, the H α line is a very good diagnostic for the magnetic structures in the chromosphere. The chromospheric mass density can be traced with the H α line core intensity (Leenaarts et al. 2012). The low atomic mass of hydrogen results in high-temperature sensitivity of the H α line width through significant thermal Doppler broadening (Cauzzi et al. 2009). Even though the H α line is a useful diagnostic of stellar chromospheres –because it forms in non-local thermodynamic equilibrium (NLTE)–, it is not particularly suitable for determination of the chromospheric temperature stratification (Pasquini & Pallavicini 1991).

Based on radiative-transfer calculations for a solar atmospheric radiation–magnetohydrodynamics (rMHD) simulation (Carlsson et al. 2016), Leenaarts et al. (2012) show that the H α line width is correlated with the temperature of the plasma, while the line core intensity is a diagnostic of the mass density in the chromosphere. These relations come from the fact that the H α line is a strongly scattering line such that the source function is non-locally determined by the mean intensity. A high local temperature means that the atomic absorption profile becomes wide (because of the low atomic mass, the width of the profile is dominated by thermal broadening), and we also get a wide intensity profile because the source function is rather insensitive to the local conditions. A high mass density in the chromosphere leads to line-core formation at a larger height where the source function is lower, and therefore lower line-core intensity.

It is well established that the continuum radiation at millimetre (mm) wavelengths is formed at chromospheric heights (see e.g. Wedemeyer et al. 2016, and references therein). The continuum radiation at mm wavelengths (here 0.3–8.5 mm) originates from free-free emission in the chromosphere, and the two

main opacity sources are H and H⁻ free-free absorption (Dulk 1985). These processes result in a LTE source function as they are coupled to the local property of the plasma: the electron temperature. We can therefore use the Rayleigh-Jeans law and interpret the emergent intensity (the observed brightness temperature (T_b)) in the mm wavelength domain as local electron temperature (Loukitcheva et al. 2015). For this reason, the mm continuum is a very convenient diagnostic for understanding the temperature stratification in solar and stellar atmospheres (Wedemeyer-Böhm et al. 2007; Wedemeyer et al. 2020).

The H α line opacity is proportional to the hydrogen $n = 2$ level population; the H α optical depth scales with the $n = 2$ column density (Leenaarts et al. 2007). The availability of free electrons is dependent on the $n=2$ population of hydrogen in the upper atmosphere (Molnar et al. 2019). The formation of the H α and mm continuum is influenced by the plasma temperature, the H($n = 2$) level populations, and electron populations.

Traditional H α activity indicators, such as linewidth, full width at half maximum (FWHM), or integrated fluxes depend on several wavelengths across the line profile (Hanuschik 1989; Gizis et al. 2002; Marsden et al. 2014; Molnar et al. 2019). The H α line core is formed higher in the atmosphere than the wings, and therefore while calculating these activity indicators from observations, we inherently look at a large volume of plasma in the chromosphere (Vitas et al. 2009), which makes determining the thermal stratification difficult. In this regard, the mm continuum has an additional advantage as a complementary diagnostic, namely that –to a first approximation– the radiation at a given mm wavelength originates from approximately the same height range with the average formation height range increasing as a function of wavelength. While this assumption is probably valid on average, we note that the exact formation height ranges might show variations because of the surface corrugation, which is investigated here (see e.g. Eklund et al. 2021; Wedemeyer et al. 2022; Hofmann et al. 2022, and references therein). On the other hand, the formation height of the H α line is in the range of 0.5 Mm to 3 Mm above the photosphere, which is a large range (Leenaarts et al. 2012).

The Atacama Millimetre/submillimetre Array (ALMA; Wootten & Thompson 2009) provides observations with a high spatial and temporal resolution for the mm continuum. The H α linewidth and mm continua both depend on the temperature and the electron density of the volume of plasma where they are formed. In the present work, we focus on using these two as complementary diagnostics, similar to the case study on co-observational data for ALMA Band 3 and IBIS in Molnar et al. (2019). Here, we compare the mm continuum and H α linewidth synthesised from a 3D realistic Bifrost model atmosphere to understand how these can be used as complementary diagnostics for the chromosphere. Our model and spectral synthesis are described in Sect. 2. In Sect. 3, we present a quantitative comparison of the two diagnostics, which is further qualitatively discussed in Sect. 4. Finally, we present our conclusions in Sect. 5.

2. Methods

We used a snapshot of a numerical 3D simulation of the solar atmosphere (see Sect. 2.1) as input for radiative-transfer codes to compute the H α line intensity (see Sect. 2.2) and the continuum intensity at mm wavelengths (see Sect. 2.5). We then degraded the resulting maps for different wavelengths to a spatial resolution typically achieved with ALMA as described in Sect. 2.6, before determining the H α line width and comparing it to the mm brightness temperatures.

2.1. Three-dimensional model atmosphere

Bifrost is a 3D radiation magnetohydrodynamics (rMHD) simulation code that includes physics relevant to chromospheric conditions (Gudiksen et al. 2011). The model used for this study is taken from a continuation of the enhanced network simulation en024048 at 17 min after the publicly released snapshots from Carlsson et al. (2016). The computational box of this model extends 24 Mm \times 24 Mm horizontally, and vertically from 2.4 Mm below the visible surface to 14.4 Mm above it, thereby encompassing the upper part of the convection zone, the photosphere, chromosphere, transition region, and corona. The computational box consists of 504 \times 504 \times 496 grid points with a horizontal resolution of 48 km, which corresponds to an angular size of approximately 0.066 arcsec. The grid is non-equidistant in the vertical direction, varying from 19 km in the photosphere and chromosphere up to a height of 5 Mm and then increasing to 100 km at the top boundary. Both the top and bottom boundaries are transparent, whereas lateral boundary conditions are periodic. At the bottom boundary, the magnetic field is passively advected with no extra field fed into the computational domain. For further details, see Carlsson et al. (2016, and references therein).

The temperature and absolute magnetic field showing the loops of the enhanced network with the quiet region at typical chromospheric heights are shown in Fig. 1. As seen in Figs. 11 and 12 in Carlsson et al. (2016), the simulation has different regions. The en024048 simulation features an enhanced network (EN) patch with loops in the middle of the computational domain as seen in Fig. 2 in Loukitcheva et al. (2015) or (see the black square in Figs. 3 and 4), whereas the outer parts are more representative of magnetically less active, quiet Sun (QS) conditions. In the absolute magnetic field slice through 1.74 Mm (Fig. 1b), the footpoints of the magnetic loops are seen. The gas temperatures at those heights are comparatively lower at locations with higher magnetic strengths, and the loops show significantly higher temperatures in the range of 2 to 3 MK from the footpoint to the apex of the loop.

2.2. H α spectral line synthesis

Multi3D (Leenaarts et al. 2009) employs the accelerated lambda iteration method developed by Rybicki & Hummer (1992) with the extension to treat effects of partial frequency redistribution using the angle averaged approximation by Uitenbroek (2001). We used a five-level plus continuum hydrogen model atom. Microturbulence is not introduced, as Leenaarts et al. (2012) show that the synthesised spectra are similar to observational spectra even without using microturbulence. Further details of how the H α spectra are synthesised in 3D using Multi3D can be found in Leenaarts et al. (2012).

2.3. H α observations of α Cen A

In this study, H α observations of the solar-like star α Cen A are used for comparison. The data were acquired from Porto de Mello et al. (2008) and Lyra & Porto de Mello (2005). The H α observations were collected at Observatório do Pico dos Dias (OPD), which is operated by the Laboratório Nacional de Astrofísica (LNA), CNPq, Brazil on the ESPCOUDE 1.60m telescope. The data were wavelength-calibrated, Doppler-corrected, and flux-normalised to unity by Porto de Mello et al. (2008).

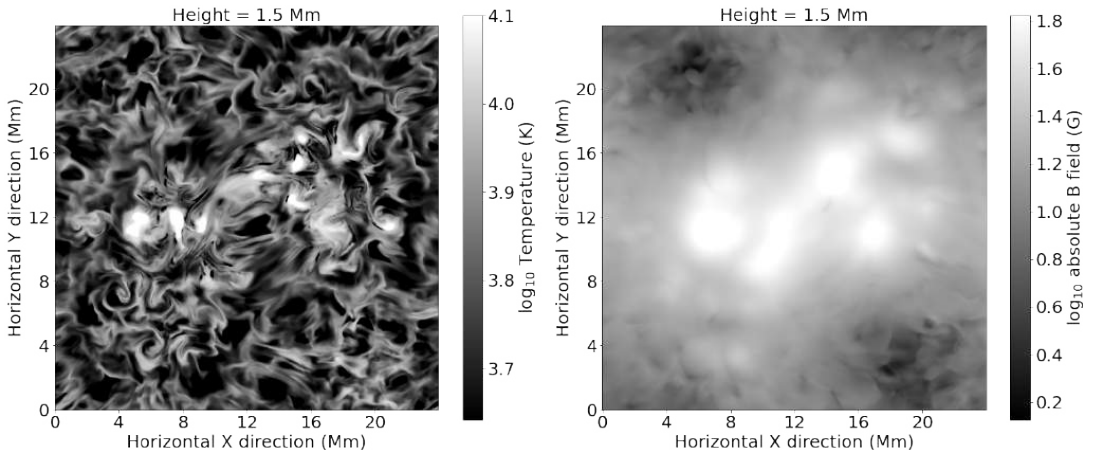


Fig. 1. Horizontal cross-section of temperature (left) and the absolute magnetic field ($|B| = \sqrt{B_x^2 + B_y^2 + B_z^2}$) (right) from a snapshot of the Bifrost simulation at a constant height of 1.5 Mm from the surface.

2.4. Definition of linewidth

As this study is based on forward modelling, we use the definition of linewidth put forward by [Leenaarts et al. \(2012\)](#). However, we note that different definitions of the $H\alpha$ linewidth are used in the literature. The definition of core width given by [Leenaarts et al. \(2012\)](#) and the definitions used by [Cauzzi et al. \(2009\)](#) and [Molnar et al. \(2019\)](#) are compared to the definition of FWHM for the linewidth in Fig. 2

The [Leenaarts et al. \(2012\)](#) $H\alpha$ line-core width calculated for the Bifrost model is the full width at one-tenth maximum, which is the separation between the line wings at $I = I_{\min} + 0.1(I_{\max} - I_{\min})$. The representative wavelengths for the red and blue line wing that span the core width are calculated by first identifying the two spectral sampling points which are closest to one-tenth of the intensity between the pseudo continuum and the line core and then using linear interpolation.

[Molnar et al. \(2019\)](#) follow the definition by [Cauzzi et al. \(2009\)](#) for their observational study, and these authors define linewidth as the separation of the line profile wings at half of the line depth, where the maxima are defined at $\pm 1\text{\AA}$ from the line core (referred to as the [Molnar et al. \(2019\)](#) definition of linewidth hereafter). The line-core intensity calculated for the Bifrost model used in this study reveals the structure of the EN loops. The variation in the activity in the model atmosphere among QS and EN regions is also visible from the variation of the $H\alpha$ line core intensity. It is to be noted that throughout the paper, the wavelengths mentioned are vacuum wavelengths.

The resulting line core width according to the [Leenaarts et al. \(2012\)](#) definition is shown in Fig. 3a. Please note that the plotted value ranges for these maps have been limited to the 99th to 1st percentile for better visibility, and in particular to highlight the imprints of the loop structures in contrast to the less active surroundings.

2.5. Synthesis of mm continuum brightness temperatures

The intensity of the continuum radiation at mm wavelengths for the 3D input model (see Sect. 2.1) is calculated with the Advanced Radiative Transfer (ART) code by

[de la Cruz Rodríguez et al. \(2021\)](#). The output intensities I_l are then converted to brightness temperatures T_b using the Rayleigh-Jeans approximation:

$$T_b = \frac{\lambda^4}{2k_B c} I_l, \quad (1)$$

where, λ , k_B , and c are the wavelength and Boltzmann constant and the speed of light, respectively. In total, maps for 34 wavelengths are computed, covering the range that in principle can be observed with ALMA. This includes both currently available receiver bands and bands that might be offered for solar observations in the future. The resulting maps for the wavelengths of 3.0 mm and 0.8 mm are presented in Figs. 3 and 4, respectively, while further maps for selected wavelengths are shown in Appendix A (Figs. A.1–A.8).

2.6. Image degradation

In principle, the synthesised beam for interferometric observations with ALMA, that is, the effective point spread function (PSF), depends on several factors, such as the angle of the Sun in the sky with respect to the array baselines and the configuration of the antennas. The resulting beam would be typically elliptical, while the Fourier space of the source (here the Sun) would only be sampled sparsely (see e.g. [Högbom 1974](#); [Boone 2013](#)). For this theoretical study, circular Gaussians are used as PSFs as a first approximation, as this simplified approach is sufficient to demonstrate the effect of spatial resolution. The more detailed modelling of the ALMA beam would depend on the exact array configuration, receiver band (some of which are not yet used for solar observations), and details of the imaging process, which would go beyond the scope of this study ([Wedemeyer et al. 2022](#)).

As mentioned above, the exact shape and width of the synthetic beam varies even for observations in the same receiver band. For instance, the data sets found on the Solar ALMA Archive (SALSA, [Henriques et al. 2022](#)) have widths of around $2''$, which includes the beam with a width of $1.92'' \times 2.30''$ for the data set 2016.1.01129.S. That data set was also used by

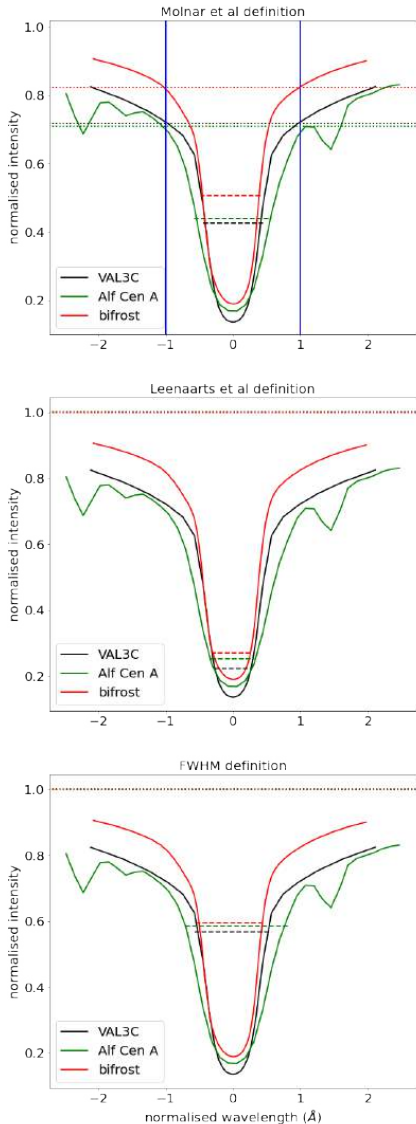


Fig. 2. Comparison of the linewidth as defined by Molnar et al. (2019; upper panel), by Leenaarts et al. (2012; middle panel) and as defined as the FWHM (lower panel). The red, black and green lines show normalised spectra for the VAL C model, Bifrost QS and the observed spectrum for α Cen A (Porto de Mello et al. 2008), respectively. The solid blue lines in the top panel mark $\pm 1\text{\AA}$, while the dotted lines show the considered maxima and the dashed lines show the calculated linewidths in all three cases.

Mohan et al. (2021), although their choice of imaging parameters results in a beam width of only $1.75'' \times 1.91''$. However, based on a comparison with $H\alpha$ observations, these latter authors instead chose a PSF with a width of $1.95'' \times 2.03''$. For simplicity in this study, the width of the beam (i.e. the PSF) is set to $2''$ at a wavelength of $\lambda = 3.0\text{ mm}$ and is then linearly scaled as a

function of the observing wavelength λ . The considered wavelength range includes the receiver bands that are already available for solar observations with ALMA (bands 3, 5 and 6, i.e. 2.59–3.57, 1.42–1.90 and 1.09–1.42 mm), but in addition also bands 1, 2, 4, and 7–10, thereby covering the whole range that might be offered in the future from 0.3 mm to 8.5 mm. The same wavelength-dependent Gaussian kernels are used for degrading the mm brightness temperature maps and the $H\alpha$ intensity maps. Please note that all three considered snapshots (with 5 min solar time between snapshots) are synthesised and then degraded with the different beams. In addition, corresponding time-averaged ALMA maps are calculated so that they can be compared to the observational data used by Molnar et al. (2019).

2.7. Semi-empirical models

For comparison, the 1D semi-empirical reference models Vernazza-Avrett-Loeser C (VAL C; Vernazza et al. 1981) and Fontella-Avrett-Loeser C (FAL C; Fontenla et al. 1993) are used, which are both representative of quiet Sun conditions. Corresponding $H\alpha$ line profiles and mm continuum intensities for these 1D semi-empirical atmosphere models are calculated with the radiative code RH (Uitenbroek 2001; Pereira & Uitenbroek 2015).

3. Results

3.1. Dependence on spatial resolution

Figure 3 shows a comparison between the EN and QS regions for the original and the degraded resolution corresponding to the assumed ALMA resolution at a wavelength of 3 mm. The calculated $H\alpha$ line core width for the whole box (panel a) is very similar to the results in Fig. 9a in Leenaarts et al. (2012). The $H\alpha$ line core width from the simulation (Fig. 9a in Leenaarts et al. 2012) appears to be formed at a lower height in the chromosphere than that suggested by observations (Fig. 16b in Leenaarts et al. 2012). As the employed wavelength points are very close to the line core, one should expect to see chromospheric features in the line-core width map. However, in contrast, the continuum intensity for 3 mm at the original resolution as shown in Fig. 3b differs notably from the line-core width shown in Fig. 3a.

The maps appear more similar at reduced resolution after convolution with a circular Gaussian kernel corresponding to the spatial resolution at the wavelength of 3 mm (see panels (d) and (e)). The black and red boxes on these maps denote the chosen EN and QS regions for further comparison. The EN region is chosen to be centred at the EN as seen in the degraded resolution, and the QS region is placed at the bottom right corner of the simulation box. Both boxes are of the same size, of namely $9.5\text{ Mm} \times 9.5\text{ Mm}$ (200 pixels \times 200 pixels).

Panels (c) and (f) of Fig. 3 show the scatter contour plots for the three sets of pixels: the whole simulation box, the QS box (red square in panels a,b,d,e), and the EN box (black square in panels a,b,d,e). The distribution for the whole simulation box is shown in red contours with the colour bar for the number of pixels falling into the individual bins. The QS and EN distributions are represented by green and blue contours, respectively. The distributions at the original resolution show substantially more spread than the distributions at degraded resolution because of the associated loss of variations on small spatial scales. This effect is already clear from a visual comparison of the $H\alpha$ linewidth maps in panels (a) and (d) and likewise

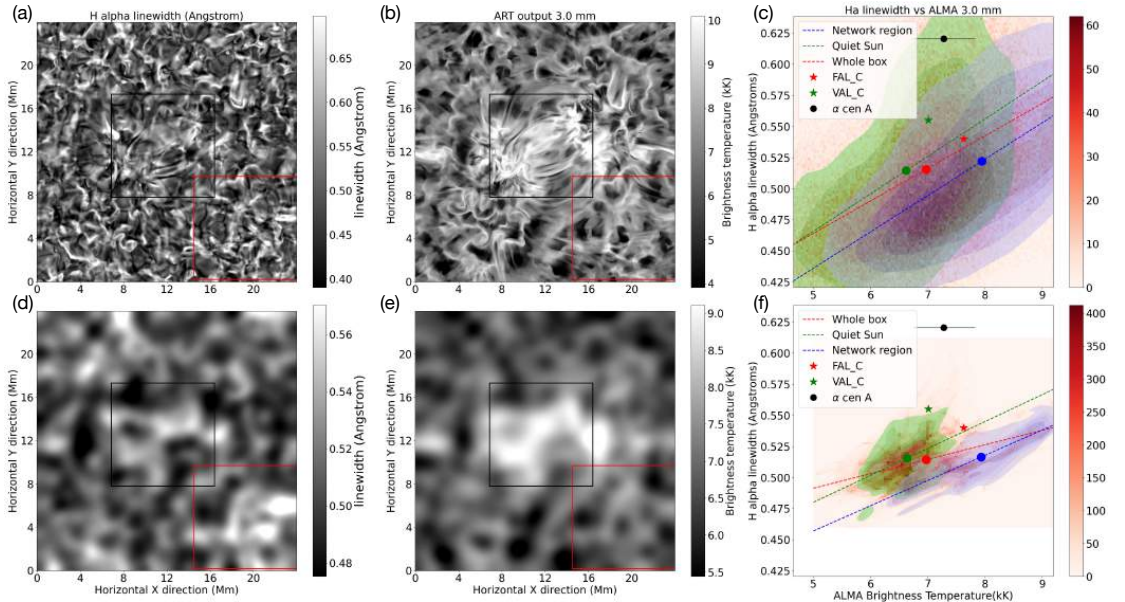


Fig. 3. Comparisons of the $H\alpha$ line core width (a,d) and ALMA at 3.0 mm brightness temperature maps (b,e) at original (top row) and degraded (bottom row) resolution. The black and red boxes on these maps denote the chosen EN and QS regions, respectively. The last column is a correlation contour plot between the $H\alpha$ linewidth and ALMA brightness temperature at 3.0 mm, with contours with linear fits (dashed lines) and means (circles) of the three cases: the whole simulation box in red, the QS box in green, and the EN region box in blue. The red and green star data points are for the FAL C and VAL C ID semi-empirical models and the black circle with error bars is an observational data point for the G2V type star α Cen A with a linewidth of 0.62 Å.

for the mm brightness temperature maps in panels (b) and (e), respectively. The red, green, and blue points in panels (c) and (f) represent the average values for the whole box, QS and EN, respectively. The impact of applying the ALMA beam can be seen from the spatial power spectral density plots in Fig. 5. As seen in the plots for 3.0 mm and 0.8 mm, the power spectral density (PSD) falls drastically for small spatial scales that are not resolved with the respective PSF (beam). Another notable observation is that both definitions of linewidth show similar values of power at larger scales. At smaller scales, the mm PSD is close to the PSD of the line-core-width definition, implying better correlations (see Table 1). Also, the observational 3 mm data show a very similar trend in PSD to the mm spatially degraded data, as expected.

In addition, the $H\alpha$ linewidth and the T_b at the mm wavelengths for the VAL C and FAL C semi-empirical model atmospheres are plotted for comparison. The VAL C model has consistently lower brightness temperature than the FAL C model, as seen in Fig. 6. When plotted on the linewidth-versus-temperature planes, these QS models lie in between the EN and QS distributions, demonstrating the agreement between the data from our study and the semi-empirical models. Applying the beam changes the mean T_b value for the QS and EN pixel sets as shown in Table 1. The mean EN T_b decrease and mean QS T_b increase leave the mean T_b of the whole box unchanged. This change in the mean and standard deviation of the brightness temperatures is further shown in Fig. 6 and discussed in Sect. 4.1. The T_b at 3 mm for the VAL C and FAL C models are calculated as 7009 K and 7624 K, respectively, which are similar to the corresponding average brightness temperature of 6968 K

across the whole horizontal extent of the 3D model employed here (see Table 1). The value for FAL C agrees with the calculations reported by Loukitcheva et al. (2004). The differences are further discussed in comparison to observations in Sect. 4.2. It should also be noted that the average QS $T_b = 6621$ K found for the 3D model is lower than the reference value of 7300 K suggested by White et al. (2017) for Band 3 ($\lambda = 3.0$ mm) at the centre of the solar disk. Please refer to Sect. 4.2 for further discussion.

The wavelength of 0.8 mm is of particular interest for this study, too, as will be discussed in Sects. 3.2 and 4.2. The results for $\lambda = 0.8$ mm are presented in Fig. 4, which corresponds to the above-discussed Fig. 3 for $\lambda = 3.0$ mm. While the $H\alpha$ line core width map at the original resolution (panel a) is the same in both figures, the mm brightness temperature maps (panel (b)) and the degraded maps (panels (d) and (e)) differ. The $H\alpha$ line core width map (Fig. 4a) and the mm continuum map at 0.8 mm (Fig. 4b) are already very similar at the original resolution and even more so at the lower resolution, as shown in Fig. 4d-e. The PSF at 0.8 mm is smaller in width compared to the 3.0 mm PSF by a factor of 0.8/3.0, which can be seen from a visual comparison of Fig. 3c and Fig. 4e. The 3.0 mm maps appear more blurred, mainly as a result of the wider PSF. The same effect can be seen for the $H\alpha$ line width maps, which were derived from the $H\alpha$ line-intensity maps after these were all degraded accordingly for each wavelength point.

The slopes in the EN and QS cases are very similar to each other and are also similar to the slopes for the whole box as seen in Table 1. In contrast to Fig. 3c and f, the scatter plots in Fig. 4c and f show that the slopes for the QS and EN distributions

Table 1. Brightness temperatures in kK, correlation coefficients, and slopes for the three pixel sets (whole box, QS, and EN) each for two resolutions (original and degraded) for the single snapshot and time-averaged dataset, with both the definitions used for calculating the linewidth.

	Original resolution			Reduced resolution			
	Wavelength	Whole box	QS	EN	Whole box	QS	EN
Single snapshot:		Line core width calculated with (Leenaarts et al. 2012) formula.					
Temperatures (kK)	0.8 mm	5.275	5.124	5.590	5.275	5.126	5.593
	3.0 mm	6.968	6.621	7.835	6.968	6.637	7.848
Correlation	0.8 mm	0.764	0.798	0.785	0.778	0.834	0.808
Coefficients	3.0 mm	0.524	0.516	0.628	0.453	0.520	0.813
Slopes	0.8 mm	0.047	0.052	0.045	0.041	0.047	0.040
	3.0 mm	0.026	0.030	0.029	0.012	0.022	0.020
Time-averaged:		Line core width calculated with (Leenaarts et al. 2012) formula.					
Temperatures (kK)	0.8 mm	5.111	4.881	5.609	5.111	4.881	5.609
	3.0 mm	6.862	6.367	7.891	6.862	6.371	7.878
Correlation	0.8 mm	0.668	0.705	0.712	0.696	0.751	0.755
Coefficients	3.0 mm	0.461	0.398	0.583	0.470	0.316	0.755
Slopes	0.8 mm	0.035	0.048	0.035	0.031	0.047	0.031
	3.0 mm	0.017	0.018	0.023	0.009	0.008	0.016
Single snapshot:		Linewidth calculated with Molnar et al. (2019) formula.					
Correlation	0.8 mm	0.733	0.746	0.797	0.770	0.813	0.854
Coefficients	3.0 mm	0.443	0.443	0.545	0.384	0.411	0.819
Slopes	0.8 mm	0.042	0.043	0.040	0.044	0.048	0.041
	3.0 mm	0.020	0.023	0.022	0.014	0.022	0.022
Time-averaged:		Linewidth calculated with Molnar et al. (2019) formula.					
Correlation	0.8 mm	0.729	0.692	0.837	0.771	0.724	0.894
Coefficients	3.0 mm	0.479	0.343	0.609	0.610	0.294	0.829
Slopes	0.8 mm	0.040	0.045	0.043	0.039	0.046	0.043
	3.0 mm	0.019	0.015	0.025	0.015	0.008	0.025

(0.052 and 0.045) are very similar to the values for the maps at degraded resolution. On the other hand, for 3 mm, the values are 0.03 and 0.029, which show a higher departure from each other. The mean T_b values for the QS region and the whole box are relatively close, as seen in Table 1, as the atmosphere is mainly QS. The VAL C and FAL C data points are closer to the mean T_b for the EN region, possibly because of the factors discussed above. Treating the synthetic mm and the $H\alpha$ linewidth map with the generated PSFs for corresponding wavelengths (see Appendix A for representative plots similar to Figs. 3 and 4 for ALMA bands), the scatter and the linear fits were plotted and the slopes and the correlation coefficients were calculated. The trends in correlations and slopes for all considered wavelengths are presented in Sect. 3.2 and shown in Figs. 7 and 8, respectively.

3.2. Correlations and slopes

The correlation of the $H\alpha$ linewidth maps and the mm brightness temperature maps and the dependence of this correlation on mm wavelength and therefore spatial resolution are quantified through the Pearson correlation coefficient between the $H\alpha$ linewidth maps and mm brightness temperature maps and linear

fits to the distributions, as shown for example in Figs. 3 and 4. The slopes, as well as the intercept of the linear fits, are calculated by linear regression for the whole box, and the EN and QS regions, separately.

The resulting correlation coefficients as a function of wavelength are shown in Fig. 7 at original resolution (black lines) and after degradation with the synthetic ALMA PSFs (red lines) corresponding to the wavelength. It should be noted that the mm brightness temperature maps exhibit differences as a function of wavelength which are due to the different formation height ranges at a given wavelength. Although the formation heights can vary notably across the model, they nonetheless increase on average with increasing wavelength. Consequently, the mm brightness temperature maps at original resolution show a maximum correlation with the $H\alpha$ linewidth maps at a given wavelength as can be seen most clearly from the peak for the QS correlation (black dotted line) for wavelengths in the range from 0.5 mm to 1.8 mm. Peaks are also present for the whole box and the EN region with a decrease towards shorter and longer wavelengths in all cases.

Reducing the spatial resolution has a notable impact on the correlation coefficients (see Fig. 7), resulting in generally higher values as compared to the correlation at the original resolution.

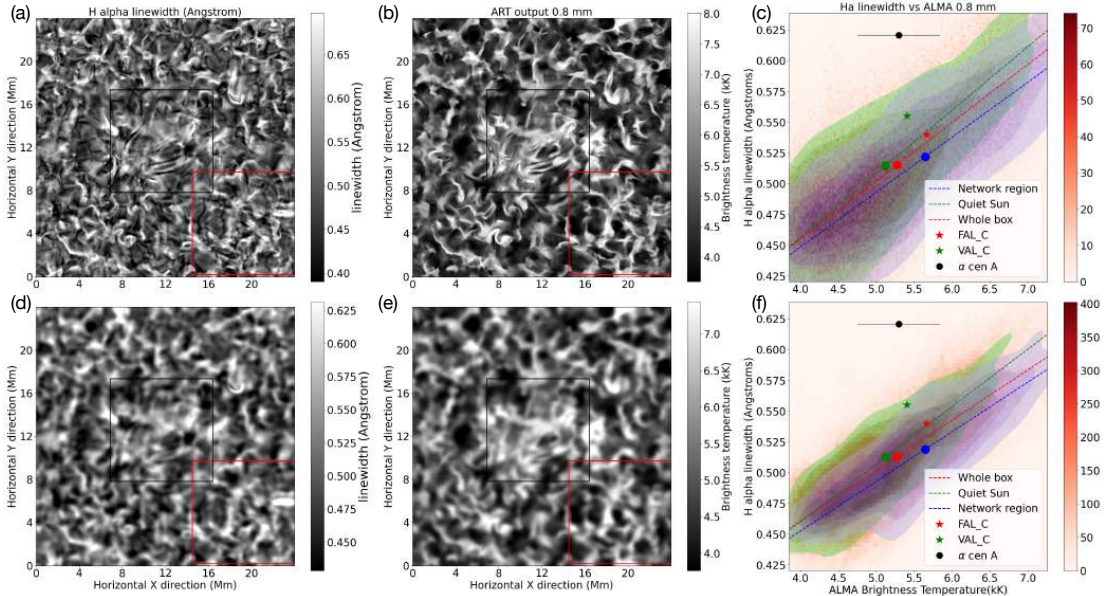


Fig. 4. Same as Fig. 3 but for a wavelength of 0.8 mm.

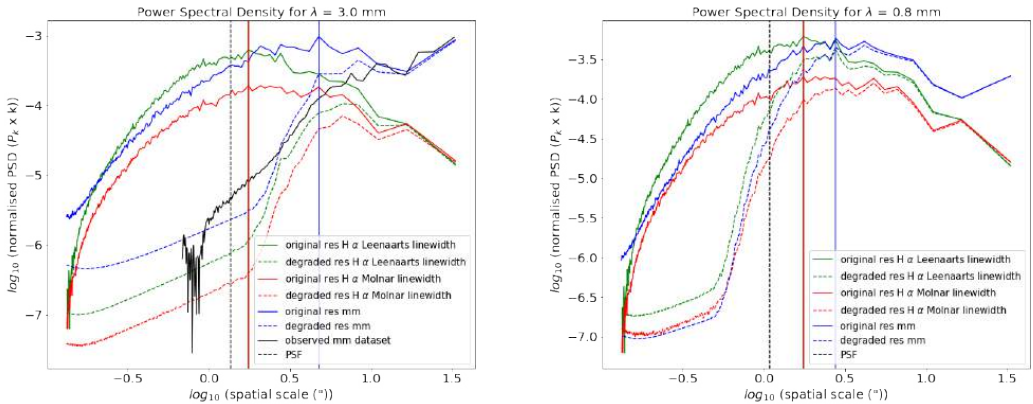


Fig. 5. Normalised power spectral density kP_k plots for time-averaged datasets of mm brightness temperatures with both definitions of linewidth at 3.0 mm and 0.8 mm. The solid lines represent the original-resolution data and the dashed lines show the spatially degraded data, green for the Leenaarts et al. (2012) linewidth, red for the Molnar et al. (2019) definition of linewidth, and blue for the corresponding mm wavelength. The vertical lines represent the dominant spatial scales (in arcsec) for the original-resolution data with the Leenaarts et al. (2012) definition of linewidth and the Molnar et al. (2019) definition of linewidth. The black dashed line represents the PSF corresponding to the mm wavelength, showing the resolution limit for the degraded dataset. In the left panel, the spatial power spectral density for the Band 3 ALMA observations (ADS/NRAO.ALMA#2016.1.01129.S) as used by Molnar et al. (2019) and shown in Fig. 11 are plotted as the black solid line. The power spectral density was calculated for all time steps in the time range considered by Molnar et al. (2019) and then averaged in time.

The QS region correlations are lower than for the whole box in both cases and the EN region correlations are slightly higher in the degraded resolution case and for most wavelengths for the original resolution. While the correlation for the degraded resolution maps also exhibits peaks, there is a systematic increase in the correlation between the degraded resolution maps as a function of wavelength for longer wavelengths. This effect can be attributed primarily to the spatial resolution, that is, the width

of the PSF, which increases with wavelength. Consequently, the structure below a corresponding (small) spatial scale is blurred, which affects the resulting correlation coefficient. With increasing wavelength, more and more of this atmospheric fine structure is blurred, as already discussed in Sect. 3.1 and seen from a comparison of Figs. 3 and 4 (see Table 1 for the correlation coefficients for 3.0 mm and 0.8 mm). However, at the longest wavelengths, even structure on relatively large spatial scales is

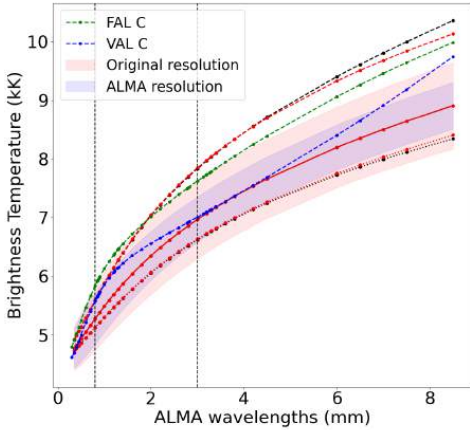


Fig. 6. Comparison of the mean brightness temperatures for mm wavelengths at the resolution of the original simulations (in black) and the resolution of the observations from the ALMA observatory (in red). In both these cases, the whole simulation box (solid lines), the QS box (dotted lines), and the EN box (dashed lines) are taken separately. The pink and blue shaded regions show a region of one standard deviation around the mean for the original resolution and the degraded resolution case, respectively. The green and blue dashed lines show brightness temperature trends for FAL C and VAL C models, respectively. The black dashed vertical lines mark 0.8 mm and 3 mm.

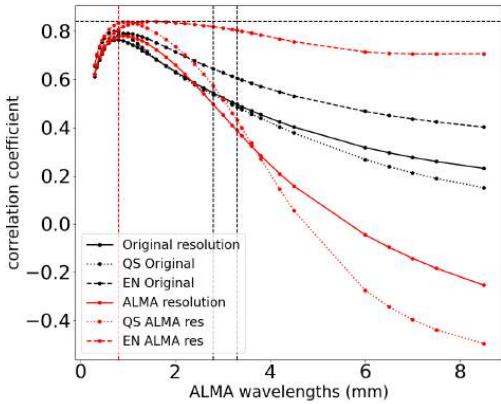


Fig. 7. Comparison of the calculated Pearson correlation coefficients with two different resolutions. Black vertical lines show the ALMA band 3 range and black horizontal lines show the Molnar et al. correlation coefficient = 0.84, and the red vertical line shows the maximum correlation in the original resolution case, which is at 0.8 mm.

lost. Consequently, the data ranges for these very blurred maps become very narrow, which then results in a high correlation coefficient. The impact of a lower spatial resolution on the data ranges is also visible in Fig. 3c,f and 4c,f: The shown distributions become notably narrower as a function of spatial resolution for the whole box, QS region, and EN region, being broadest at the original resolution and narrowest when degraded with the 3.0 mm PSF. Most importantly, the highest correlation for the degraded maps with a value of 0.844 is found for the EN region at 1.1 mm, whereas the QS region has a maximum of 0.839 at

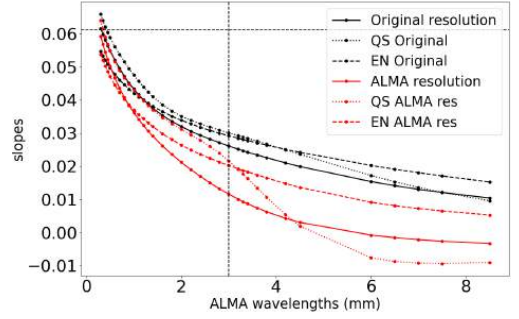


Fig. 8. Comparison of the calculated slopes for the scatter plots, legend same as Fig. 6. The black lines show the Molnar et. al. slope = 0.0612 at 3 mm.

1.0 mm. The correlation for the whole box peaks with 0.799 at a wavelength of 1.0 mm as well. These results suggest that (i) the highest correlation between the $H\alpha$ line core width and mm continuum brightness temperature maps is found for wavelengths at 1.0 mm, which corresponds to ALMA Band 7, and that (ii) the correlation between observed $H\alpha$ line core width maps and simultaneously obtained ALMA Band 7 brightness temperature maps is expected to be higher than what was found by Molnar et al. (2019) for Band 3 observations (at 3.0 mm); see Sect. 4.2 for further discussion.

The blue contours in Fig. 4c and f, which represent the EN region, show higher $H\alpha$ line core widths and mm brightness temperatures. On the other hand, the green contours, which represent the QS regions, show lower intensities in mm and lower $H\alpha$ linewidths in both resolutions; these differences are more distinct in the degraded resolution case. As the smaller network-internetwork features get blurred, the higher (lower) intensities in the QS (EN) region get blurred with neighbouring lower (higher) intensities and hence the green (blue) contours shift downwards (upwards). The slopes of the fitted lines for the three distributions change with resolution. The slope decreases for the EN case but increases for the QS case with the degraded resolution, as can be seen in Fig. 8 for all the cases in the dataset.

The slopes show a general decreasing trend with wavelength. As the wavelength increases, the radiation originates from a slightly higher layer of the atmosphere, which is on average slightly hotter. As seen in Fig. 6, the temperatures at different wavelengths are dependent on the formation heights, in addition to the resolution. This is evident from the decreasing slopes shown in Fig. 8. For the degraded resolution case, the difference in the slope for QS and EN regions is more than the original resolution case. In particular, for the EN case, as seen in Figs. 3 and 4, in the degraded resolution case (panels d and e), the brightness temperatures decrease, decreasing slopes significantly. For the QS case, on the other hand, the slopes remain comparable, or approximately the same in both resolutions. This is explained by the blurring effect due to the application of the ALMA PSFs, but in the QS region, the features are more equally distributed. The slopes therefore do not significantly change with the resolution in the mm range of interest (Bands 3-6). The line widths derived from the time-averaged $H\alpha$ intensity maps following the definition by Molnar et al. (2019) produce very similar trends and also indicate that the best match occurs at wavelengths corresponding to ALMA Band 7. Please refer to Sects. 3.3 and 4.2 for further discussion.

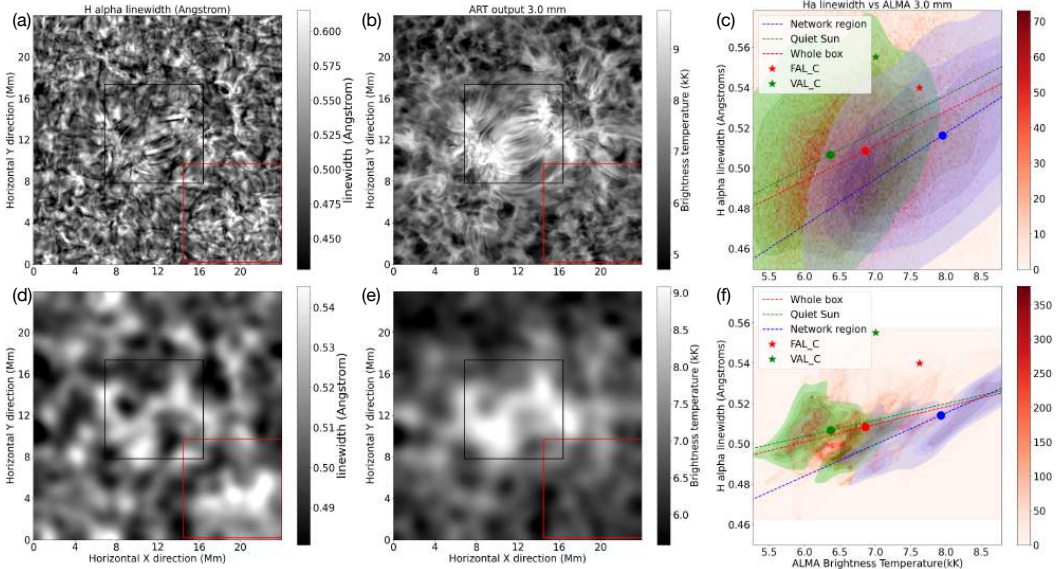


Fig. 9. Same as Fig. 3, for time-averaged dataset.

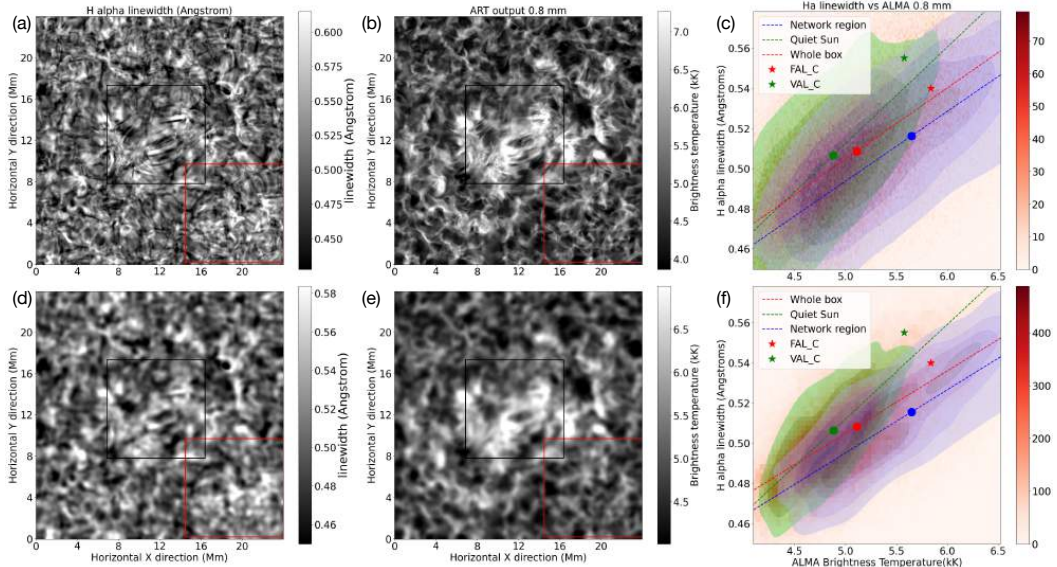


Fig. 10. Same as Fig. 4, for time-averaged dataset.

3.3. Dependence on temporal resolution

Figures 9 and 10 show the original and ALMA resolution maps for the dataset averaged over 10 min. The comparison of features in Figs. 9a,b and 3a,b with those in Figs. 10a,b and 4a,b shows that the time averaging causes the features to smooth out, as expected. The QS, EN, and whole box contours show less spread in the time-averaged case than in the single snapshot

case, as observed in Figs. 9c,f and 3c,f and Figs. 10c,f and 4c,f, respectively. When calculating the H α line core width from the time-averaged maps and comparing it to the time-averaged mm brightness temperature maps, the correlation between the H α line core width maps and the mm brightness temperature maps at original resolution decreases, whereas the correlation increases significantly for the corresponding maps at reduced (i.e. ALMA) resolution. The correlation is highest for the EN case and the

lowest for the QS case at both resolutions. This can be attributed to the differences in the small-scale features in the QS region, which get averaged over time and therefore do not match in the two data sets at degraded resolution. Similarly, the slopes for the QS region are also lower than for the whole box, whereas the slopes for the EN region are higher than for the whole box. The slopes do not show very drastic changes from the single snapshot case, but they are monotonically decreasing for all pixel sets.

4. Discussion

The $H\alpha$ line core widths correlate best with the mm continuum brightness temperatures at a wavelength of 0.8 mm. The Pearson correlation coefficients for the degraded maps are determined as 0.778 for the whole box, 0.808 for the QS region, and 0.834 for the EN region (see Table 1). These results imply that, despite the similarities of the $H\alpha$ linewidth with the observational ALMA Band 3 data found by Molnar et al. (2019), a closer match with Band 7 is to be expected. The immediate next step would therefore be to compare observational ALMA Band 7 data with co-observed $H\alpha$ data but, to the best of our knowledge, no such data are currently available for the study presented here.

4.1. Effect of spatial resolution

One of the aims of this study is to use high-resolution synthetic data at mm wavelengths to investigate how they can complement other diagnostics, such as $H\alpha$, for determining the properties of small-scale features in the solar atmosphere. Even though the resolution of ALMA observational data is outstanding compared to previous observations at mm wavelengths, the resolution is very low compared to what is typically achieved at optical wavelengths (see e.g. White et al. 2006; Wedemeyer et al. 2016, and references therein).

The comparison between maps at the original resolution and maps at the ALMA resolution using Gaussian kernels as simplified PSFs for the respective wavelengths (see Figs. 3 and 4) shows that there are two effects in action: the change in the formation layer for the mm data, and the decreasing resolution due to the increasing wavelength. These two effects cannot be disentangled in observational data, but with a simulation like the one employed here the physical and instrumental effects can be separated. In Fig. 6, the effect of the change in formation height for the continuum radiation at mm wavelengths and the change in resolution for the given wavelength are demonstrated. Although the average brightness temperature of the whole simulation box remains the same when degrading the resolution at a given wavelength, the width of the brightness temperature distribution (as represented by the shaded areas of one standard deviation around the mean values in the figure) reduces with degrading resolution. The increase in correlations and a general decrease in slopes with the degradation of the resolution can be attributed to this phenomenon.

To understand this impact of the spatial resolution more quantitatively, the values of the correlations for all six cases for $\lambda = 0.8$ mm and $\lambda = 3.0$ mm are listed in Table 1. The correlations significantly increase with the degradation of the resolution, as observed in Fig. 7. On the other hand, as seen in Fig. 8 and Table 1, the slopes do not change significantly. Hence, it can be safely speculated that the $H\alpha$ linewidth and mm brightness temperatures are correlated and follow the linear fit fairly well.

Figure 16 presents the formation heights for the continuum at wavelengths of 3.2 mm, 1.8 mm, and 0.8 mm, along with the ver-

tical temperature slice through the model atmosphere. Two more formation height profiles are plotted for the linewidth definition by Molnar et al. (2019; cf. Cauzzi et al. 2009) and for the line core width as defined by Leenaarts et al. (2012). In both cases, the plotted line is the average formation height of the wavelength points in the blue and red line wing that result from the calculation of the linewidth. It is observed that the Leenaarts et al. (2012) definition agrees better with the 0.8 mm formation height range. The Molnar et al. (2019) linewidth is rather a diagnostic of the lower atmosphere.

4.2. Comparison with observations

To compare these results with the observational study by Molnar et al. (2019), we used the same definition of the linewidth, which follows the approach by Cauzzi et al. (2009, see Sect. 2.4). The corresponding $H\alpha$ and mm maps at the original and degraded resolution with the scatter contour plots are shown in Figs. 12 and 13. In Figs. 14c,f and 15c,f, the black dashed lines show the respective correlation and slope calculated by Molnar et al. (2019) for the observational data obtained with ALMA in Band 3 (3 mm) on 23 April 2017 (see their Fig. 3). We produced a brightness temperature map similar to the one shown in Fig. 3 by Molnar et al. (2019) by time-averaging the corresponding data that is publicly available on the Solar ALMA Science Archive (SALSA, Henriques et al. 2022; see Fig. 11). The differences between the data from Molnar et al. (2019) and the data taken from SALSA are due to the difference in the applied imaging, including the choice of CLEAN parameters and the combination of the interferometric and total power (TP) data, as Molnar et al. (2019) follow the standard approach while the SALSA data are produced with the Solar ALMA Pipeline (Wedemeyer et al. 2020). Please refer to White et al. (2017) and Shimojo et al. (2017) for a detailed discussion of the uncertainties of the interferometric and TP data, which both affect the resulting absolute brightness temperatures. A cutout from the central part of the observed field of view with the same extent as the synthetic observations presented here (i.e. 24 Mm \times 24 Mm) is shown in Fig. 11b to allow for a direct comparison. Within the 1st and 99th percentiles, the brightness temperature range is observed to be between 5 kK and 11 kK both in the observational data and the simulated data (see Fig. 3e), in particular given the aforementioned uncertainties in absolute brightness temperatures derived from ALMA observations. This qualitative agreement with observations was already demonstrated for a different snapshot of the same Bifrost simulation by Loukitcheva et al. (2015); see also Loukitcheva et al. (2004). As mentioned in Sect. 3.1, the average brightness temperature at 3.0 mm for the whole computational box of the 3D model is only \sim 100 K higher than the corresponding value for the VAL C model and only 520 K lower than the FAL C value. These therefore all agree with the reference value of 7300 K derived by White et al. (2017) from ALMA observations within the aforementioned uncertainties.

The resolution of the observed ALMA data shown in Fig. 11 appears to be lower than for the degraded maps presented in Fig. 4e, which can be attributed to several factors. Firstly, as detailed in Sect. 2.6, the synthetic brightness temperatures maps are degraded to ALMA's angular resolution by convolution with ideal PSFs, each of which is constructed as a circular Gaussian with a width appropriate for the respective wavelength. This simplified approach corresponds in principle to a telescope with a filled aperture of the size of the longest baseline. However, in reality, ALMA consists of a limited number of antennas in a given configuration, which results in a sparse sampling of the spatial Fourier

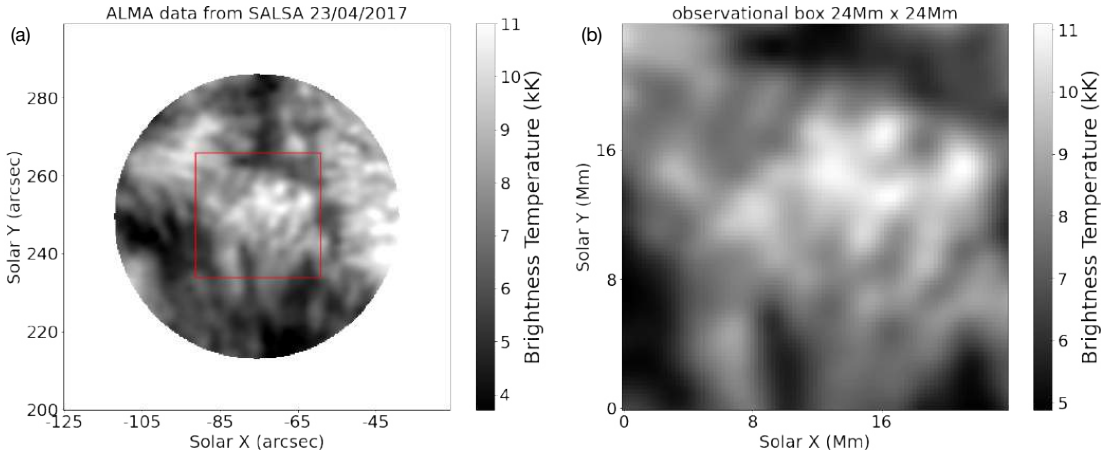


Fig. 11. Time-averaged ALMA Band 3 brightness temperature for the same measurement set as used by Molnar et al. (2019), i.e. ADS/NRAO.ALMA#2016.1.01129.S from 23 April 2017. The data were averaged over the period from 17:31 to 17:41 UTC. (a) The whole FOV. (b) The central 24 Mm × 24 Mm part, also indicated by the red box in panel (a) for comparison with the simulated data.

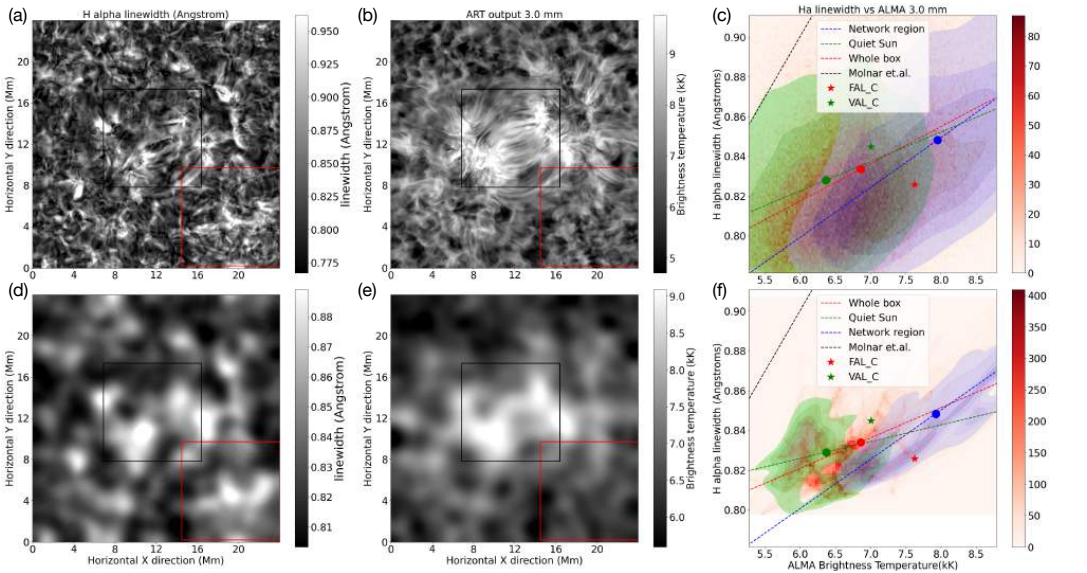


Fig. 12. Same as Fig. 9, for the Molnar et al. (2019) definition of linewidth. The black dashed line denotes the linear fit by Molnar et al. (2019).

space of the observed source. The resulting PSF (or rather referred to as synthesised beam) of the interferometric array is typically elongated and tilted. Properly accounting for these detailed instrumental effects, the additional degradation due to Earth’s atmosphere and the necessary imaging of the ALMA data (see e.g. Henriques et al. 2022) requires a much more detailed and computationally more expensive modelling approach (Wedemeyer et al. 2022), which goes beyond the scope of the study presented here. However, overall it is safe to assume that the employed degradation of the synthetic brightness temperature maps is still too optimistic. The same is true for the synthetic H α data for which fur-

ther instrumental effects and the influence of the Earth’s atmosphere are not accounted for. The statement that the employed instrumental degradation for ALMA is still too optimistic is confirmed by the power spectral density shown for the ALMA Band 3 in Fig. 5. The curve for the observational data starts to drop at a slightly larger spatial scale as compared to the simulated data and also shows a noise component at smaller spatial scales that is not included in the simulations here.

Secondly, the ALMA image shown in Fig. 11 represents the time-average over an observational period of 10 min, which is produced in the same way as described by Molnar et al. (2019).

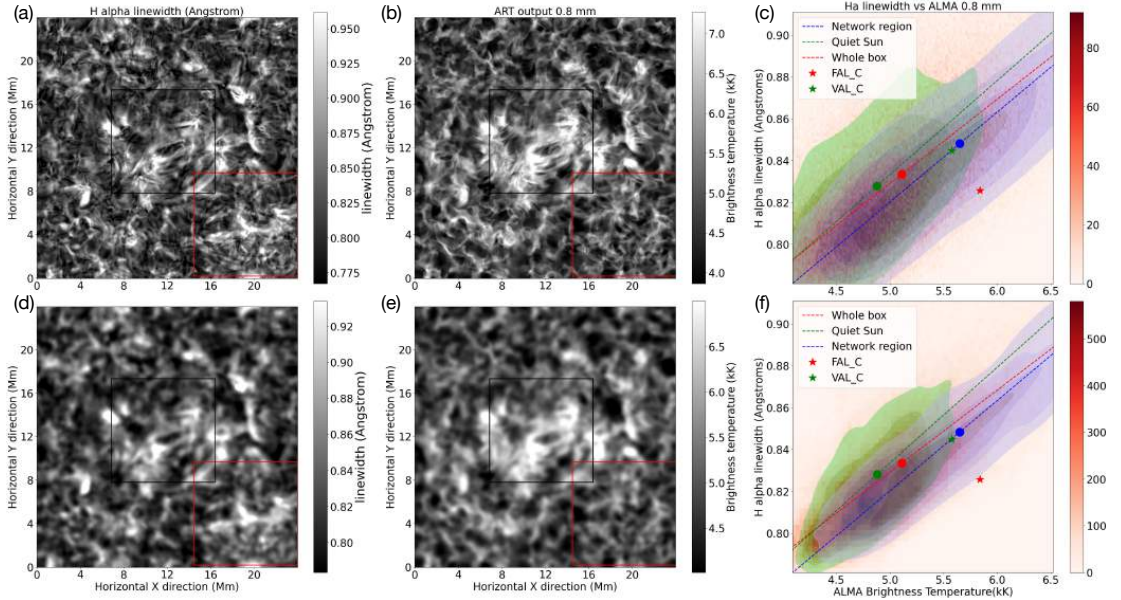


Fig. 13. Same as Fig. 12, for 0.8 mm.

Also, the $H\alpha$ observations obtained with IBIS by Molnar et al. (2019) were time-averaged for a comparison with the aforementioned ALMA data. A period of 10 min is substantial given the dynamic timescales on which the chromospheric fine structure evolves, and the time-averaging further blurs the resulting images. This effect can be seen by comparing, for example, Figs. 3e and 12e, but it is also apparent in Fig. 3 by Molnar et al. (2019), which compares snapshots to time-averaged images. In Table 1, the correlation coefficients and the slopes for both cases are listed.

Thirdly, limited spectral sampling points for the IBIS observations (Cavallini 2006) and also the time it takes to scan through the spectral line profile would contribute to uncertainties. For our simulated data, we used more than three times more spectral sampling points for the $H\alpha$ line, namely 101, as compared to the 29 points for the IBIS data used by Molnar et al. (2019).

As a result of the limited resolution discussed above, emission from different heights gets mixed within the respective synthesised ALMA beam. It is particularly important to be aware of this effect in view of the highly dynamic and intermittent nature of the solar chromosphere, which can result in substantial changes in formation height across small (possibly unresolved) spatial distances. In addition, it should be noted that the region observed by Molnar et al. (2019) comprises a mix of plage, network, and magnetically quiet regions, whereas the simulated data contain only EN and QS regions and can therefore only be compared within the respective limitations.

As a result of these effects, differences in the density plot for $H\alpha$ linewidth versus ALMA brightness temperature for the simulated data in Fig. 12f and the corresponding density plot for observed data in Molnar et al. (2019), see their Fig. 4) are expected. However, it should be noted that, despite these effects, the distributions in observed and simulated data are very similar. The simulated QS distribution coincides with the high-density

scatter distribution at low observed brightness temperatures and low $H\alpha$ line widths in the plot shown by Molnar et al. (2019). The blue EN contour, which has a slightly lower slope than the slopes for the QS part and the slope for the whole box in the simulated data, has its counterpart in the scatter plot for the observed data. The calculated slopes for the whole box at the degraded resolution are slightly different, which can be attributed to the aforementioned differences between the observations and the simulations reported here. For the observed data, Molnar et al. (2019) report the slope to be 0.0612, as compared to 0.015 for the whole box at degraded spatial and temporal resolution for the simulated data (see Table 1 for details).

As shown in Sect. 3.2, changing the spatial resolution affects the correlations between $H\alpha$ linewidth and mm brightness temperatures. The correlation for the data observed at 3 mm reported by Molnar et al. (2019) is 0.84, which is close to the correlation of 0.61 found here for the simulated data at degraded spatial and temporal resolution. The correlation is 0.5 for the data at the original resolution. The difference in the correlation coefficients is because the spatial arrangement of the individual pixels relative to each other does not matter when calculating them. Consequently, the correlation coefficient increases with decreasing spatial resolution, because the resulting image degradation gradually removes the largest variations on the smallest scales in both the ALMA and the $H\alpha$ maps. For both data sets, lowering the spatial resolution results in narrower intensity distributions towards the mean value. The height at which the core is formed is higher and the linewidth is lower for the quiet region, and the formation height is lower and linewidth is higher for the EN region (Leenaarts et al. 2012).

4.3. Effect of temporal resolution

When time-averaging the spatially degraded $H\alpha$ and mm brightness temperature maps, the resulting correlation coefficients

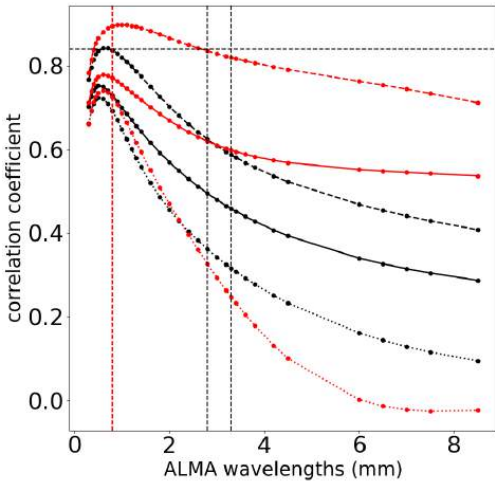


Fig. 14. Same as Fig. 7, but for the time-averaged data set, for the Molnar et al. (2019) definition of linewidth. The legend is the same as for Fig. 7

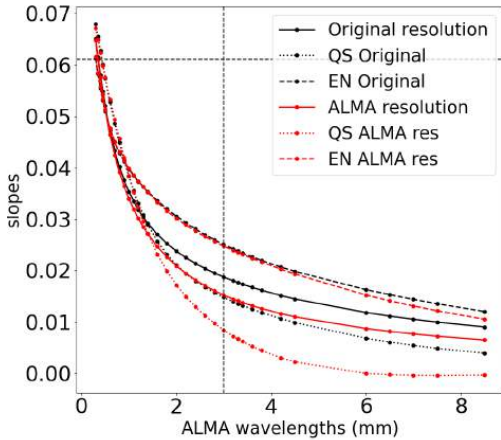


Fig. 15. Same as Fig. 8, but for the time-averaged data set, for the Molnar et al. (2019) definition of linewidth.

change with respect to the results based on single snapshots. As summarised in Table 1, for the line core width as defined by Leenaarts et al. (2012), the correlation coefficients for all three pixel sets become lower when time-averaging both at original and reduced resolution, except for a small increase for the correlation with the 3 mm data across the whole box at reduced resolution (cf. Fig. 14). The same behaviour is found when using the linewidth definition by Molnar et al. (2019), except perhaps for a small increase of the EN correlations both at original and reduced spatial resolution.

In general, temporal averaging results in blurring of the maps and lower correlation coefficients. However, for the EN region, time-averaging can tend to highlight persistent features, resulting in a slightly higher correlation coefficient. In contrast, for the QS region, the more uniformly distributed and short-lived

features get averaged over time and space and lose the similarities. Similarly, the values of slopes for original and degraded resolutions are very close for individual wavelengths (see Fig. 15). In conclusion, time averaging causes a decrease in the correlation in the QS case and a small increase in the EN case for the Molnar definition, while the slopes decrease marginally. This effect becomes slightly more notable for the maps at reduced spatial resolution as compared to the maps at original resolution. We conclude that the exact values and behaviour of correlation coefficients as shown here may depend critically on the spatial and temporal resolution of the employed data.

4.4. Comparison of linewidth definitions

As seen in Fig. 2, the value and the atmospheric layer connected to the linewidth change significantly based on the definition used. In the case of the Molnar et al. (2019) definition, as described in Sect. 2.4, the continuum and therefore the line depth are derived from the $\pm 1 \text{ \AA}$ region around the line core. On the other hand, for both the Leenaarts et al. (2012) definition and the FWHM, the continuum is defined based on the true continuum intensity. The wavelength grid points used for the calculation of the line core width – which are close to the line core – are formed significantly higher in the atmosphere than they are when taking the Molnar et al. (2019) approach, as illustrated in Fig. 16. The radiation at the wavelength points in the line wings as used for the FWHM definition are accordingly formed lower in the atmosphere, even lower than for the Molnar et al. (2019) definition. In Fig. 17, the line widths for all three definitions are compared, implying the above-discussed differences in connected atmospheric heights, which are highest for the line-core width definition by Leenaarts et al. (2012). The FWHM linewidth map much resembles a granulation pattern as formed in the low photosphere.

The distribution of line core widths as seen in Fig. 18a is in the range of line core widths calculated by Leenaarts et al. (2012). Using the Molnar et al. (2019) definition instead produces larger linewidths (see Fig. 18b), which nonetheless remain smaller than the observationally determined values reported by Molnar et al. (2019). The simulated linewidths according to the Molnar et al. (2019) definition cover a range of 0.75 to 1.0 \AA , whereas the values derived from observations by Molnar et al. (2019) are in the range of 0.9 to 1.3 \AA , which is also in line with the observed linewidth for α Cen A (see Sect. 4.5). The reason behind this discrepancy could be that the $H\alpha$ opacity used in the simulations that include the radiative transfer calculations is lower than that for the real Sun (Leenaarts et al. 2012). Similarly, as seen in Fig. 16, the formation heights of the radiation at the wavelength positions entering the line-core width calculation with the Leenaarts et al. (2012) definition are closer to the formation heights of the mm continua than to the corresponding heights for the Molnar et al. (2019) definition. The conclusion that the Leenaarts et al. (2012) definition produces a better match of the $H\alpha$ line (core) width with the mm continua is also implied by a closer match in terms of spatial power spectral density as compared to the Molnar et al. (2019) definition (see Fig. 5). This seems to be true at both the original and reduced resolutions.

4.5. Implications for solar-like stars

The correlation between $H\alpha$ linewidth and mm brightness temperatures described in Sect. 3.2 can be transferred to the study of Sun-like stars. It should be noted that the study presented

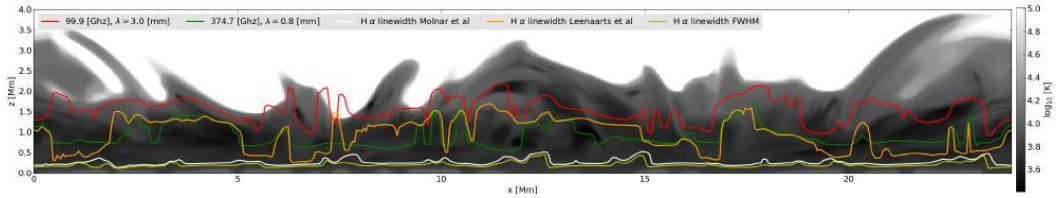


Fig. 16. Simulated logarithmic gas temperature (grey-scale) in a vertical slice of 3D rMHD Bifrost simulations. The solid lines represent the heights at which the optical depth is unity at a wavelength of 3.2 mm (red), and 0.8 mm (green), which correspond to ALMA bands 3, 5 and 7, respectively. The orange, white and yellow lines show the average heights at which the red and blue sides of the $H\alpha$ line width according to the Leenaarts et al. (2012), Molnar et al. (2019) and FWHM definitions of linewidth are formed.

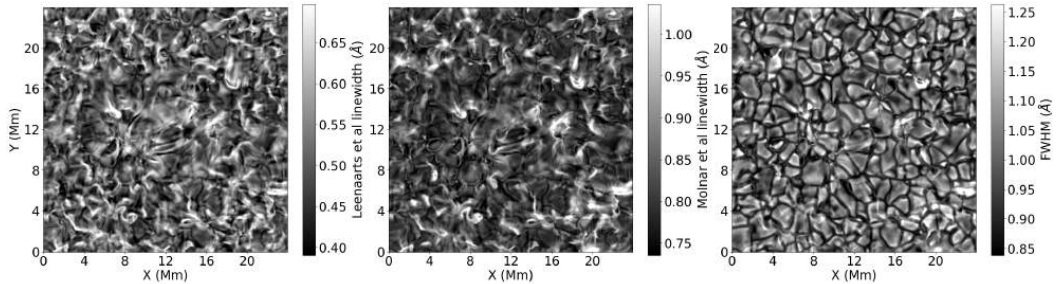


Fig. 17. Maps of linewidths for original resolution case for the single snapshot: Left: Leenaarts et al. (2012) definition, middle: Molnar et al. (2019) definition and right: FWHM.

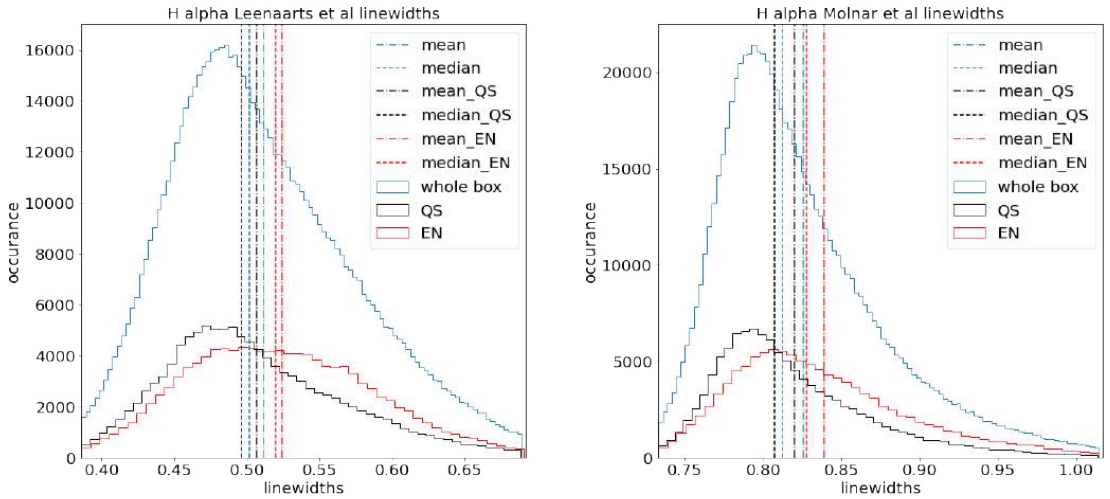


Fig. 18. Left: Distribution of $H\alpha$ core widths (following the definition by Leenaarts et al. 2012) for the whole time series. Right: Corresponding line widths according to the definition by Molnar et al. (2019). The whole box, QS and EN regions are separately plotted in blue, black and red, and mean and median values for the three sets of pixels are indicated with a dot-dashed and dashed lines in the respective colours. Please note the difference in ranges for linewidths axes in the two plots.

here is based on simulated EN and QS regions, while the corresponding trends for a whole active region could not be investigated because of the lack of an equivalent consistent simulation. Any comparison with unresolved observations of other solar-like stars therefore needs to account for the potential contributions of active regions via corresponding filling factors.

A direct application to stellar observations is to estimate the stellar activity level, in particular for Sun-like stars as for instance used in the studies by Liseau et al. (2016) and Mohan et al. (2021, 2022). The position in the $H\alpha$ linewidth–mm brightness temperature plane as derived from adequate observations then provides constraints on the properties of the observed stellar atmo-

sphere. This approach is illustrated by comparing the data points for the semi-empirical 1D models FAL C and VAL C to the averages for the whole box, EN, and QS data points on the $H\alpha$ linewidth–mm brightness temperature plane in Figs. 3 (c and f) and 4 (c and f). For the disk-integrated signal, the centre-to-limb variation for the $H\alpha$ line and ALMA full disk data should be taken into account (see e.g. Alissandrakis et al. 2022a,b; Otsu et al. 2022; Nindos et al. 2018, and references therein). As the $H\alpha$ core forms in the chromosphere and the wings in the photosphere, the limb effects would be varying (brightening or darkening depending on the wavelength) when going from the core to the wing. In a recent study based on SST observations, Pietrow et al. (2022) concluded that chromospheric lines might exhibit a blueshift towards the limb due to the chromospheric canopies, but the resulting effect on the equivalent width or linewidths is non-trivial. Further, the authors show that the line core widths would decrease when going from the centre to the limbs. Further systematic studies need to be conducted in order to understand the limb effects on the correlations between the two diagnostics and the implications for disk-integrated stellar observations.

The brightness temperature values at the wavelengths of 0.8 mm and 3 mm for α Cen A, which are obtained from ALMA observations (see Mohan et al. 2021, and references therein), are in line with the values derived from ALMA observations of the Sun and also with those based on the simulations presented in this study. In contrast, the $H\alpha$ line profile for α Cen A (see Fig. 2), with a line core width of $\sim 0.6 \text{ \AA}$, is significantly broader than the simulated data based on the Bifrost simulation and also for the FAL C and VAL C models, which causes the respective data point to be placed away from the linear fit for the solar simulation shown in Figs. 3 (c and f) and 4 (c and f); see the black circle with error bars in these figures. The α Cen A datapoint is out of the bounds of the plane in Figs. 12 (c and f) and 13 (c and f) as the calculated Molnar et al. (2019) linewidth is 1.1 \AA . The comparatively broad $H\alpha$ line profile for α Cen A is likely due to differences in atmospheric structure and the activity level of this star as compared to the Sun; although an in-depth study would be needed in order to draw any detailed conclusions. We also note that the solar observations are spatially resolved and cover only a small region on the Sun, whereas the α Cen A data are intrinsically integrated across the whole (spatially unresolved) stellar disk.

5. Conclusions

We look at the synthetic $H\alpha$ linewidth and the brightness temperatures corresponding to the mm wavelengths generated from a close-to-realistic 3D Bifrost model. Degrading the spatial resolution of these synthetic observations to ALMA resolution results in decreased standard deviations of the synthetic observables: $H\alpha$ line width and mm brightness temperatures, and increased correlations between them. With increasing wavelength, the beam size increases and the small structures get blurred out, resulting in a further increased correlation between the two diagnostics. But this degradation in terms of spatial resolution does not have any significant effect on the mean slopes for the linear fits on the $H\alpha$ linewidth versus mm brightness temperature distributions. This implies that the instrumental resolution of ALMA is sufficient to capture the similarities between the two diagnostics.

The solar results in comparison with the observations of α Cen A strongly imply that the $H\alpha$ linewidth and mm continuum

brightness temperatures can be considered equivalent indicators; as shown in Fig. 16, they form close to each other and the thermal stratification of a star can be constrained using the correlations and slopes found in this study in the absence of mm data, simply using the $H\alpha$ data, and vice versa. As discussed in Wedemeyer et al. (2016, see also references therein), using multi-wavelength observations along with mm observations can provide better insights into the thermal structure of stellar atmospheres.

The $H\alpha$ linewidth depends on the temperature in the line-forming region, which is observed using mm continua (Leenaarts et al. 2012). The brightness temperatures can be directly calculated from the mm continuum intensity maps, which correlate with the $H\alpha$ linewidth very well. The best match, that is, in terms of the highest correlation, is found for a wavelength of 0.8 mm, which corresponds to ALMA Band 7. Simultaneous $H\alpha$ –ALMA Band 7 observations have therefore the potential advantage of better constraining the imaging process, resulting in more reliable temperature measurements for the solar chromosphere. Published simulations of the solar chromosphere (Carlsson et al. 2016) show overly narrow MgII h & k lines compared with IRIS observations (Carlsson et al. 2019), indicating that the models have too little mass at upper chromospheric temperatures. Newer models in higher resolution, including ambipolar diffusion and non-equilibrium ionisation (e.g., Martínez-Sykora et al. 2023), flux emergence (Hansteen et al. 2023), or run with the MURaM code with chromospheric extensions (Przybylski et al. 2022), show significantly broader magnesium lines. It will be important to check the reported ALMA– $H\alpha$ relationships with these new models. As the correlation between the two diagnostics is high even in the case of lower resolution, this study may prove useful in mitigating the challenging task of calibrating mm continuum solar data obtained from ALMA.

Acknowledgements. We thank the referee for very valuable comments and suggestions, which improved considerably the quality of this paper. This work is supported by the Research Council of Norway through the EMISSA project (project number 286853), the Centres of Excellence scheme, project number 262622 (“Roseland Centre for Solar Physics”) and through grants of computing time from the Programme for Supercomputing. This paper makes use of the following ALMA data: ADS/NRAO.ALMA#2016.1.01129.S. ALMA is a partnership of ESO (representing its member states), NSF (USA) and NINS (Japan), together with NRC (Canada), MOST and ASIAA (Taiwan), and KASI (Republic of Korea), in cooperation with the Republic of Chile. The Joint ALMA Observatory is operated by ESO, AUI/NRAO and NAOJ. The authors thank Porto de Mello et al. (2008) for their prompt correspondence regarding the $H\alpha$ observational data of α Cen A. This research utilised the Python libraries matplotlib (Hunter 2007), seaborn (Waskom 2021) and the NumPy computational environment (Oliphant 2006). The authors would like to thank Thore Espedal Moe, Mats Ola Sand, Atul Mohan, Juan Camilo Guevara Gomez, Vasco Henriquez, Shahin Jafarzadeh for their support.

References

- Alissandrakis, C. E., Bastian, T. S., & Brajša, R. 2022a, *Front. Astron. Space Sci.*, **9**, 981320
- Alissandrakis, C. E., Bastian, T. S., & Nindos, A. 2022b, *A&A*, **661**, L4
- Boone, F. 2013, *Exp. Astron.*, **36**, 77
- Carlsson, M., Hansteen, V. H., Gudiksen, B. V., Leenaarts, J., & De Pontieu, B. 2016, *A&A*, **585**, A4
- Carlsson, M., De Pontieu, B., & Hansteen, V. H. 2019, *ARA&A*, **57**, 189
- Cauzzi, G., Reardon, K., Rutten, R. J., Tritschenaar, A., & Uitenbroek, H. 2009, *A&A*, **503**, 577
- Cavallini, F. 2006, *Sol. Phys.*, **236**, 415
- Cram, L. E., & Mullan, D. J. 1985, *ApJ*, **294**, 626
- de la Cruz Rodríguez, J., Szydlarski, M., & Wedemeyer, S. 2021, <https://zenodo.org/record/4604825>
- Dulk, G. A. 1985, *ARA&A*, **23**, 169

- Eklund, H., Wedemeyer, S., Szydlarski, M., & Jafarzadeh, S. 2021, *A&A*, 656, A68
- Fontenla, J. M., Avrett, E. H., & Loeser, R. 1993, *ApJ*, 406, 319
- Gizis, J. E., Reid, I. N., & Hawley, S. L. 2002, *AJ*, 123, 3356
- Gudiksen, B. V., Carlsson, M., Hansteen, V. H., et al. 2011, *A&A*, 531, A154
- Hansteen, V. H., Martínez-Sykora, J., Carlsson, M., et al. 2023, *ApJ*, 944, 131
- Hanuschik, R. W. 1989, *Ap&SS*, 161, 61
- Henriques, V. M. J., Jafarzadeh, S., Guevara Gómez, J. C., et al. 2022, *A&A*, 659, A31
- Hofmann, R. A., Reardon, K. P., Milic, I., et al. 2022, *ApJ*, 933, 244
- Högbom, J. A. 1974, *A&AS*, 15, 417
- Hunter, J. D. 2007, *Comput. Sci. Eng.*, 9, 90
- Leenaarts, J., & Carlsson, M. 2009, *ASP Conf. Ser.*, 415, 87
- Leenaarts, J., Carlsson, M., Hansteen, V., & Rutten, R. J. 2007, *A&A*, 473, 625
- Leenaarts, J., Carlsson, M., & Rouppe van der Voort, L. 2012, *ApJ*, 749, 136
- Liseau, R., De la Luz, V., O’Gorman, E., et al. 2016, *A&A*, 594, A109
- Loukitcheva, M., Solanki, S. K., Carlsson, M., & Stein, R. F. 2004, *A&A*, 419, 747
- Loukitcheva, M., Solanki, S. K., Carlsson, M., & White, S. M. 2015, *A&A*, 575, A15
- Lyra, W., & Porto de Mello, G. F. 2005, *A&A*, 431, 329
- Marsden, S. C., Petit, P., Jeffers, S. V., et al. 2014, *MNRAS*, 444, 3517
- Martínez-Sykora, J., de la Cruz Rodríguez, J., Gošić, M., et al. 2023, *ApJ*, 943, L14
- Mohan, A., Wedemeyer, S., Pandit, S., Saberi, M., & Hauschildt, P. H. 2021, *A&A*, 655, A113
- Mohan, A., Wedemeyer, S., Hauschildt, P. H., Pandit, S., & Saberi, M. 2022, *A&A*, 664, L9
- Molnar, M. E., Reardon, K. P., Chai, Y., et al. 2019, *ApJ*, 881, 99
- Nindos, A., Alissandrakis, C. E., Bastian, T. S., et al. 2018, *A&A*, 619, L6
- Oliphant, T. E. 2006, *Guide to NumPy* (Trelgol)
- Otsu, T., Asai, A., Ichimoto, K., Ishii, T. T., & Namekata, K. 2022, *ApJ*, 939, 98
- Pasquini, L., & Pallavicini, R. 1991, *A&A*, 251, 199
- Pereira, T. M. D., & Uitenbroek, H. 2015, *A&A*, 574, A3
- Pietrow, A. G. M., Kiselman, D., Andrienko, O., et al. 2022, *A&A*, 671, A130
- Porto de Mello, G. F., Lyra, W., & Keller, G. R. 2008, *A&A*, 488, 653
- Przybylski, D., Cameron, R., Solanki, S. K., et al. 2022, *A&A*, 664, A91
- Rybicki, G. B., & Hummer, D. G. 1992, *A&A*, 262, 209
- Shimojo, M., Bastian, T. S., Hales, A. S., et al. 2017, *Sol. Phys.*, 292, 87
- Uitenbroek, H. 2001, *ApJ*, 557, 389
- Vernazza, J. E., Avrett, E. H., & Loeser, R. 1981, *ApJS*, 45, 635
- Vitas, N., Vitičchiè, B., Rutten, R. J., & Vögler, A. 2009, *A&A*, 499, 301
- Waskom, M. L. 2021, *J. Open Source Softw.*, 6, 3021
- Wedemeyer, S., Bastian, T., Brajša, R., et al. 2016, *Space Sci. Rev.*, 200, 1
- Wedemeyer, S., Szydlarski, M., Jafarzadeh, S., et al. 2020, *A&A*, 635, A71
- Wedemeyer, S., Fleishman, G., De La Cruz Rodríguez, J., et al. 2022, *Front. Astron. Space Sci.*, 9, 335
- Wedemeyer-Böhm, S. 2007, in *Convection in Astrophysics*, eds. F. Kupka, I. Roxburgh, & K. L. Chan, 239, 52
- White, S. M., Loukitcheva, M., & Solanki, S. K. 2006, *A&A*, 456, 697
- White, S. M., Iwai, K., Phillips, N. M., et al. 2017, *Sol. Phys.*, 292, 88
- Wooten, A., & Thompson, A. R. 2009, *IEEE Proc.*, 97, 1463

Appendix A: Additional brightness temperature maps for single snapshot with Leenaarts et al. (2012) linewidth

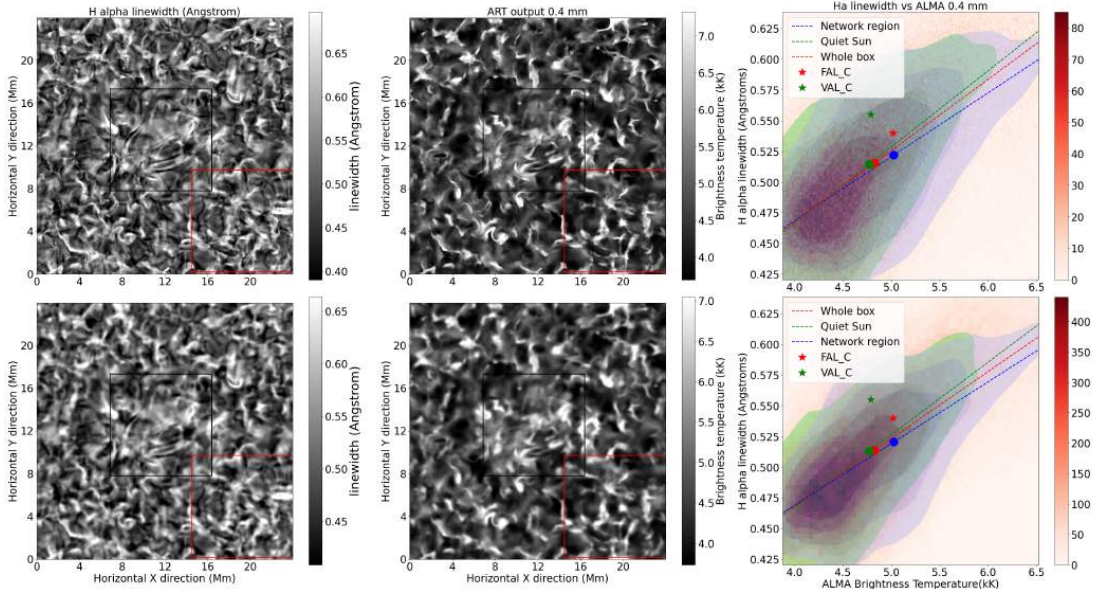


Fig. A.1. Same as Fig. 3, but for 0.4 mm corresponding to ALMA Band 9-10.

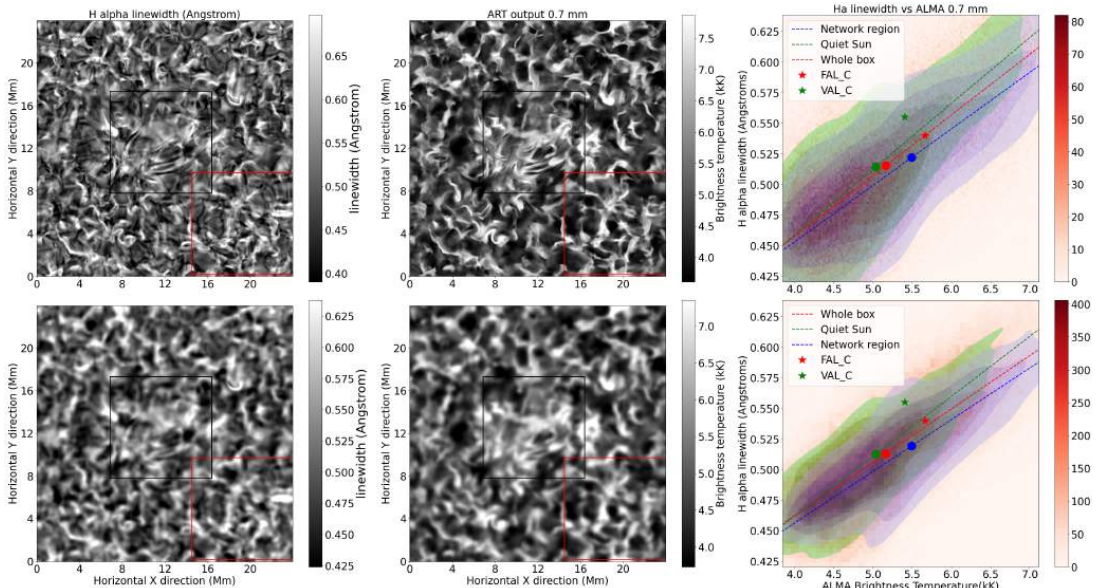


Fig. A.2. Same as Fig. 3, but for 0.7 mm corresponding to ALMA Band 8.

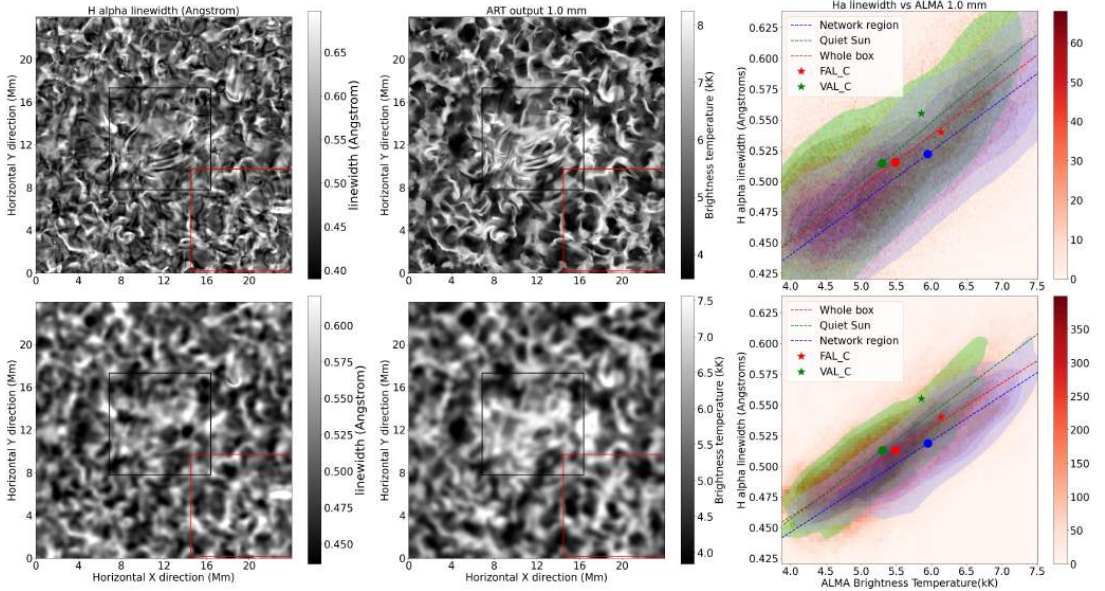


Fig. A.3. Same as Fig. 3, but for 1.0 mm, corresponding to ALMA Band 7.

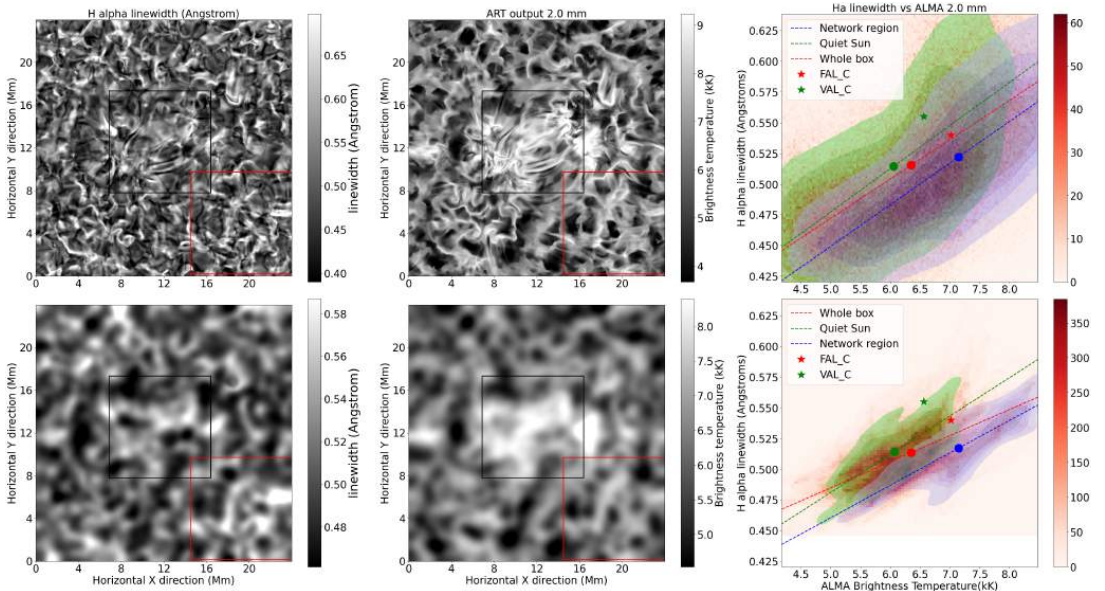


Fig. A.4. Same as Fig. 3, but for 2.0 mm, corresponding to ALMA Band 4.

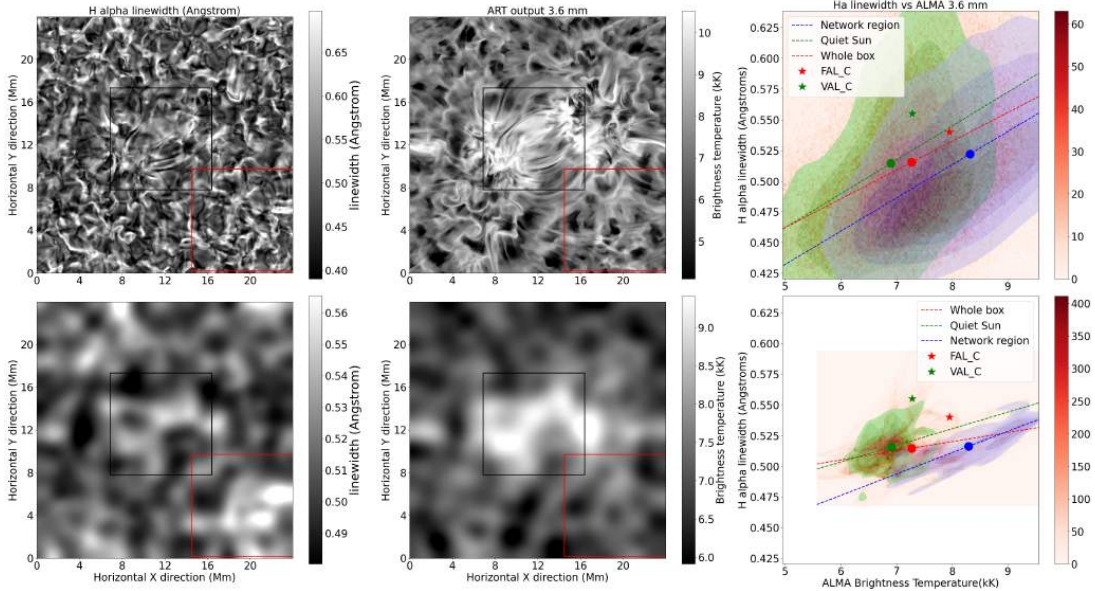


Fig. A.5. Same as Fig. 3, but for 3.6 mm, corresponding to ALMA Band 3.

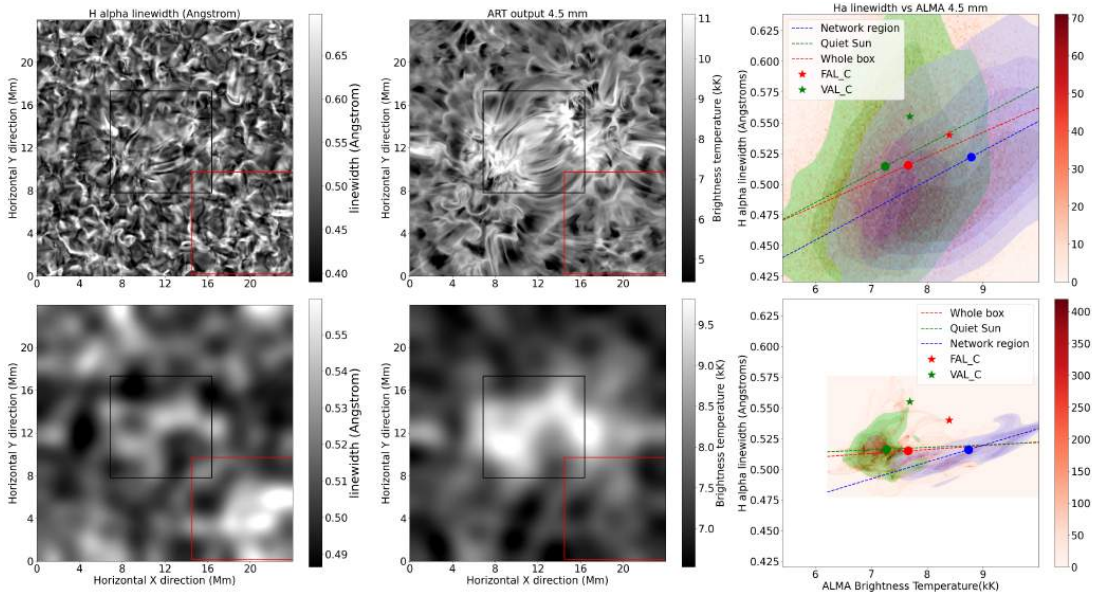


Fig. A.6. Same as Fig. 3, but for 4.5 mm, corresponding to ALMA Band 2.

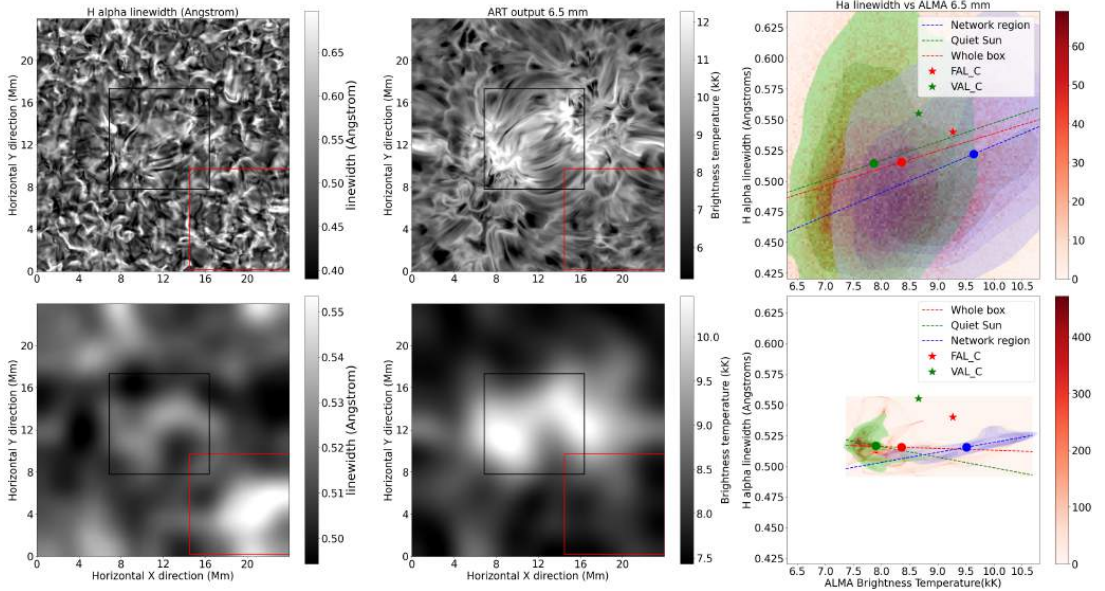


Fig. A.7. Same as Fig. 3, but for 6.5 mm, corresponding to ALMA Band 1.

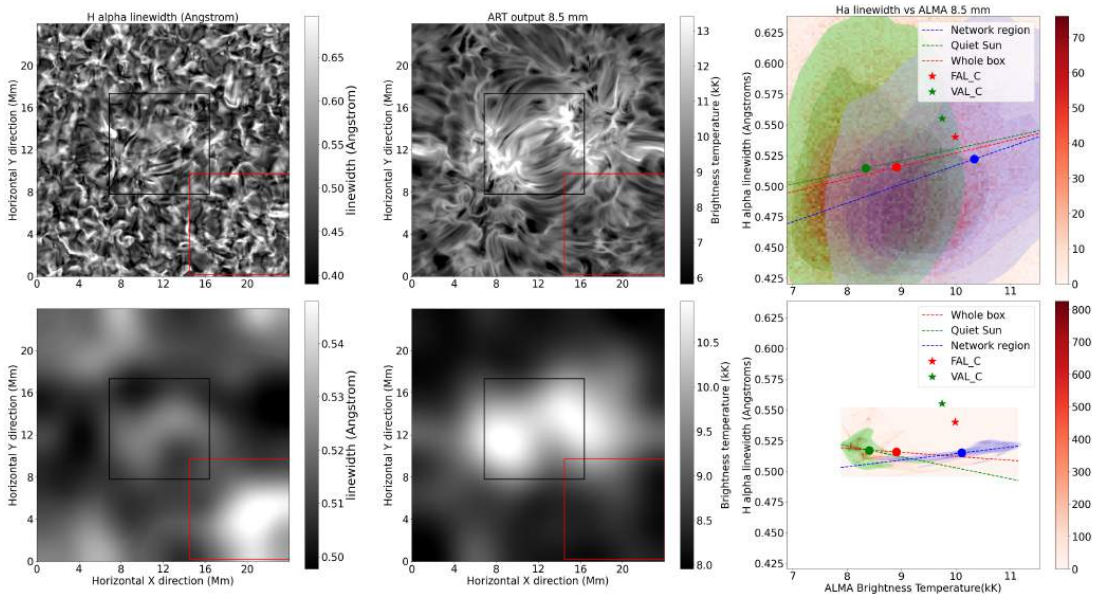


Fig. A.8. Same as Fig. 3, but for 8.5 mm, corresponding to ALMA Band 1.

Paper II

EMISSA (Exploring Millimeter Indicators of Solar-Stellar Activity). III. Comparison of Ca II indices and millimetre continua in a 3D model atmosphere

Sneha Pandit, Sven Wedemeyer, Mats Carlsson

Under review in: *Astronomy and Astrophysics*



Paper III

EMISSA (Exploring Millimeter Indicators of Solar-Stellar Activity). IV. Full-disk observations of the Sun

Sneha Pandit, Sven Wedemeyer, Atul Mohan, Sowmya Krishnamurthy, Henrik Eklund

Soon to be submitted to *Astronomy and Astrophysics*.



